

Flutter Analysis of Open-Truss Stiffened Suspension Bridges Using Synthesized Aerodynamic Derivatives

By

Adel Al-Assaf

A dissertation submitted in partial fulfillment of
the requirements for the degree of

Doctoral of Philosophy

WASHINGTON STATE UNIVERSITY
Department of Civil and Environmental Engineering

DECEMBER 2006

To the Faculty of Washington State University:

The members of the Committee appointed to examine the dissertation
of ADEL AL-ASSAF find it satisfactory and recommend that it be accepted.

Chair

ACKNOWLEDGMENT

I would like to express my gratitude to my professor in the Washington State University. Special recognition to Dr. Rafik Itani, Dr. William Cofer, Dr. Cole McDaniel, Dr. David Stock, Dr. David Pollock and Dr. Balasingam Muhunthan for their help.

This research is made possible by the funding of the United States Federal Highway Administration and the support of the Washington States Department of Transportation.

I also would like to thank everyone who helped me during pursuing this research.

Flutter Analysis of Open-Truss Stiffened Suspension Bridges Using Synthesized Aerodynamic Derivatives

Abstract

by Adel Al-Assaf, Ph.D.
Washington State University
December 2006

Chair: Rafik Itani

Aerodynamic analysis is of primary consideration in designing long-span bridges. Theoretical models as well as experimental tools have been developed, which resulted in Wind tunnel tests becoming the fundamental design tool.

Recent researches focus on alternative methods to assess the wind response of suspension bridges. These include the computational Fluid Dynamics (CFD) method, which is based on finite element analysis. Theoretically, this method is capable of solving different types of fluid-structure-interaction (FSI) problems.

This research discusses the flutter analysis of open-truss stiffened suspension bridges, with an emphasis on the Second Tacoma Narrows Bridge. The scope is to assess the wind response of the bridge using analytical tools. The approach suggested here is to synthesize the wind derivatives based on previous studies of a similar deck configuration. Then the equation of motion and the synthesized aerodynamic forces are solved to find the critical wind speed.

In order to conduct an aerodynamic analysis, the frequencies and the mode shapes of the bridge should be determined. Therefore, a frequency analysis is conducted using a detailed finite element model. The results are compared with an ambient study of the bridge, and found to be similar and accurate.

The solution procedure and assumptions of the approach are verified using the Golden Gate Bridge flutter analyses, where the experimental aerodynamic coefficients of the bridge are applied in the proposed procedure and compared with the analysis based on the synthesized coefficients. The results of both cases agree with the results in the literature. The analysis procedure is then conducted for the Second Tacoma Narrows Bridge to estimate the critical wind speed is found to be less than the flutter criteria of the bridge.

TABLE OF CONTENTS

Chapter 1	1
Introduction.....	1
1.1 Overview.....	1
1.2 Objectives	4
1.3 Outline.....	4
Chapter 2.....	7
Theory of Suspension Bridges	7
2.1 Introduction.....	7
2.2 Needs and Uses	9
2.3 History and Development	10
Chapter 3.....	16
Analysis Methods for Cabled Structures	16
3.1 Introduction.....	16
3.2 Theory of Cable	17
3.2.1 Cable Profile	17
3.2.2 Classical Theories	19
3.2.3 Finite Element Analysis.....	21
3.2.3.1 Modeling Issues	22
3.2.3.2 Finite Element Formulation	25
3.3 Shape-Finding.....	31
3.4 Frequency Analysis.....	32
3.4.1 Eignvalue analysis	33
3.4.2 Averaged Mechanical Properties	33

Chapter 4.....	36
Analysis of the Tacoma Narrows Bridge.....	36
4.1 Problem.....	36
4.2 Previous Research.....	37
4.3 Description and Specifications	37
4.4 Finite Element Model	41
4.4.1 Towers.....	43
4.4.2 Stiffening Truss.....	44
4.4.3 Floor Truss	44
4.4.4 Main Cable.....	45
4.4.5 Hangers	50
4.4.6 Material	51
4.4.7 Section Properties	52
4.4.8 Boundary Conditions	52
4.4.9 Nonlinear elements	53
4.4.10 Load and Mass Estimation.....	56
4.4.11 Estimation of Mass	58
4.5 Frequency Analysis.....	59
4.5.1 Ambient Study	59
4.5.2 Eigenvalue Analysis.....	60
4.5.3 Model Calibration and Analysis	61
4.6 Results.....	62
4.7 Discussion.....	69

Chapter 5	71
Bridge Aeroelasticity	71
5.1 Background	71
5.2 Earlier Aeroelasticity Theories	71
5.3 Early Bridge Aeroelasticity Theories.....	73
5.4 Wind Forces on Bridges	75
5.4.1 Vortex-shedding.....	77
5.4.2 Self-induced Forces	81
5.4.3 Buffeting	82
5.5 Analytical Models of Flutter	84
5.5.1 Equation of Motion	86
5.5.2 Self-induced Forces	87
5.5.3 Flutter Derivatives	89
5.5.3.1 Extracting Flutter Derivatives.....	91
5.5.3.2 Parametric Analysis	95
5.5.3.3 Solving for Flutter Condition.....	105
5.5.3.3.1 Two-Degree-of-Freedom System	105
5.5.3.3.2 Verification Problem.....	111
5.6 Flutter Criteria.....	114
5.7 Estimation of Design Wind Speed.....	114
Chapter 6	118
Flutter Analysis of the Second Tacoma Narrows Bridge	118
6.1 Problem Statement	118

6.2 Assumptions and Parameters	118
6.2.1 Synthesizing Wind Derivative	119
6.2.2 Verification of the Synthesized Wind Derivative	121
6.3 Results	122
6.3.1 Critical Flutter Condition	123
6.4 Discussion	124
Chapter 7	127
Conclusions and Recommendations	127
Appendix A	129
Analysis Results	129
A.1 Second Tacoma Narrows Bridge Frequency Analysis	129
Appendix B	133
MATLAB Programs	133
B.1 Coupling Coefficient	133
B.2 Flutter Analysis MATLAB Program	133
Appendix C	137
C.1 Calculation of Side-Span Profile	137
1.4 C.2 Derivation of Equations 5.19 coefficients	137
1.4 C.2 Derivation of Equations 5.19 coefficients	138
Appendix D	139
Miscellanies Calculations	139
D.1 Calculations of the Grate Opening Ratio of Tacoma Narrows Bridge:	139
Appendix E	140

Parameters for Aeroelasticity.....	140
E.1 Wind Characteristics	140
E.1.1 Estimating Wind Parameters	141
E.2 Flat Plate Aerodynamics.....	146
References.....	148

LIST OF FIGURES

Figure 1.1: The Second Tacoma Narrows Bridge	2
Figure 1.2: The open grates of the Second Tacoma Narrows Bridge	3
Figure 2.1: Suspension Bridges Components Chen and Duan (1999).....	8
Figure 3.1: Rigid Cable Load.....	17
Figure 3.2: Catenary versus parabolic cable profile	19
Figure 3.3: Deflection-load ratio relations among the theories	21
Figure 3.4: Catenary Cable Element subjected to nodal displacement.....	26
Figure 4.1: Section of the Second Tacoma Narrows Bridge Suspended Structure.	38
Figure 4.2: Existing Tacoma Narrows Bridge Elevation View.	39
Figure 4.3: The Detailed Finite Element Model of the Tacoma Narrows Bridge	42
Figure 4.4: TNB Main Tower Elev. and Side views.....	43
Figure 4.5: Tacoma Narrows Bridge Floor Truss.....	45
Figure 4.6: Catenary versus parabolic cable profile	47
Figure 4.7: Difference between catenary profile and parabolic profile along the main span length.....	49
Figure 4.8: Normalized tension in main cable	49
Figure 4.9: Hanger Force Model.....	50
Figure 4.10: Hanger Force	51
Figure 4.11: Modeling of Windshoe – top view at deck level.....	55
Figure 4.12: First Mode Period vs Normalized Density	56
Figure 4.13: Effect of Eliminating Tower Contribution to Frequency Content	58
Figure 4.14: Mode shapes of Identified Modes	66

Figure 4.15: Normalized modes of vibration.....	68
Figure 5.1: Grouping of Hangers.....	76
Figure 5.2: Torsional Oscillation of the First Tacoma Narrows Bridge.....	81
Figure 5.3: Flutter forces on a three degrees-of-freedom bridge section.....	89
Figure 5.4: NACA-0012-Airfoil test results, for H's and A's, by Scanlan and Tomko (1971).....	93
Figure 5.5 : Results for airfoil, Original Tacoma Narrows Bridge Deck, and six.....	96
Figure 5.6: The aerodynamic derivatives, H1, H3, A1 and A2 for grating-installed girders, with OR = 40% and $\alpha = 0^\circ$ and $\alpha = 3^\circ$, Matsumoto et al (2001)	102
Figure 5.7: The Aerodynamic derivative, A ₂ for Type 3, Matsumoto et al (2001)	103
Figure 5.8: Lateral flutter derivatives of Akashi-Kaikyo Bridge, Katsuchi et al. (1998)	104
Figure 5.9: Flutter analysis for the Golden Gate Bridge.....	112
Figure 5.10: Flutter Derivatives of the Golden Gate Bridge Jain et al (1998).....	113
Figure 6.1: Synthesized flutter derivatives	121
Figure 6.2: Flutter Analysis of the Golden Gate Bridge using the Flat Plate Theory.....	122
Figure 6.3: Synthesized flutter derivatives	123
Figure 6.4: Critical Frequencies versus critical reduced wind speed.....	123
Figure D.1: The Second Tacoma Narrows Bridge Grates	139

LIST OF TABLES

Table 4.1: Comparison between the experimental and the analytical frequencies	63
Table 4.2: Modal Frequency Identification of the TNB	64
Table 5.1: Golden Gate Bridge flutter analysis parameters	113
Table 6.1: Assumptions used to Synthesize flutter coefficients	120
Table 6.2: Flutter analysis of the Second Tacoma Narrows Bridge	124
Table E.1: Air parameters	146

DEDICATION

In memory of my late Mother, my family and all those who took time to help ...

CHAPTER 1

INTRODUCTION

1.1 Overview

Wind is the critical design component of suspension bridges. The failure of the First Tacoma Narrows Bridge, in November 1940, drew the attention of the impact of wind on these types of bridges. After the catastrophic failure of the bridge, wind tunnel testing became a standard method to assess the aerodynamic response of long-span bridges. Recent researches focus on analytical methods to evaluate the wind response of the bridge superstructures. The intention is to investigate alternative methods that estimate the critical wind speed.

The “Second” Tacoma Narrows Bridge, opened in October 1950, is designed using wind tunnel testing. The bridge is shown in Figure 1.1. The preliminary design configuration suggested installing open-grates, shown in Figure 1.2, along the bridge deck. This indeed improves the aerodynamic characteristics of the bridge. The United States Federal Highway Administration (USFHWA) and the Washington States Department of Transportation requested closing the open-grates to remodel the traffic lanes. Closing the gates will change the aerodynamic characteristics of the bridge. This research is conducted to assess the possibility of closing the open-grates of the bridge without adverse impact on the bridge aerodynamic stability.

The aerodynamic characteristics of the bridge under consideration are unknown. There is a need to analytically estimate the possibility of closing the open-grates of the

bridge without physically testing the bridge's superstructure. Two uncommon analytical approaches are suggested here to solve the problem:

- 1- To synthesize the aerodynamic coefficients of this type of superstructure and validate its appropriateness.
- 2- To use the fluid-structure-interaction procedure to estimate the wind response of the bridge and find its aerodynamic characteristics, , Bathe, K.J. and Zhang, H. (1999), Zhang, H. and Bathe, K.J. (2001) and Zhang H. (2003).

The first approach is extensively discussed here. The Theodorsen function is correlated to the aerodynamic derivatives of the open-truss stiffened decks. The approach is verified based on previous flutter analysis of the Golden Gate Bridge and is then applied to the bridge under consideration.



Figure 1.1: The Second Tacoma Narrows Bridge



Figure 1.2: The open grates of the Second Tacoma Narrows Bridge

The computational fluid dynamic approach was tested, using ADINA-F. Two bluff body models were chosen to verify the procedure, namely, a cylinder and an H-shape. The effort to capture the behavior of the vortex shedding phenomena and the response of an oscillating cylinder did not lead to any accurate results. Extensive effort was also spent to obtain the response of an H-shape section in wind, as described in Barriga-Rivera (1973), using this approach. The oscillatory response was significantly different from those of the experiments.

Moreover, this approach is found not to be completely robust and convergence is not always guaranteed. Several issues should be considered to account for the high degree of nonlinearity in solving the coupled fluid-structure systems. These include some modeling considerations such as discretization of the domain and the solution time step. The cost of running a two dimensional model with moderately fine mesh is very expensive. For

example, the time required to run one step of the H-shape problem, Barriga-Rivera (1973), using an Intel Centrino Duo[®] processor, with two cores 3.2 GHz speed, and sufficient RAM, is around 4 minutes. The appropriate time step is 1×10^{-5} second and the solution should be run for at least 10 seconds. Nevertheless, a three dimensional analysis is require, which makes the solution infeasible. While this approach was explored extensively in this research, it was later abandoned because of feasibility, software and hardware limitations issues.

For any type of aerodynamic analysis, the structural frequencies and the mode shapes of the bridge are important parameters in the method of analysis. In order to obtain these parameters a frequency analysis is required. In this research, a detailed finite element model of the bridge is developed to obtain an accurate estimate of the frequencies content of the structure.

1.2 Objectives

This research develops alternative analytical methods to supplement the wind tunnel testing, for estimating the critical wind speed of a bridge section with open-truss stiffened superstructure. The developed approach will be applied to the Second Tacoma Narrows Bridge to assess the flutter condition of the bridge after closing the existing deck grates.

1.3 Outline

This research is divided into two sections:

A- The first section discusses the theory of suspension bridges and their behavior.

B- The second investigates the classical flutter analysis and a method to solve the equation of motion of flutter. In each part the analysis theory is discussed first and then followed by the bridge's case study. A brief listing of the coming chapters and their content is as follows:

Chapter two starts with a historical review of the theory of the suspension bridges, starting from early attempts in 1800's and the several bridge catastrophes, to the evolution of the theory of suspension bridges and the aeroelasticity, and ending with the contemporary advancements in long-span bridges analysis and construction. The purpose of the chapter is to give an introductory review of the engineering experience in the development of suspension bridges.

Chapter 3 includes a discussion of the theory of suspension bridges with the structural analysis methods of cables. The emphasis is on the catenary cable profile and the associated modeling issues, such as the methods to evaluate the initial internal forces and the unstretched profile of cables. A finite element formulation of the three-dimensional catenary cable is investigated in detail. The chapter is concluded by a discussion of the frequency analysis of cabled structures.

The frequency analysis of the Second Tacoma Narrows Bridge is discussed in Chapter 4. The detailed finite element model developed and its structural components are described. The natural frequencies of the bridge and the mode shapes are compared with

previous analytical and experimental frequency analyses. The results are utilized in the flutter analysis.

Part two of the research starts by a literature review of the previous aerodynamic theories as discussed in Chapter 5. Various aerodynamic phenomena are described, highlighting the differences between them and presenting the pertained phenomenon to the problem under consideration. The pervious studies done on the aerodynamic coefficients of open-truss stiffened and plate-like superstructures are discussed. The discussion is then extended to synthesize the flutter derivatives of these types of decks based on the Theodorsen function. This is useful since the Theodorsen function provides a closed form solution of the flutter derivatives, as discussed in Appendix E. The derivation of the equation of motion of flutter condition for a two degrees-of-freedom system is shown. This chapter is concluded by a case study to verify the derived equation and the methodology that will be used in the following chapter.

Chapter 6 discusses the flutter analysis of the Second Tacoma Narrows Bridge. The synthesized flutter derivatives are listed and applied to the current bridge. A previous study done on the Golden Gate Bridge is used to verify this approach.

CHAPTER 2

THEORY OF SUSPENSION BRIDGES

2.1 Introduction

The construction of suspension bridges is well defined and such structures have been in use for decades. Simple suspension bridges, for use by pedestrians and livestock transportation, were constructed in the ancient Inca Empire, around year 1200 in South America, where ropes and wood were used to build bridges. Modern versions of suspension bridges started with iron chain bridges and then developed to use steel cables. This type of bridge is naturally aesthetic. Its catenary curve is the essence of its distinct identity and beauty. The use of suspension bridges *emerged* due to their enormous capacity to span long distance.

The advances made in the structural system and analysis methods of suspension bridges allowed constructing longer spans with better serviceability. Modern bridges are capable of carrying relatively heavy loads such as vehicles and light rail. The modern design procedures of suspension bridges are very advanced. However, there are accounts of success and failure that lead engineers to study the behavior of suspension bridges and their interaction with nature. The failure of the first Tacoma Narrows Bridge in 1947 is considered the pivotal point that changed the design of suspension bridges.

Modern suspension bridges are conceptually very similar. Typically, a suspension bridge consists of main towers that carry the main cables. The cables carry the deck loads via the

hangers, which connect the deck to the cables. The main cable transforms the vertical loads to tension load along its profile. Anchorages, at each side, provides the required support for the cables. Suspension bridges, however, might vary in detail, such as the number of spans, the type of anchorage, the type of deck, the configuration of hangers and cables, and the material used in construction. Figure 2.1 shows a schematic sketch of a typical suspension bridge, showing its main components.

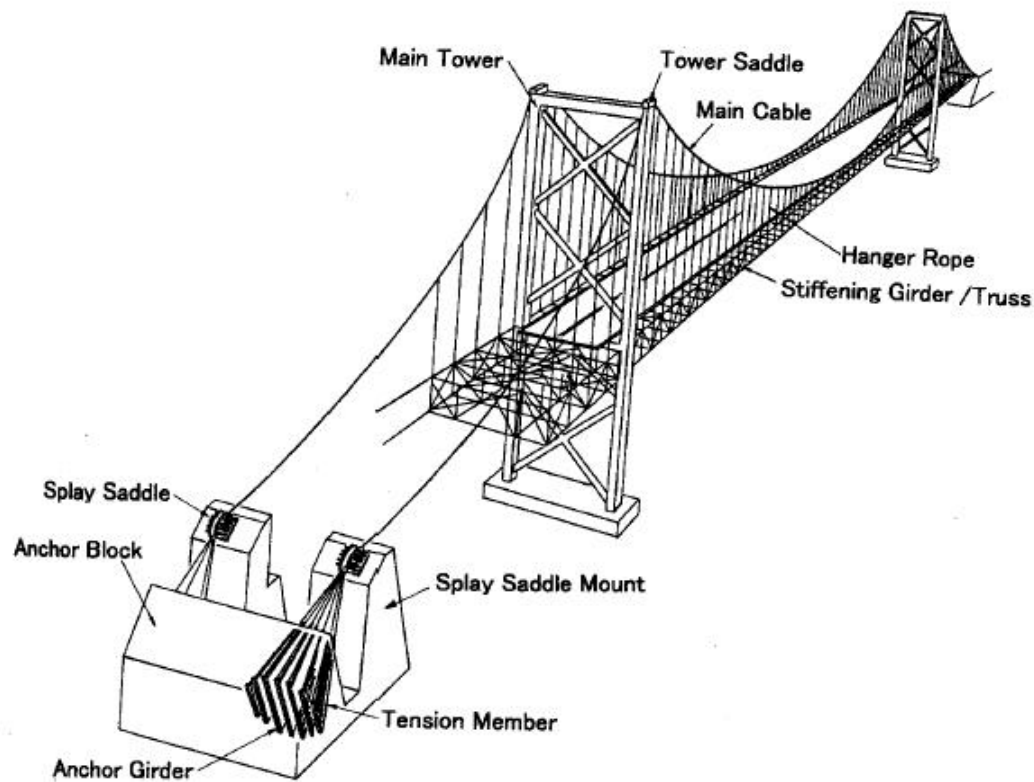


Figure 2.1: Suspension Bridges Components Chen and Duan (1999)

2.2 Needs and Uses

There are several advantages that justify the use of suspension bridges over other types of bridges. Considering ambient limitations, suspension bridges center span may be made very long in proportion to the amount of materials required, which is unlike other types of multi-span bridges. This is due to the fact that the center span weight is all suspended on the cable itself, which delivers the imposed loads it to the ground. This allows the bridge to economically span very wide canyons or waterways without the need to build intermediate supports or construct extremely deep middle span. Moreover, since the main towers are naturally required to be massive and tall to account for cable sag and to carry cable forces, it can be built high over water to allow the passage of very tall vessels, without significant increase in construction cost. Therefore, most of the bays and narrows nowadays are magnificently bridged with this type of structures.

Ambient limitations are not only a restriction for the structural layout but also for construction methods. If a structure is built over water, especially if deep, then it is required that neither temporary central supports nor access from beneath is required for construction. Construction of suspension bridges, as it will be briefly shown later, does not require any of the previous construction methods.

From a structural point of view, a suspension bridge uses the axial stiffness of cables. This type of structural elements has *membrane stiffness*, which increases the stiffness with increase of applied load. This allows carrying relatively heavy load with more utilization of the material. However, cables, as major structural elements, do not provide high overall stiffness to the structure. This has an advantage of being relatively flexible so the structure can flex under severe wind and seismic conditions, whereas a more rigid

bridge would have to be made much stronger and probably much heavier. One disadvantage of flexible structures is that they may become unusable in strong wind conditions and may require temporary closure to traffic.

2.3 History and Development

The attempt to erect suspension bridges goes back to the seventeenth century, where iron chain bridges were used. This was followed by the use of advanced structural elements such as cables. Accurate analysis theories related to the theory of structures and aerodynamic analysis was later applied after the collapse of Original Tacoma Narrows Bridge, in 1940. The introduced methods developed for long-span bridges led to the design of longer spans and more stable bridges.

The following is a brief review of the major suspension bridges and the development of analysis, design and construction techniques.

James Findlay (1756-1828) designed the first modern examples of long span bridges in the US. He introduced the Jacob's Creek, main span of 70ft, and Deer Island, main span of 240ft. However, in Findlay's days the theory of suspension bridges was not quite developed. Thus, he depended on some testing and on the basics of the elastic theory to analyze his structures. He developed bridges with relatively large stiffening truss, which were seemed over design.

Sam Brown (1776-1852) built a series of bridges in Britain, such as Union Bridge at Berwick with a main-span of 449ft, and the first long-span bridge in Britain to carry

heavy traffic. This achievement was possible because of his invention of using flat wrought iron eyebar to construct the main chain. He also introduced the first multi-span suspension bridges in Brighton and Firth of Forth in England. However, he wasn't successful in designing many bridges such as the Brighton Pier Bridge because of its collapse in wind. At that time, it was recorded by Russell that slender structures are susceptible to oscillation and he advised using diagonal stays and stiffening trusses to solve the issue.

Brunel (1806-1859), the designer of the Clifton Bridge with main span of 702ft, addressed the differences between catenary and parabola in cable profile. Up to that era suspension bridge theory was very primitive. Fundamental issues related to the real behavior of bridges components such as, the secondary or geometric stiffness of cables, were not properly appreciated. The Clifton Bridge oscillated under wind load and required retrofit work to stabilize it.

During that time French engineers were working on developing a new technology for the construction of suspension bridges. The Seguin brothers developed the use of wire rope to fabricate cables instead of links and chains. Vicat had first used a method to spin wire cables in-site. This new technology made the construction of the Fribourg Bridge in 1834 with a main span of 870ft, possible. The Fribourg Bridge was the longest suspension bridge in Europe until 1900.

The experience developed in France was then invested by the Americans to build their long-span bridges. Charles Ellet (1810-1862) considered the additional geometric

stiffness due to the gravitational load. He designed the wheeling bridge with main span of 1010 ft, which later failed in wind due to its low torsion stiffness. The bridge was rebuilt later by John Roebling (1806-1869). Roebling paid attention to the need of stiffness in the truss, although the concept of torsional stiffness was not clearly comprehended, until Rankine's theory was developed, which emphasized the importance of torsional stiffness in the design of suspension bridge superstructure. Roebling designed his bridges based on his intuitive engineering sense, before Rankine's theory, and his last accomplishment was Brooklyn Bridge with a main span of 1395ft, in 1883.

Other important theories were then developed and adopted in the design of suspension bridges. In 1888 Melan introduced the deflection theory which accounts for the effects of nonlinearity. Melan's theory is more logical than the Elastic theory to analyze cable deflection. The use of this theory built confidence for using high loads to stiffen the structure.

Leon Moisseiff adopted the deflection theory to design the Manhattan Bridge in 1909. The use of the deflection theory allowed him to design relatively long span bridges. Moisseiff then started to argue the possibility of building long span bridges with relatively slender superstructure, claiming that the stretched cables under the gravity load provide the adequate stiffness. Moisseiff implemented his thought in designating the first Tacoma Narrows Bridge with a main span of 2800 ft. His judgment was right regarding to the vertical stiffness; however, it ignored the importance of torsional stiffness. Besides, the H-shaped used in constructing the deck is quite undesired from aerodynamic perspective, an issue which was not understood at that time.

The bridge collapsed in wind, in November 1940. Although it was not the first suspension bridge to fail in wind, the failure of the first Tacoma Narrows Bridge invoked the need of understanding wind load on long-span bridges. The collapse of the first Tacoma Narrows Bridge took place with the evolution of aerodynamics research and the emerging aeronautical engineering science, in addition to wind tunnel testing, which was a newly applied technology in designing aircraft in the Second World War. This technology was transported to bridge engineering and used after 1950 as a standard requirement to test and design long-span bridges.

The preliminary conclusion of this implementation was the understanding of the importance of torsional stiffness of the superstructure. Plate girders and flat decks were avoided. The stiffening truss was the only superstructure configuration used in constructing suspension bridges, due to its substantial torsional stiffness. Consequently, the Second Tacoma Narrows Bridge was then built with 33ft stiffening truss in 1950. Other bridges were later constructed using stiffening trusses to provide sufficient torsional stiffness such as, the Forth Road Bridge in Scotland, 1958. The Golden-gate Bridge built in 1936 in San Francisco, with main span of 4200 ft, was later retrofit to improve its torsional resistance, where diagonal elements were added to connect the bottom cords of the truss.

The wind tunnel study done on the second Tacoma Narrows Bridge in 1950 by University of Washington proved improvement in aerodynamic characteristics of the

bridge when open-grates were used along the superstructure. Open-grates became the solution to improve deck aerodynamics. Another improvement of the truss aerodynamics was the introduction of a vertical stabilizer running longitudinally in the deck. This improvement was recently applied in the Great Belt Bridge and the Akashi-Kaikyo Bridge.

The shape of the superstructure was not appreciated until the first Severn Bridge was built in U.K, 1966, with main span of 5240ft. The original design used a stiffing-truss to support the deck. The model was destroyed by an accident in the wind tunnel. The designers then suggested using box-girder instead for testing for fast testing in the wind tunnel. The deck box section obtained was relatively streamlined, to reduce the drag and lift components. The wind tunnel test proved the merits of streamlined box-girders, which became the very first case to introduce closed-box section as tentative option of long-span superstructures.

After the 1970's the theory of suspension bridges and bridge aeroelasticity become more established. Construction techniques of casting caissons and steel fabrication of cables and tower elements improved significantly. This allowed building longer spans such as the Humber Bridge in England, 1981, with main span of 4626ft and the Great Belt Bridge built in 1986 with 5250 ft center span in Denmark, which is now considered to be the second longest span in the world.

Improving steel capacity made the Akashi-Kaikyo Bridge, built in Japan with 6558 ft main span, possible. The steel capacity was increased 10% more than the normally used steel for cables which is (260 ksi or 1800 MPa). In fact, ninety percent of the stress in the main cable of the Akashi-Kaikyo Bridge is due to its own weight. This implies that the design of longer spans is getting uneconomical, however, this opens the door for innovation in designing and optimizing bridge sections.

The awaited cutting-edge suspension bridge is the Messina Bridge in Italy, expected to be opened in 2012, that if completed will be about 2 miles long, that is around 60% longer than the current longest span in the world, the Akashi-Kaikyo Bridge. The optimized deck shape will allow this bridge to span that distance and carry six traffic lanes.

This shows that building a stable long suspension bridge depends on three factors, namely, the shape of the superstructure, the separation between the natural frequencies, and the material capacity used in construction.

CHAPTER 3

ANALYSIS METHODS FOR CABLED STRUCTURES

3.1 Introduction

A *Cable* is a structural element that can only resist tension forces. Applied vertical forces are transmitted to the cables as axial forces along their profile. The Geometry of the main cable is described by the final sag, which forms due to the cable self-weight and other sustained loads. The cable profile is, therefore, correlated to the applied external forces and the resulting internal forces.

Several theories were developed to investigate the actual shape of the main cable and to mathematically solve its parameters, such as internal forces and deflections. Earlier theories suggested a parabolic shape to map the shape of cables, loaded with a uniformly distributed gravity load. Catenary profile is, however, found to be the actual profile.

Classical theory of suspension bridges includes three formulations to estimate cable deflection and stiffness based on the elastic theory, linearized deflection theory, and the deflection theory. Other theories have been incorporated with other formulations to discretize the development of the force – displacement relationship and implement that relationship in finite element methods.

The following is a brief discussion of the classical theories and the modern analysis methods.

3.2 Theory of Cable

3.2.1 Cable Profile

To simplify the concept of a continuous cable element consider the free body diagram of a cable, which has the same shape as the actual cable and is mounted on simple supports, as shown in Figure 3.1. The load “ w ” has vertical and horizontal reactions at support A and a vertical reaction at B, where A is a hinge and B is a roller. The horizontal reaction H_A and the stabilizing force H_B are equal, and their magnitude is H . The cable profile must result a zero bending moment at any point on the cable.

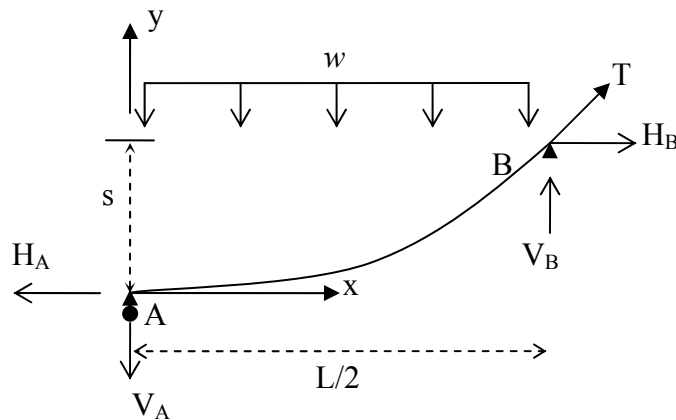


Figure 3.1: Rigid Cable Load

Based on these assumptions and by applying equilibrium and boundary conditions, the initial derivation of cable profile, under uniformly distributed gravity load, w , was found to be parabolic:

$$y = \frac{4.s}{L^2} x^2 \quad 2.1 - a$$

$$H = \frac{w.L^2}{8.s} \quad 2.1 - b$$

$$T = \frac{w.L}{2} \sqrt{\left(\frac{L}{4.s}\right)^2 + \left(\frac{2x}{L}\right)^2} \quad 2.1 - c$$

where, s is the sag, L is the span length of the parabola, w is the total gravity load distributed uniformly allover the cable length, and x and y are the horizontal and vertical distances, measured according to the reference point shown in Figure 3.2.

However later, it was realized that the real shape exhibited by cables, under gravity load, is the *catenary shape*. Schematic sketch of both profiles is shown in Figure 3.2. The reason that cables have catenary shape, rather than a parabolic shape, is that the weight should be uniformly distributed over the element length. This is more accurate than the assumption made in the derivation of Equations 2.1, where it was assumed that the infinitesimal weight resultant is distributed over its projection. Obviously, the catenary shape is the optimal shape taken naturally by the system to minimize its strain energy.

The catenary shape, as a mathematical expression, is some sort of hyperbolic sinusoidal function, or its equivalent exponent function, as expressed in Equation 2.2. For cables hung between two supports, with the same elevation y , the algebraic expression is :

$$y = a.(\cosh(x/a) - 1) = a.\left(\left(\frac{e^{x/a} + e^{-x/a}}{2}\right) - 1\right) \quad 2.2$$

where, a is the shape parameter, needed to be calibrated to obtain the profile shape.

Note if the target profile is known, an iterative procedure is required to obtain a . The coordinate system, x and y , is set up as shown in Figure 3.2. The cable profile and the

internal forces of the Second Tacoma Narrows Bridge are discussed in Chapter 3, showing the difference between both profile shapes.

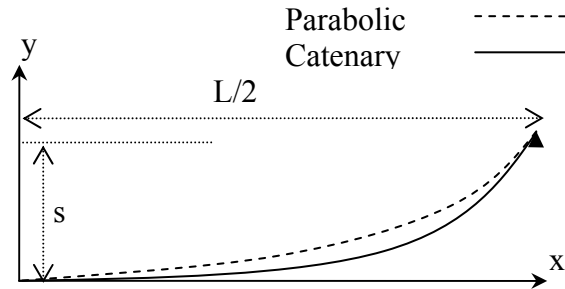


Figure 3.2: Catenary versus parabolic cable profile

3.2.2 Classical Theories

The first theory of suspension bridges was published by Rankine in 1858. The theory assumptions were made based on an abstraction of suspension bridges system, that is, a bridge comprising a straight and horizontal roadway slung from suspension cables and stiffened in some measures by longitudinal girders at the road level. The theory assumes that under total dead load the cable is parabolic and the stiffening girder is unstressed. Any partial or concentrated load on a platform must, by means of the girder, be transmitted to the “chain” in such a manner as to be uniformly distributed on the chain.

Rankine’s idea implies that the tension in the hangers should be the same under any type of loading, and that is, in a free-body diagram of the girder the hanger forces are assumed to be a uniformly distributed load along the span and acting upward. To achieve this assumption the girder should be sufficiently deep. This might be economic and

feasible for relatively short spans, that is, a few hundred feet long; but would be uneconomic for relatively longer spans.

The above assumptions were, mainly, applied to two well-known theories, the elastic theory and the deflection theory. The difference between them is whether cable deflection resulting from live load is considered. The bending moment equation along the stiffening girder and after applying the live load is evaluated and employed in the strain energy equations to derive the force – displacement relationship along the bridge span. This difference leads to a major discrepancy in both theories.

The inclusion of deformation in the deflection theory yields two main differences from the elastic theory. The first is that it reduces the bending moment of the stiffening girder. The second is that the derivation will be nonlinear and recursive, that is, the parameters of the strain energy equation is a function of its results. The nonlinearity of the deflection method makes the principle of superposition and influence line analysis inapplicable. Therefore, another theory was introduced to linearize the deflection theory by assuming that the ratio of the live load to the dead load is very small. This implies that the deflection is constant and is due to the dead load only.

Figure 3.3 shows a schematic sketch of the deflection-load ratio relationship estimated by the three theories. Note that the elastic theory over estimates the deflection, and the deflection theory has a very reasonable trend, while the linearized deflection theory lies somewhere between the two estimates.

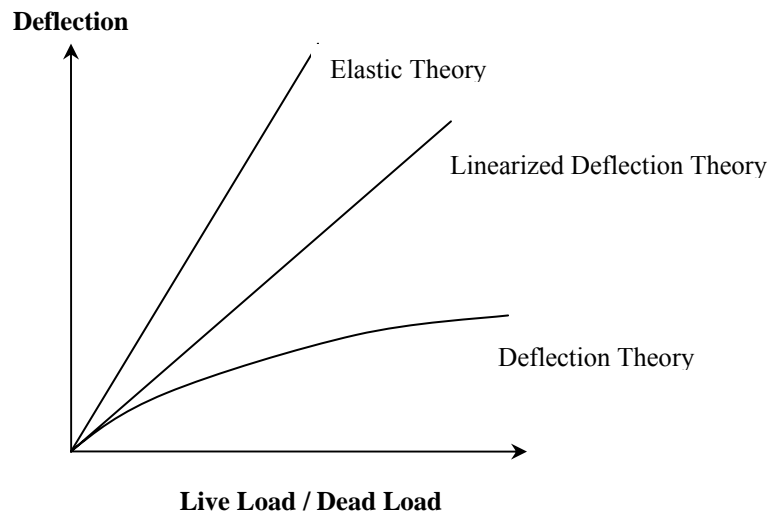


Figure 3.3: Deflection-load ratio relations among the theories

The out-of-plane forces are assumed to be transferred from the stiffening girder to the main cables. This analysis was first established by Moisseiff who assumed that the main girder always has larger deformation than the main cables.

Although these theories succeeded, to some extent, in designing the suspension bridges in mid 50's and until early 70's, finite element procedures became the powerful state-of-the art analysis method of suspension bridges.

3.2.3 Finite Element Analysis

The development of the finite element methods eliminated the restriction on the analysis of suspension bridges, and allowed accurate and detailed analysis. The cable

element is no longer assumed as a continuous element, the hangers are included as discrete entities, even the elements of the stiffening girders are modeled explicitly, three-dimensional analysis is possible, and all geometric and material variations along the span are accountable.

3.2.3.1 Modeling Issues

Modeling of suspension bridges can be done using a combination of different types of finite element modules and different analysis procedures. This depends on the type of the structural element being modeled, such as beam, cable or shell, the elasticity assumptions, the type of analysis required, such as dynamic, static or P- Δ analysis, and the stage of construction being modeled, such as, the initial construction stages or the final as-built analyses. The following discussion considers linear elastic finite element analysis of suspension bridges with an open-truss stiffening girder at the final, as-built, configuration. The discussion is mainly made to develop a finite element model to estimate the dynamic response of a bridge.

The level of modeling sophistication varies from a very simplified spine model, where the superstructure and the towers are lumped in discrete beam elements, called *spine elements*, to complete detailed finite element models, where every single element is explicitly modeled. The first approach was the most desirable in the early 70's and mid 80's, when the computer resources were very limited. A detailed model, however, is possible nowadays. A detailed finite element model of the Second Tacoma Narrows Bridge is discussed in the coming chapter. The frequency analysis results are compared

with frequencies obtained experimentally and with frequencies obtained from a previous study, done with less detail.

Detailed models are more accurate than condensed models. Detailed models are more capable of estimating stiffness and mass distributions along the structure. Spine models should be avoided in relatively flexible superstructures. That is because the estimation of the torsional stiffness of a spine element base on the cross sectional properties of the original configuration, is usually inaccurate especially when a segment of a space truss is being condensed. A magnification factor of the computed properties is usually applied to calibrate the element response. Another issue associated with the use of spine models is the difficulty of modeling the location of the center of mass and the center of rigidity of the element, which might affect the accuracy of a dynamic analysis.

Beam elements or truss elements can be used to model stiffening-truss girders. This depends on the type of joints connecting the elements. It is acceptable to model a truss using beam elements provided that all loads and masses are lumped at the joint, the stiffness of the elements is relatively close to one another, the bending stiffness of each element is relatively small compared to its axial stiffness and compared to the total bending stiffness of the truss, and the angles between the elements are not very large, less than 130° .

For elastic analysis, the conventional beam element, derived based on beam theory, is appropriate. The beam element could be used to model the superstructure elements and

the towers. Since the tower legs are usually substantial in dimensions, offsets or rigid links might be used to model the rigid joint effect at element intersections.

Modeling of cables requires special attention to two main issues. The first is the formulation of the element, and the second is the initial condition of the element. Cables, as described earlier, have unique nonlinear force – displacement behavior. The stiffness matrix of a cable element should be formulated accordingly, that is, to account for the geometric nonlinearity. The different ways to formulate a cable element are described in the coming section.

Since the stiffness of a cable element is a function of its internal forces, initial internal forces should be calculated. These forces are due to the deflection due to the self-weight of the cable and/or the total sustained load. The initial profile of a simply supported cable, under its own weight, will sag to its *final* or *target profile* due to the application of the sustained gravity loads. A *shape-finding* process is usually required to estimate the final shape of a cable and its associated internal forces. A brief discussion of this process is conducted in this chapter.

It is definite that the static analysis procedure of suspension bridges is nonlinear, where iterative procedures should be conducted to reach equilibrium at the final sag. Frequency analysis is usually conducted based on linear Eigenvalue analysis, where the initial conditions assigned are used in stiffness estimation. However, due to the considerable difference in the flexibility of the bridge components, such as the main cable

and the superstructure, the Ritz method is strongly recommended to eliminate local modes of vibrations, Chopra (2001).

3.2.3.2 Finite Element Formulation

The formulation of a cable element could be done in two different ways. The first one is based on the equivalent truss element, where the stiffness is derived by minimizing the strain energy of a line element, assuming linear shape function and non-linear second order strain function, Przemieniecki (1968). The result is a stiffness matrix which is function of the external deflections, i.e., the internal force in the element. The local tangent stiffness matrix of the equivalent truss element is:

$$K_t = \frac{EA}{L} + \frac{12T^3}{w^2 L^3} \quad 2.3$$

where, A is the cable cross section area, E is the modulus of elasticity, L is the length.

The first term in the above equation is the elastic stiffness and the second term is the geometric stiffness due to sag. Elements developed based on this formulation are called *linear cable elements*.

These types of elements are suitable to model straight tendons or cables with high tension, where the cable profile is almost linear. A cable with large sag or vertical deflection has a catenary profile, and thus an element formulated based on a linear shape function is not the best modeling choice.

For cables with large sag or large vertical deformation a catenary element should be used. The fundamentals of this element are discussed in Irvine (1981). Kim and Lee

(2001) briefly discussed the derivation of a two-dimensional catenary cable. The following is a detailed derivation of a three-dimensional elastic catenary cable.

The cable shown in Figure 3.4 is originally defined with unstretched length L_0 and two points i and j , defined in the fixed coordinate system x, y and z . Assume that in the initial equilibrium configuration the cable is subjected to six forces, F_1^o to F_6^o . The initial length of the cable is L_0 and the cross section is A_0 . The cable translation and a stretching, to i' and j' , is defined by the six displacements u_1 to u_6 , which is accompanied with six forces F_1 to F_6 . The Lagrangian (curvilinear) coordinate of an arbitrary point P on the cable element is s for the unstretched length, and p for the stretched length.

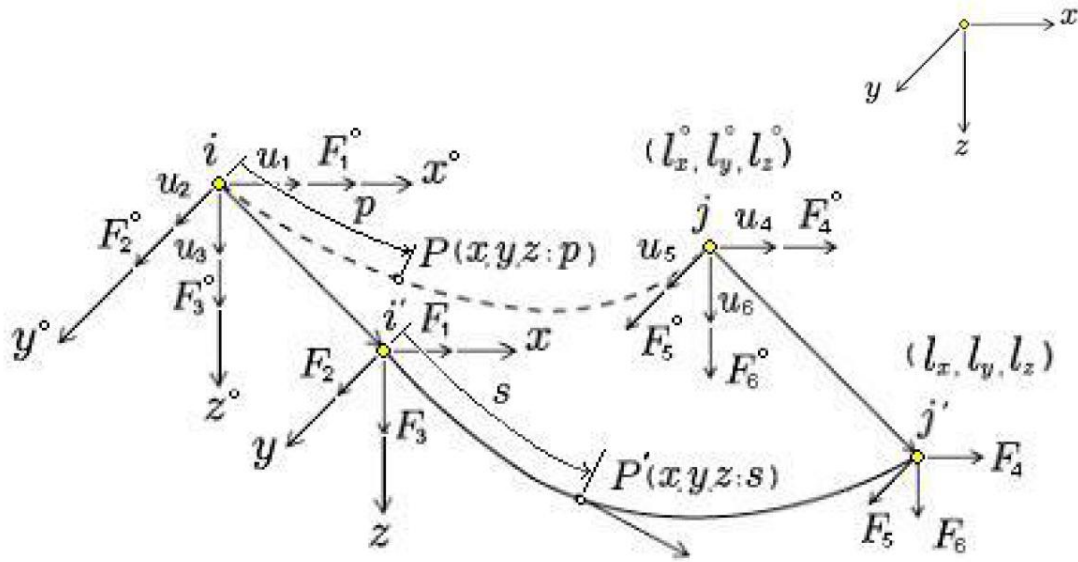


Figure 3.4: Catenary Cable Element subjected to nodal displacement

In this configuration of the cable element, the geometric constraints and the equilibrium conditions for tension forces, for infinitesimal length of the cable, are,

$$\left(\frac{dx}{dp}\right)^2 + \left(\frac{dy}{dp}\right)^2 + \left(\frac{dz}{dp}\right)^2 = 1 \quad 2.4$$

$$T\left(\frac{dx}{dp}\right) = -F_1$$

$$T\left(\frac{dy}{dp}\right) = -F_2 \quad 2.5$$

$$T\left(\frac{dz}{dp}\right) = -F_3 - ws$$

where, w is the weight of the cable per unit length. This implies the following,

$$T = \left(F_1^2 + F_2^2 + (F_3^2 + ws)^2\right)^{1/2} \quad 2.6$$

The nodal forces equilibrium and displacement compatibility conditions are,

$$F_4 = -F_1$$

$$F_5 = -F_2$$

$$F_6 = -F_3 - wL_0$$

$$l_x = l_x^0 + (u_4 - u_1) \quad 2.7$$

$$l_y = l_y^0 + (u_5 - u_2)$$

$$l_z = l_z^0 + (u_6 - u_3)$$

The relationships between the undeformed Lagrangian coordinate s and Cartesian coordinate are,

$$x(s) = \int \frac{dx}{ds} ds$$

$$y(s) = \int \frac{dy}{ds} ds \quad 2.8$$

$$z(s) = \int \frac{dz}{ds} ds$$

A constitutive relation that is a mathematically consistent expression of Hooke's law is

$$T = EA_0 \left(\frac{dp}{ds} - 1 \right) \quad 2.9$$

Therefore, from Equations 2.5 and 2.9, the following could be derived,

$$\begin{aligned}\frac{dx}{ds} &= \frac{dx}{dp} \frac{dp}{ds} = -\frac{F_1}{T} \frac{dp}{ds} = -\frac{F_1}{T} \left(\frac{T}{EA_0} + 1 \right) \\ \frac{dy}{ds} &= \frac{dy}{dp} \frac{dp}{ds} = -\frac{F_2}{T} \frac{dp}{ds} = -\frac{F_2}{T} \left(\frac{T}{EA_0} + 1 \right) \\ \frac{dz}{ds} &= \frac{dz}{dp} \frac{dp}{ds} = -\frac{(F_3 - ws)}{T} \frac{dp}{ds} = -\frac{(F_3 - ws)}{T} \left(\frac{T}{EA_0} + 1 \right)\end{aligned}\tag{2.10}$$

Substituting the Equations 2.10 in 2.8 and integration with respect to s gives,

$$x(s) = -\frac{F_1 s}{EA_0} - \frac{F_1}{w} \left[\sinh^{-1} \left(\frac{F_3}{F_1} \right) - \sinh^{-1} \left(\frac{F_3 + ws}{F_1} \right) \right]\tag{2.11}$$

which are equivalent to,

$$x(s) = -\frac{F_1 s}{EA_0} - \frac{F_1}{w} [\ln\{F_3 + ws + T\} - \ln\{F_3 + T\}]\tag{2.12}$$

Working out for the other directions,

$$y(s) = -\frac{F_2 s}{EA_0} - \frac{F_2}{w} [\ln\{F_3 + ws + T\} - \ln\{F_3 + T\}]\tag{2.13}$$

$$z(s) = -\frac{F_3 s}{EA_0} - \frac{ws^2}{2EA_0} - \frac{1}{w} \left[T - \{F_1^2 + F_2^2 + F_3^2\}^{1/2} \right]\tag{2.14}$$

The boundary conditions at the cable ends are,

$$\begin{aligned}x = 0, y = 0, z = 0, p = 0 \text{ at } s = 0 \\ x = l_x, y = l_y, z = l_z, p = L \text{ at } s = L_0\end{aligned}\tag{2.15}$$

Applying the boundary conditions gives the following,

$$\begin{aligned}l_x &= -\frac{F_1 L_0}{EA_0} - \frac{F_1}{w} [\ln\{F_3 + wL_0 + T\} - \ln\{F_3 + T\}] \\ l_y &= -\frac{F_2 L_0}{EA_0} - \frac{F_2}{w} [\ln\{F_3 + wL_0 + T\} - \ln\{F_3 + T\}] \text{ or } i \\ l_z &= -\frac{F_3 L_0}{EA_0} - \frac{wL_0^2}{2EA_0} - \frac{1}{w} \left[T - \{F_1^2 + F_2^2 + F_3^2\}^{1/2} \right] \\ T &= \{F_1^2 + F_2^2 + (F_3 + wL_0)^2\}^{1/2}\end{aligned}\tag{2.16}$$

To implement the finite element procedure, the nodal forces have to be expressed with respect to the global nodal displacements of the element. Note that the above nonlinear relations satisfy this requirement. Applying an incremental procedure using the first order Taylor expansion, with respect to the unknowns F_1 , F_2 , and F_3 the following expression is obtained,

$$\begin{aligned} dl_1 &= \frac{\partial l_1}{\partial F_1} dF_1 + \frac{\partial l_1}{\partial F_2} dF_2 + \frac{\partial l_1}{\partial F_3} dF_3 \\ dl_2 &= \frac{\partial l_2}{\partial F_1} dF_1 + \frac{\partial l_2}{\partial F_2} dF_2 + \frac{\partial l_2}{\partial F_3} dF_3 \\ dl_3 &= \frac{\partial l_3}{\partial F_1} dF_1 + \frac{\partial l_3}{\partial F_2} dF_2 + \frac{\partial l_3}{\partial F_3} dF_3 \end{aligned} \quad 2.17$$

Or in matrix form

$$\begin{Bmatrix} dl_1 \\ dl_2 \\ dl_3 \end{Bmatrix} = F \begin{Bmatrix} dF_1 \\ dF_2 \\ dF_3 \end{Bmatrix} \quad 2.18$$

Where F is the nodal flexibility matrix, defined as follows:

$$F = \begin{Bmatrix} \frac{\partial l_1}{\partial F_1} & \frac{\partial l_1}{\partial F_2} & \frac{\partial l_1}{\partial F_3} \\ \frac{\partial l_2}{\partial F_1} & \frac{\partial l_2}{\partial F_2} & \frac{\partial l_2}{\partial F_3} \\ \frac{\partial l_3}{\partial F_1} & \frac{\partial l_3}{\partial F_2} & \frac{\partial l_3}{\partial F_3} \end{Bmatrix} = \begin{Bmatrix} f_{11} & f_{12} & f_{13} \\ f_{21} & f_{22} & f_{23} \\ f_{31} & f_{32} & f_{33} \end{Bmatrix} \quad 2.19$$

The forces are equal to

$$\begin{Bmatrix} dF_1 \\ dF_2 \\ dF_3 \end{Bmatrix} = K \begin{Bmatrix} dl_1 \\ dl_2 \\ dl_3 \end{Bmatrix}, \quad K = F^{-1} \quad 2.20$$

where K is the nodal stiffness matrix.

The components of the flexibility matrix in the above equations are,

$$\begin{aligned}
f_{11} &= -\frac{L_0}{EA_0} - \frac{1}{w} [\ln\{F_3 + wL_0 + T\} - \ln\{F_3 + A\}] \\
&\quad - \frac{F_1^2}{w} \left[\frac{1}{T^2 + (F_3 + wL_0)T} - \frac{1}{A^2 + F_3A} \right] \\
f_{12} &= f_{21} = -\frac{F_1F_2}{w} \left[\frac{1}{T^2 + (F_3 + wL_0)T} - \frac{1}{A^2 + F_3A} \right] \\
f_{13} &= -\frac{F_1}{w} \left[\frac{F_3 + wL_0 + T}{T^2 + (F_3 + wL_0)T} - \frac{F_3 + A}{A^2 + F_3A} \right] \\
f_{22} &= -\frac{L_0}{EA_0} - \frac{1}{w} [\ln\{F_3 + wL_0 + T\} - \ln\{F_3 + A\}] \\
&\quad - \frac{F_2^2}{w} \left[\frac{1}{T^2 + (F_3 + wL_0)T} - \frac{1}{A^2 + F_3A} \right] \\
f_{23} &= \frac{F_2}{F_1} f_{13} \\
f_{31} &= -\frac{F_1}{w} \left[\frac{1}{T} - \frac{1}{A} \right] \\
f_{32} &= \frac{F_2}{F_1} f_{31} \\
f_{33} &= -\frac{L_0}{EA_0} - \frac{1}{w} \left[\frac{F_3 + wL_0}{T} - \frac{F_3}{A} \right] \\
A &= \{F_1^2 + F_2^2 + F_3^2\}^{1/2}
\end{aligned} \tag{2.21}$$

It should be reemphasized that tension elements are different from those of cables. Modeling suspension bridges requires software with the catenary element formulation. There are very few structural analysis packages that adopt the above formulation. MIDAS – Civil developed by MIDAS Information Technology Co., Ltd. is used in this research due to its ability to properly model cable elements. The software also has an optimization procedure that estimates the initial tension in the cables of suspension bridges and cable stayed bridges.

3.3 Shape-Finding

The cable element is the most difficult part in the modeling process of suspension bridges. The initial internal forces in the cable are of importance. If an as-built bridge is being modeled, such as the problem in this research, the internal forces in the cable, due to the sustained loads, should be estimated. In order to do so, an iterative procedure should be conducted to evaluate the internal forces at equilibrium when full dead load is applied. There are several ways to find the target profile of a cable and to estimate the initial tension force. The *forward incremental method* and the *backward-loading method* are discussed here.

The forward incremental method is the simplest, yet the least accurate method to estimate the final profile. In this method, dead load is applied incrementally on the target profile. At each increment deflection and internal forces are computed and then the cable is modified to a new profile, by trial and error, to restore the original sag under the applied load increment. A new increment starts with accumulating the computed internal forces. This procedure would not reach an exact solution. However, sufficiently small load increments might yield to an acceptable solution.

An improved analytical procedure of the incremental equilibrium equation is proposed by Kim and Lee (2000). The Newton-Raphson method is used to find the target configuration of cable-supported structures under dead loads. Linearized equilibrium equations of the catenary cable element, which includes the nodal coordinates and the unstrained length as unknowns, are formulated using analytical solution of the elastic catenary cable.

The backward-loading method is also an incremental method. The procedure is conducted in a reversed iterative manner, unlike the typical incremental method. A full model of the bridge is initially modeled without any loads being assigned. Approximated but realistic initial tensions are initially assigned. These values could be obtained from simplified calculations using the elastic theory, where dead load is fully applied. The segments of the superstructure are then removed stage by stage, in a symmetric and systematic fashion. At each stage the equivalent gravity load of the removed panel is substituted by an upward force on the main cable. The process is continued and the stress and deflection computed in each stage are accumulated to the next stage. The procedure is repeated until all the elements of the superstructure are being removed. The outcomes of this process are the initial sag of the main cable and the initial setback of the main towers. The results can be refined by subtracting the residual internal tension forces, after removing the whole deck elements, from the initially assumed tensions. Then the difference is assumed to be the initial tension force and the process is repeated. This method requires software with a cable element formulation and stage-construction features, as in MIDAS-Civil.

3.4 Frequency Analysis

Frequency analysis is conducted to estimate the frequencies of the different modes of vibration of the structure and the associated mode shapes. The different frequencies are used in solving the equation of motion at critical condition. The mode shapes are important to identify the direction of the vibration, such as torsional or vertical vibration, and to estimate the generalized properties of the structure which represent the equivalent

single-degree-of-freedom effect of a certain mechanical property, such as mass or stiffness.

3.4.1 Eigenvalue analysis

The developed detailed model of this research has more degrees of freedom than needed for accurate frequency analysis. Including numerous number of degrees of freedom connecting relatively flexible elements generates local modes of vibration. A traditional procedure to solve the Eigenvalue problem of the equation of motion will yield a local mode of vibration in the solution, and thus a large number of modal vectors should be solved to reach the desired set of global response.

In order to eliminate this issue, the *Ritz vectors* procedure, which is based on the Rayleigh-Ritz method, is used. The Ritz method estimates certain numbers of mode shape vectors and then estimates the natural frequencies using the estimated vectors. A load vector should be assigned to depict the spatial distribution and direction of the fundamental mode shape. The initial Ritz vector is obtained using static linear analysis of the assigned Ritz load vector. The other vectors are estimated based on the initial vector using mass orthonormality (*see Chopra (2001)*).

3.4.2 Averaged Mechanical Properties

Structural properties, such as mass or stiffness, could be averaged, at a certain mode i , by using the mode shape ϕ_i , along the structure, as shown in Equation 2.22.

$$m_e = \frac{\int_0^l m(x) \phi_i^2(x) dx}{\int_0^l \phi_i^2(x) dx} \quad 2.22$$

where m_e is the equivalent property of $m(x)$ along the structure length. This formula is useful when the mass distribution is not uniform over the structure length. Having the mass as approximately uniformly distributed over the distance x , the average distributed mass per unit length is the same as $m(x)$ per unit length.

The average mass moment of inertia I_e could be calculated using the width of the superstructure as follows,

$$I_e = \frac{\int_0^l m(x) \phi_i^2(x) B^2 dx}{\int_0^l \phi_i^2(x) dx} \quad 2.23$$

Coupling between modes might take place in random vibration and self-induced forces. The coupling co-efficient between mode i and mode j with respect to mode j is expressed as follows

$$C_{i,j}^i = \frac{\int_{Deck} \phi_i(x) \phi_j(x) dx}{\int_{Deck} \phi_i^2(x) dx} \quad 2.24$$

The product $C_{ij}^i C_{ij}^j$ represents the potential of a mode, i , to be coupled with another mode, j , when the lower mode is excited. The potential of having two modes to be coupled is represented by the magnitude of the coefficient. The value of the coupling

coefficient is always assumed to be positive, since the sign of a mode shape vector can be reversed.

A MATLAB code is developed to calculate the coupling coefficient of vertical and torsional modes, *see Appendix B.1*.

CHAPTER 4

ANALYSIS OF THE TACOMA NARROWS BRIDGE

4.1 Problem

The frequency analysis of the bridge is required to be used in the flutter analysis. The frequencies and the mode shapes are essential parameters in the aerodynamic analysis. This analysis is also required if the research topic is expanded to include health mentoring analysis or computational fluid dynamic. A detailed finite element model is developed to conduct the analysis.

The structure is assumed to operate within the elastic limit. Therefore, linear elastic material is assumed, and only geometric nonlinearity is considered. This chapter summarizes the procedure taken to develop and calibrate a detailed finite element model for the existing bridge and includes the frequency analysis results.

The formulation and the analysis used here are to provide methodologies for assessing wind response of bridges. The model is used to assess the impact of structural alterations such as closing the open-grate segments along the deck without adversely affecting the wind response characteristics. While these alterations affect the aerodynamic characteristics, the structural properties, such as frequency content, remain significantly unchanged.

4.2 Previous Research

Several studies were conducted on the existing Tacoma Narrows Bridge by universities and engineering firms. A wind tunnel testing of the bridge in its initial design stages was conducted by Farquharson in 1954. The study investigated the aerodynamic effect of closing the grates in the bridge deck. It was concluded that open-grates improve the behaviour of the bridge. Although the study did not recommend closing all the grates, no specific critical wind speed was investigated.

Arvid Grant Associates and OPAC Consulting Engineers (1993) developed a finite element model. The study includes complete calculations of the geometric properties of the structural elements and estimations of the initial forces in the cables. SAP 2000 was used in the development of the model.

Arvid Grant Associates and OPAC-Geospectra (2003) conducted a supplemental study on seismic evaluation of the Tacoma Narrows Bridge. The study included identification of seismic hazards at the bridge site, identification of the response frequencies, analysis of the bridge under ground motion and identification of structural deficiencies. Ambient vibration measurements, which provide experimental frequencies and estimations of the structural damping, are incorporated. These studies were found to be very useful to verify the results obtained in this research.

4.3 Description and Specifications

The Second Tacoma Narrows Bridge is a suspension bridge with main span of 2800 ft and two side spans of 1100 ft each, spanning the eastern shores of Puget Sound and Kitsap Peninsula with a four-lane roadway, with total width of 60 ft. The bridge is a segment of the state highway route 16, in Washington State, traveling east-west.

The structure is made of steel, except for the roadway deck and the anchors which are made of concrete. The superstructure is made of a stiffening truss which is 33 ft deep and is strengthened by diagonal bracings. A series of floor trusses, running along the span, carry the roadway deck and transfer the load to the hangers. Figure 4.1 shows the main structural elements of the superstructure, demonstrating the mentioned components. Elements are displayed in sequence to avoid view congestion. The roadway is not modeled in this study as explained later in this chapter.

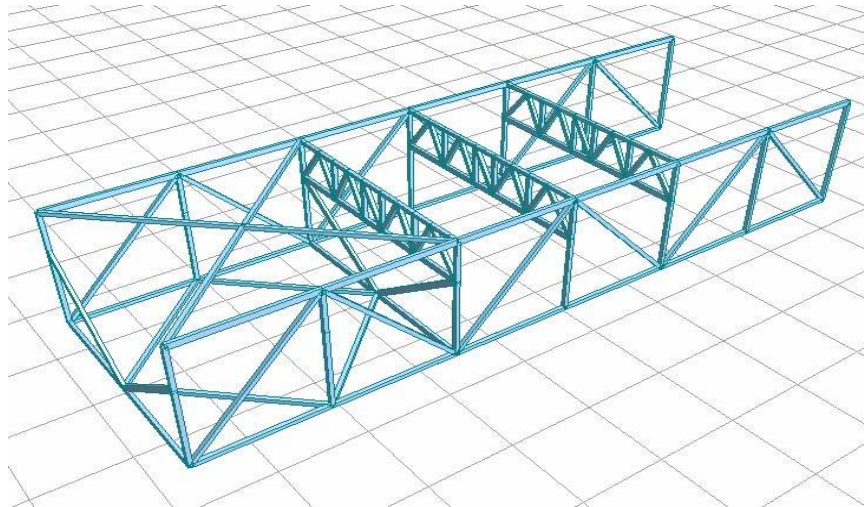


Figure 4.1: Section of the Second Tacoma Narrows Bridge Suspended Structure.

The two main towers, 467.04 ft high, support the main cable, which sags 280 ft. Both of them stand on top of the retrofitted piers of the collapsed structure, which is dug embedded over 200 ft in the narrows basin.

Figure 4.2 shows the elevation view of the structure, split into two parts for clarity. The structure consists of (viewed from west to east, i.e. from left to right), the following components: one 162.5 ft west anchorage, three 150 ft steel deck girder approach spans, 1,100 ft cable suspended steel side span, 2,800 ft cable suspended steel main span, 1,100 ft cable suspended steel side span, 45'-2-1/2" reinforced concrete T-beam approach span, 42' 5" reinforced concrete T-beam approach span, 45 reinforced concrete T-beam approach span and 185 ft east anchorage. The total length of the suspended structure is 5,000 ft.

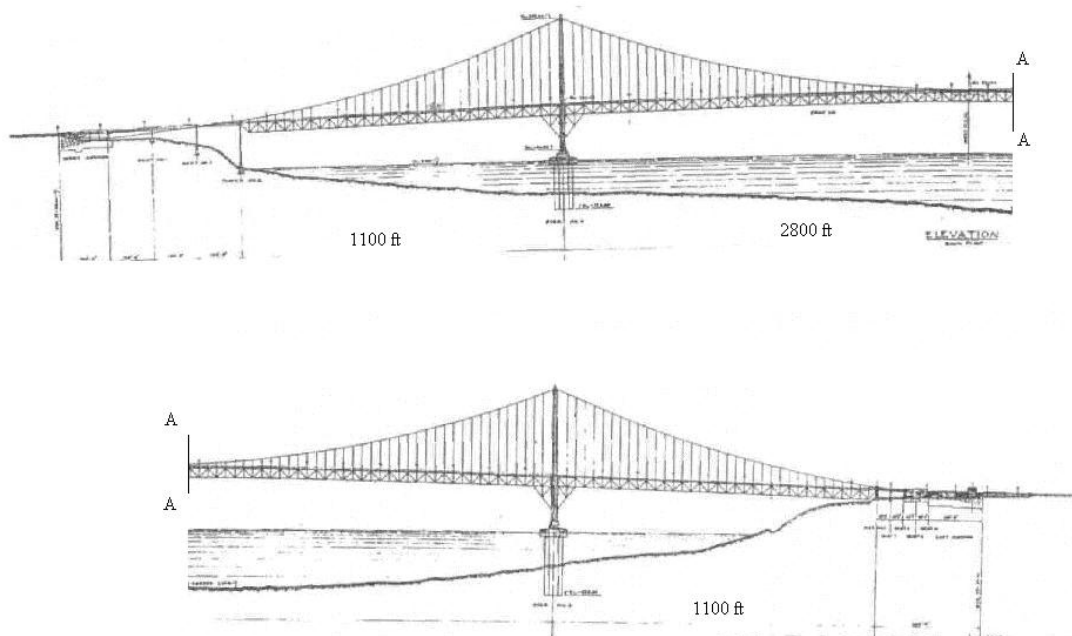


Figure 4.2: Existing Tacoma Narrows Bridge Elevation View.

The deck width is 46'-8 1/8" which includes four 9 ft lanes separated by 2.75 ft slotted wind grates and 1'-7" wind grates separating the roadway from the sidewalks. In addition there are two 3.5 ft sidewalks, one on each side of roadway, and the width between the suspension cables is 60 ft, as shown in Figure 4.5. The two main cables are 20.25 inches in diameter.

The tower's total length is 467.04 ft, measured from the pier face. The tower's legs are made of steel segments, which are made of built-up sections of five rectangular chambers arranged in cross-shape. The tower legs are tapered. The first 141.5 ft have a parabolic tapering, $0.001x^2$ (ft), and the other segments are linearly tapered up to the top of the tower. The legs are connected with lateral and diagonal bracings. Figure 4.4 shows the elevation and the side views of the main tower.

The stiffening trusses are connected to the main tower legs at two points as shown in the side view in Figure 4.4. A diamond-shaped truss element assembly embraces a giant damper which is embedded inside each tower leg and connected to the upper cord of the stiffening truss. Another assembly of truss elements connects the lower cord of the stiffening truss to the face of the tower leg via a viscous damper. Both assemblies are designed to dissipate any excessive excitation along the longitudinal direction of the stiffening truss. The stiffening trusses are also connected to the middle part of the tower via the horizontal upper chord bracings which connect the site of the upper cord to the stiffening trusses. A "windshoe" is designed at the point where the upper chord bracings are connected to the main tower lateral beam. The windshoe is simply a gap element

which allows movement along the bridge deck and around the tower axes. The other displacements in the other degrees of freedoms are restrained.

The side spans have a linear slope of 3%. The main span is parabolic with 21 ft difference in elevation between its ends at the towers and its mid span. It consists of 88 bays spaced at $30' - 10 \frac{5}{8}"$ along the center span. The spacing of bays along the side spans is $30' - 3 \frac{3}{8}"$.

4.4 Finite Element Model

The choice of the finite element procedure is very important issue in the analysis of suspension bridges. There are very few computer software packages that explicitly support catenary cable element formulation. Procedures that do not support this feature require special analysis procedure to obtain relatively close results.

The SAP 2000 was initially used for this purpose. However, the results from the dynamic and the static analyses were inaccurate. It is found that SAP2000 does not support explicit features to handle catenary cable elements and only supports non-linear truss elements. Therefore prior to conducting frequency or dynamic analyses, it is required to conduct a shape-finding analysis to determine the unstrained profile, followed by a static stage construction analysis to build up the nonlinear geometric stiffness. Furthermore, special constraints should be artificially added to the model to prevent local instability.

A detailed finite element model is developed using MIDAS-Civil. The software has very specialized features for cable elements and modeling of a suspension bridge. As-built-configuration was successfully used with pre-calculated initial tension to account for the geometric stiffness and to conduct the dynamic analysis.

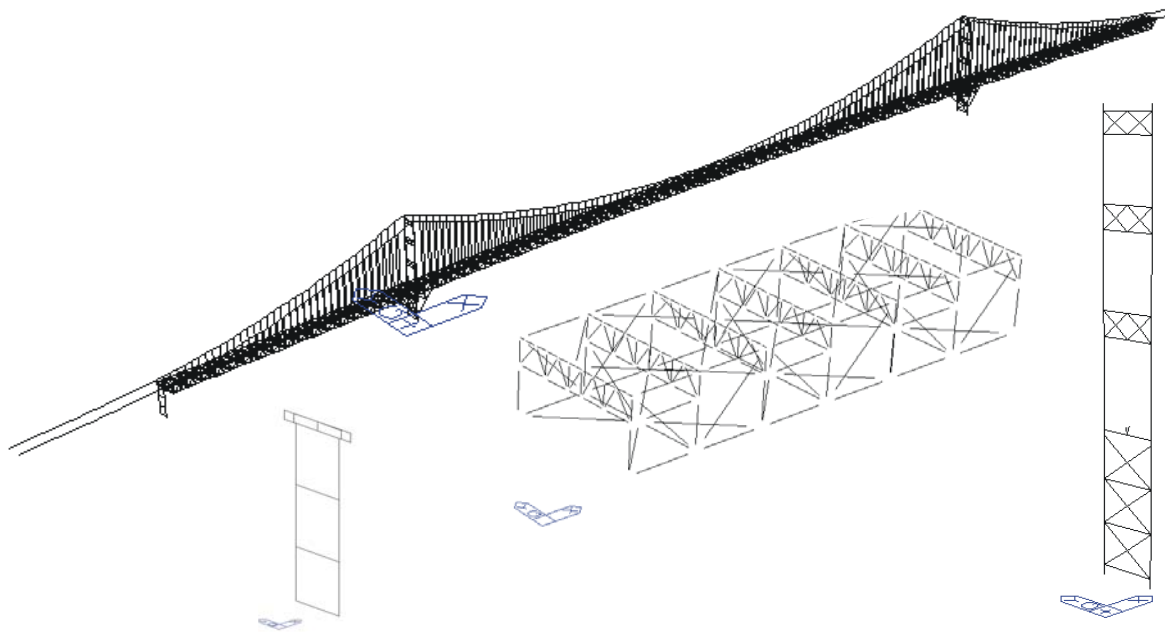


Figure 4.3: The Detailed Finite Element Model of the Tacoma Narrows Bridge

Figure 4.3 shows a general view of the finite element model with pull-outs for the main tower, the west tower and the superstructure. Note that the approaches, shown in Figure 4.2, are not included. The main cable is extended to where it terminates at the anchorage. The V-shape element, in the middle of the main tower, made of two rigid elements connecting the top cord of the superstructure with the tower.

The cross sectional properties of each segment are calculated and assigned to the finite element model. The software used to model the bridge, MIDAS-Civil, supports tapered section calculation. The cross section properties calculations proposed in the OPAC Consulting Engineers (1993) study were adopted to develop the model.

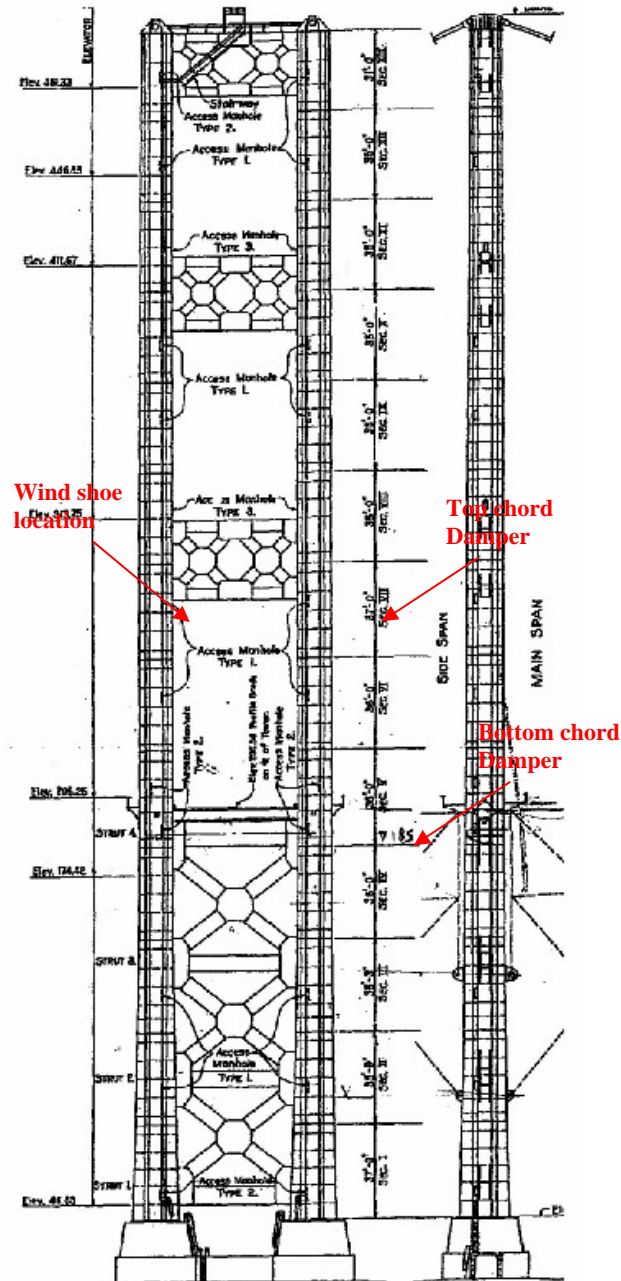


Figure 4.4: TNB Main Tower Elev. and Side views

All elements are modeled based on their centrelines. Therefore, offsets are assigned to diagonal and lateral beam bracings to account for the rigid end effect.

4.4.2 Stiffening Truss

The stiffening trusses are parallel two-plane-trusses that span along the bridge length, as shown in Figure 4.1. In the bridge under consideration, they are divided into three spans, a main span with 2800 ft in length and two side spans with 1100 ft in length. The stiffening truss elements are modeled using *beam elements*. The properties of the cross sections are calculated and compared with OPAC (1994) study and are found to be accurate.

4.4.3 Floor Truss

In suspension bridges, floor trusses are used to connect the stiffening trusses and to support the roadway deck. Previous studies condensed the structural properties of the floor truss into a single beam element, or a spine element, which was used in the global model. While this approach reduces the number of the degrees of freedom, the accuracy of the solution is also slightly diminished. Figure 4.5 shows the geometric configuration of the floor truss.

In this study the floor beams are considered in detail. For simplicity in modeling and to guarantee stability in the numerical procedure of the finite element analysis, the floor truss elements are treated as beam elements. This assumption is verified using a separate

model, such that, the maximum difference in axial load in each element due to the sustained loads is measured. The difference was found to be around 8%.

The roadway stringers, which carry the roadway slab and transfer its load to the floor truss, are eliminated. It is assumed that their contribution to the superstructure stiffness is negligible. However, they contribute to the gravity load and the mass. Removing these elements from the finite element model reduces the computational effort substantially. Their weights and masses are lumped on the nodes of the upper cord of the floor truss.

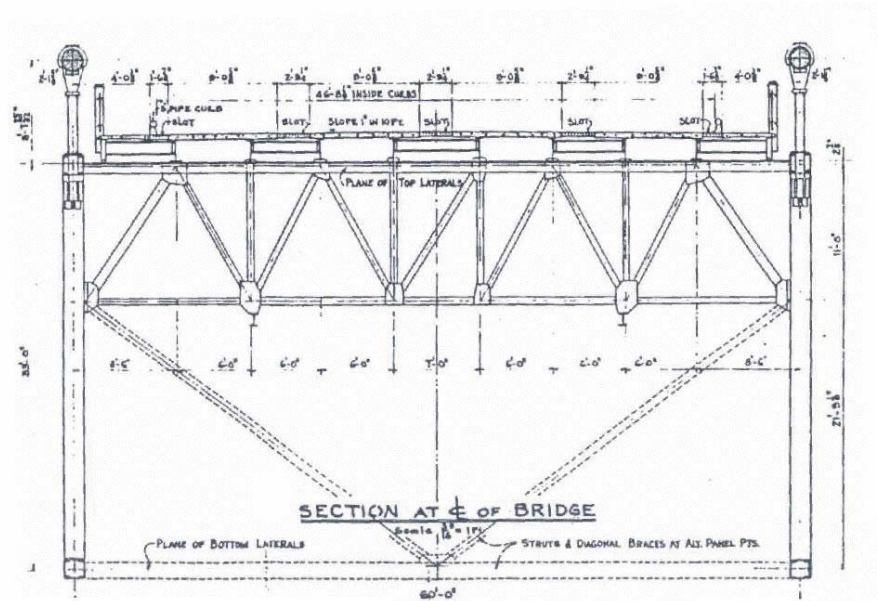


Figure 4.5: Tacoma Narrows Bridge Floor Truss.

4.4.4 Main Cable

Three main issues are considered in modeling the main cable, namely, sectional property, shape or profile finding and internal forces. The last two issues are interrelated, since the internal tension force is a function of the cable sag, which in turn determines the profile of the cable.

The main cable is made of bundles of 19 strands with each strand consisting of 464 wires. The total cross sectional area of the cable is found by summing up the total area of the wires in the cross section. A 1.773 ft² net cross sectional area is used to model the main cable, with a modulus of elasticity of 29,000 ksi. An alternative approach is to use the gross area and modify the modulus of elasticity of the cable elements.

The cable profile is determined by the sag and the span length. In this study the final sag is known to be 280 ft and the mid span length is 2800 ft. There are two types of cable profiles, the *catenary profile* and the *parabolic profile*. Although it is known that a cable element has a catenary profile, both profiles are calculated here and are compared as shown below.

The parabolic profile of the bridge is expressed as follows:

$$y = \frac{4 \times 280}{2800^2} x^2 = \frac{1}{7000} x^2 \quad 4.1$$

This equation applies on both the side-span and the main-span cable profiles such that the coordinate system is set at the vertex of the polynomial. Derivation of the side-span profile is discussed in Appendix C.

The catenary profile of the bridge is found by trial and error and is expressed as follows:

$$y = 3545.708.(\cosh(x / 3545.708) - 1) \quad 4.2$$

where, x and y are measured in feet. The coordinate system, x and y , set up is shown in Figure 4.6.

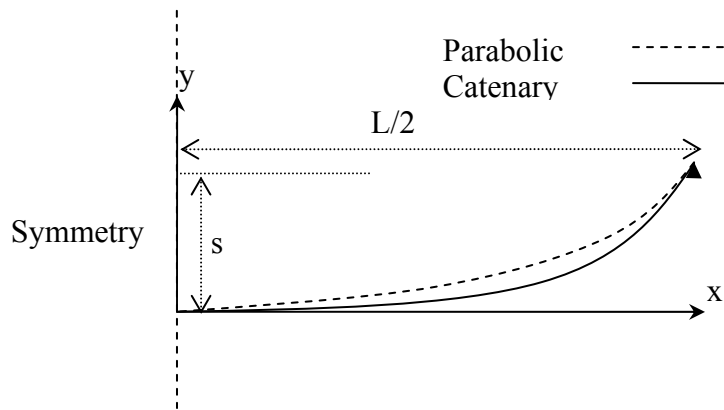


Figure 4.6: Catenary versus parabolic cable profile

Figure 4.6 shows a schematic sketch for the two cable profiles, showing one half of the main cable profile. The difference between the parabolic and the catenary profiles is very small and scaled sketch barely depicts the discrepancy. Figure 4.7 shows the difference between the two profiles. It is assumed that the catenary cable is the base line profile and the difference, in feet, is calculated along the span length as shown in Figure 4.7. The maximum difference between the two profiles is 0.905 ft at 989 ft from the span centerline. If the maximum difference of the two profiles is normalized based on the sag, then it could be shown that the difference between the two profiles is negligible.

To estimate the average load of the superstructure, a single panel of the deck was modeled. It is found that the average uniformly distributed dead load (w) is 10.4 kips/ft, that is 5.2 kips/ft per cable. Thus the total dead load carried by each cable is 15,162 kips. The Maximum tension expected based on the parabolic profile formulation is 19,602

kips. From the finite element analysis it is found that the maximum tension is 20,277.1 kips, which is 3% greater than the estimated value. The horizontal forces are estimated to be 18,200 kips based on the parabolic profile formulation. From the elastic first order finite element analysis it is found to be 18,948.72 kips, which is around 4% greater than the estimated value.

The difference between the estimated values based on the parabolic formulation and the finite element analysis is not considerable. This verifies the estimation of the internal forces and the profile shape. The estimation of the cable internal forces has significant effect on the stiffness of the cables and thus the overall accuracy of the frequency analysis. Figure 4.8 shows the distribution of the ratio of the tension force in the cable to the total weight of the superstructure along half of the cable span.

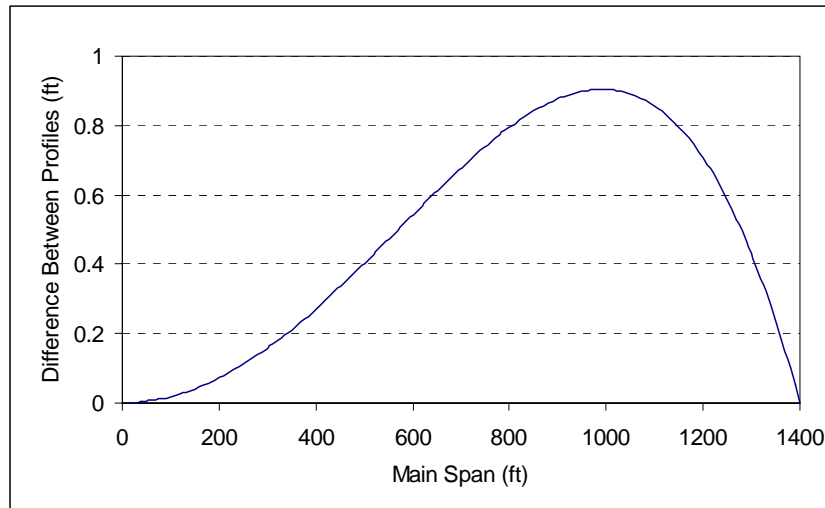


Figure 4.7: Difference between catenary profile and parabolic profile along the main span length

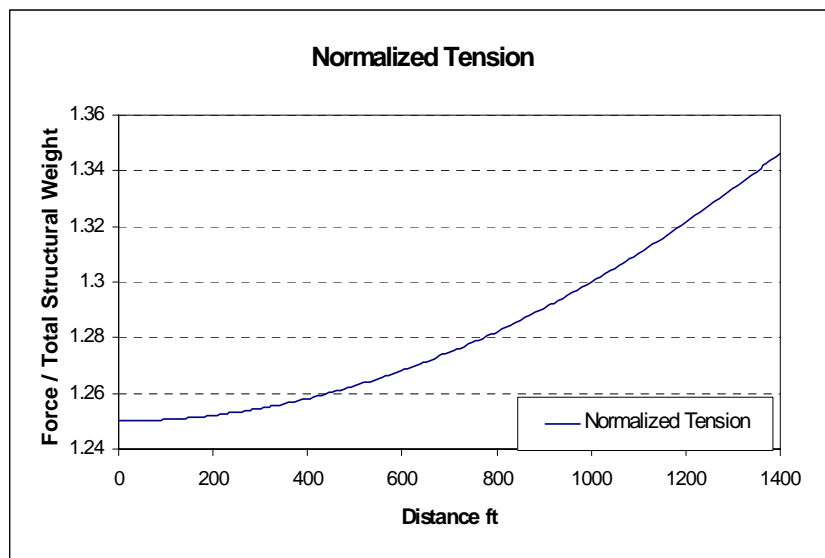


Figure 4.8: Normalized tension in main cable

While in suspension bridges, gravity loads are transferred to the main cable via discrete hangers and hence applied as concentrated load, it is assumed here that the load carried by the hanger is a uniformly distributed gravity load in order to determine the shape of the cable.

All elements are modeled based on member's centreline. Offsets can be used to model the rigid joint effects.

4.4.5 Hangers

Hanger forces are estimated by iterative finite element analysis, using detailed finite element model. Figure 4.9 shows a schematic sketch of a section along the bridge of the model used to estimate the hanger forces. The main cable is removed and the hangers are supported with hinges along the cable profile. Initially the hangers are assumed to be truss elements. A linear static analysis is conducted based on that assumption. The truss elements are then converted to cable elements and the internal forces estimated in the truss elements are then converted to cable elements and the internal forces estimated in the truss elements are used as initial forces in the cable elements.

Iterative procedure is conducted to estimate the hanger forces using the initial forces guess. Figure 4.10 shows the values and the distribution of the hanger forces. The two solid lines in the graphs represent the location of the main towers. It could be seen that the final iteration has a smoother force profile along the main span. These values are assigned to the hangers in the global detailed finite element model.

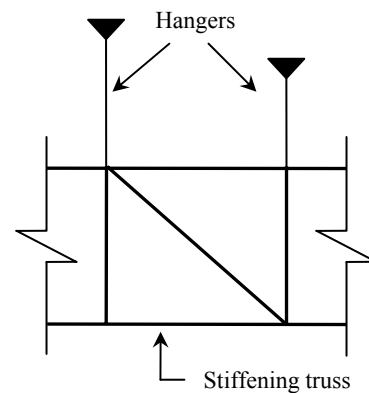
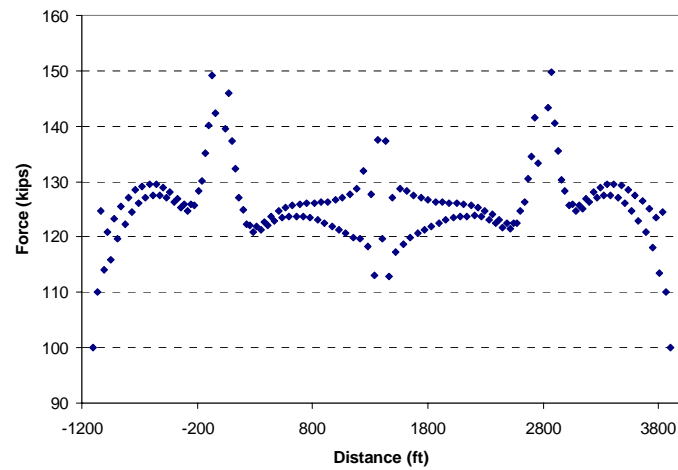


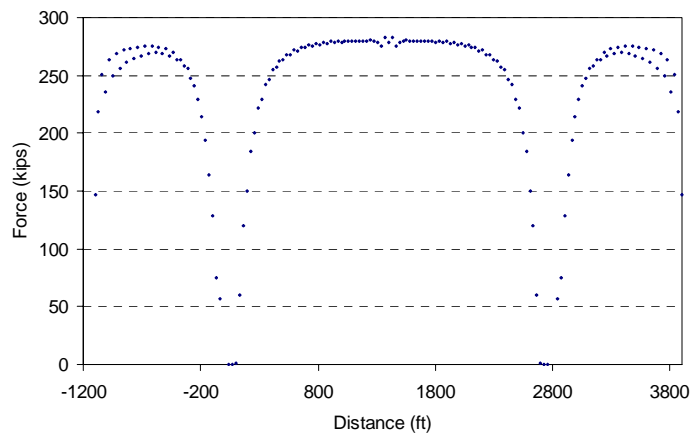
Figure 4.9: Hanger Force Model

4.4.6 Material

According to the Tacoma Narrows Bridge specifications the steel properties used are based on the ASTM A7-46, with a modulus of elasticity of 29,000 ksi for all elements.



(a) First Iteration For Hanger Force



(b) Final Hanger Force

Figure 4.10: Hanger Force

4.4.7 Section Properties

The calculations done by OPAC (1994) are adopted. The OPAC model considers spine element for the floor truss, and lump its sectional properties. This study, however, includes each floor truss element with its actual properties modeled.

4.4.8 Boundary Conditions

The boundary conditions used include the support system of the towers and the equivalent stiffness of the approaches.

The main towers are fixed on two massive caisson foundations, which are imbedded in the basin of the narrows. In the finite element model, the tower legs are assumed to be ended at the surface of the pier. A *general spring*, with six degrees of freedom, is assigned at each tower leg to simulate the soil-structure interaction. The values of the initial foundation stiffness are obtained from the study done by Geospectra, in August 1993.

The stiffness of soil-structure interaction of the Tacoma Narrows Bridge is found to be high but has insignificant effect on the frequency analysis of the bridge, if compared with fixed support condition. Analysis was conducted for the fully fixed and partially fixed conditions such that the main towers are totally constrained and then they restrained with the linear elastic springs. Six springs are assigned to each tower leg. The properties of the springs are adopted from OPAC (1994). Frequency analysis is conducted for both cases. Neither the frequencies nor the mode shapes were changed significantly. However, the modal participation factor of the first 20 models showed a change by around 8%. For

more accuracy analysis, the equivalent linear springs of the initial foundation stiffness were used.

The effect of removing the approaches is modeled as linear elastic springs. The equivalent stiffness of the west approach is added as three linear springs distributed on the top beam of tower number 3. The approach is modeled separately, such that static forces are applied to determine the equivalent stiffness values which were estimated at 226570 kips/ft and 73.2 kips/ft for the longitudinal and the transverse directions, respectively. The east tower is very short in length and made of concrete. The east approach is assumed sufficiently rigid and it is modeled as hinge support. The east approach is also excluded from the model. This will not have a significant effect on wind analysis, and will not influence the frequency content.

The two anchors, supporting the main cables and transferring their internal forces to the ground are modeled as hinges, at their corresponding locations. The anchors may experience slight movement in case of earthquakes, but their displacements are negligible if wind loading is considered.

4.4.9 Nonlinear elements

According to a field investigation, the tower top chord damper installed inside the tower were found to be leaking. These dampers are never replaced because of impracticality. It is difficult to estimate their response based on the provided

specifications in the original drawings. The AGA and OPAC (1994) study provided a force-velocity relationship for the tower damper, which is:

$$F = \begin{cases} 0.135V^2, & \text{For } V > 31.5 \text{ in/sec} \\ 135, & \text{For } 31.5 \geq V \geq 0.02 \text{ in/sec} \\ 566900 V^2, & \text{For } V < 0.02 \text{ in/sec} \end{cases} \quad 4.3$$

where F is in kips, V is the velocity of the piston in inch/second. The OPAC study utilized this relationship to establish the equivalent linearly elastic viscous damped truss element. The bottom chord dampers, installed on the tower face, have been rebuilt and are performing properly. The locations of the dampers are shown in Figure 4.4.

From the above relationship the tower dampers will not be activated until a relatively large change in the displacement along the stiffening trusses occurs. Other dampers installed in the structure are more sensitive to slower motion. Explicit modeling of these dampers is ignored here. It is assumed that the modal damping measured in the ambient study accounts for the dampers.

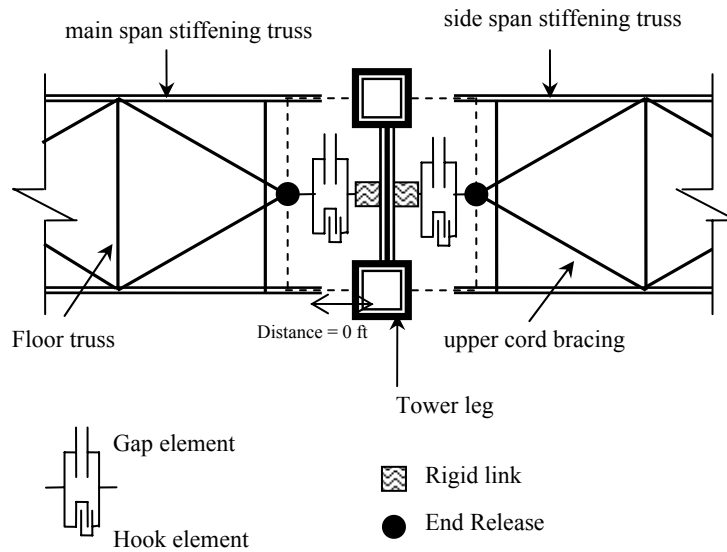


Figure 4.11: Modeling of Windshoe – top view at deck level

The nonlinear damper is modeled based on the relation shown in Equation 4.3 for $V > 31.5$ in/sec. Midas-Civil supports such a quadratic damping relationship and a small stiffness of 1 kips/ft, is assigned to the visco-elastic damper element.

The nonlinearity of the windshoe is modeled using a combination of gap and hook elements. Figure 4.11 shows a schematic top view of the joint connecting the stiffening truss and the main tower. The windshoe is connected to the bracing which ends at the mid-span of the lateral beam connecting the tower legs. There is one windshoe for each span, (i.e. two windshoes at each tower). The hook element has zero stiffness unless it is stretched a distance of 1.25 ft. When its stiffness is engaged, it will act as a rigid link due to the assigned high stiffness. The same mechanism applies for a gap element but in the other direction.

4.4.10 Load and Mass Estimation

In this stage only sustained loads are estimated. The sustained loads are due to the structural elements, such as, stiffening and floor trusses; and the non-structural elements, such as, the deck and the handrails. Traffic load and live load are ignored in the frequency analysis.

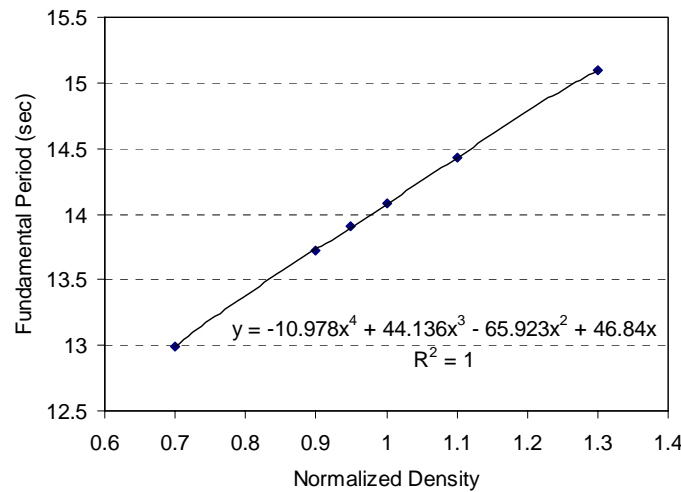


Figure 4.12: First Mode Period vs Normalized Density

Since all structural elements are included in the model and their gross cross-sectional properties are assigned, the self weight is then used to estimate the gravity load. However, the actual structural elements are not solid through out the length of the members and thus the gross area is not suitable for body force calculations. Therefore, the density assumed may need to be calibrated accordingly.

For this purpose, a parametric study is conducted to find the effect of changing the material density on the dynamic response. A steel density of, 0.49 kips/ft³ is used as a baseline. Figure 4.12 shows the change in the structural frequency due to the change in

density. While the numerical values shown in this relationship are for the first mode, other values of other modes are within 10% of these values. It could be seen that the change in the structural period is not very sensitive to the change in density. Thus the steel density is used for the gravity load and for the inertial masses computations in all degrees of freedom.

The superstructure slab, its supporting stringers and the handrails are not explicitly modeled. It is assumed that they have negligible contribution to the overall stiffness. The weight of these elements are averaged and applied as concentrated loads and masses on the joints of the upper cord of the floor truss. They are then adjusted, by trial and error procedures, to reach the measured frequencies. It was found that the load on the inner and outer joints are 12.91 kips and 10.34 kips, respectively. The gravity loads are used to calculate the equivalent concentrated masses of the deck in the three translation directions.

The average weight of the deck per span length, including the non-structural elements, is estimated to be 10.3 kips/ft. This value is estimated as follows. The detailed model is restrained by hinges at the hanger's joint, and then the reactions are calculated and averaged over the span length. This value is helpful to carry out the generalized properties of the structure.

4.4.11 Estimation of Mass

A mass is distributed based on tributary area. MIDAS-civil has the capability to lump the mass based on the section properties and the material density of each element.

Roadway slab mass is lumped at each node based on a tributary area. Translational mass and rotational mass in the three directions are both considered in the analysis.

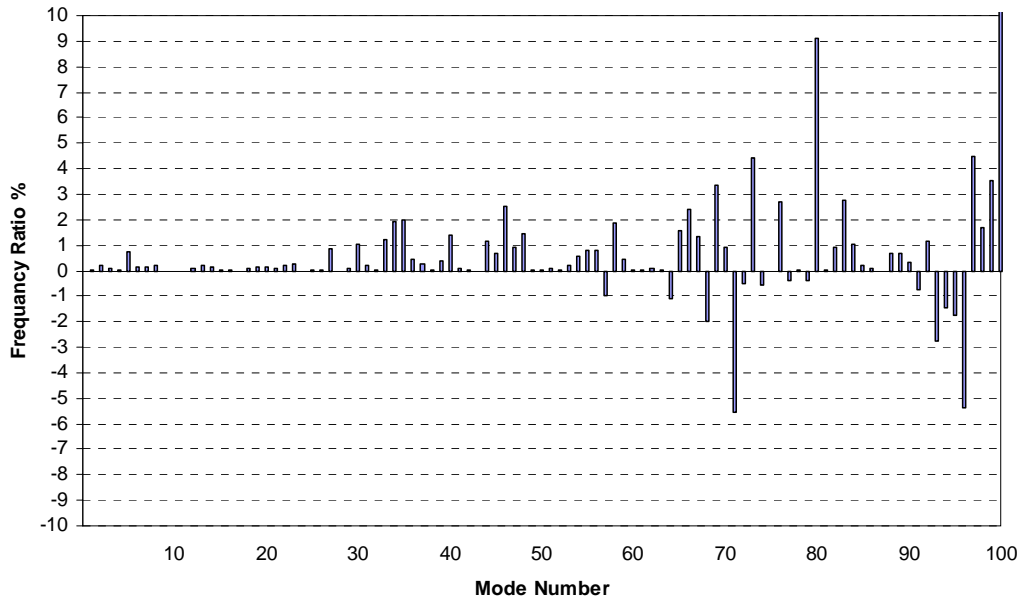


Figure 4.13: Effect of Eliminating Tower Contribution to Frequency Content

A parametric study is conducted to evaluate the effect of modeling the tower on the frequency content. The tower mass is calculated based on the assigned density and the cross sectional area. The density of the tower is set at zero to eliminate its effect on the frequency content. Figure 4.13 shows the percentage difference between the frequency of the bridge with and without the tower contributions. It could be shown that the tower effect is less than 1%, up to the 30th mode. The effect of the tower on the modal analysis is critical after the 100th mode, where the model analysis is cut off. Moreover, it is found

from the modal analysis that the frequencies related to the superstructure oscillation are found between the first and the fiftieth modes.

The parametric study verifies that uncertainty in the tower modeling is not of concern for wind analysis of the bridge superstructure. It is evident that the frequencies governing the tower vibration are beyond those of the superstructure.

The finite element model is used to estimate the uniformly distributed weight over the span length of the deck such that the reactions of the hangers are summed and distributed over the span length. The uniformly distributed load over the span length is estimated to be around 8433.7 lb/ft (255.8 slug/ft), which is equivalent to a uniformly distributed mass of 12,451.5 kg/m.

4.5 Frequency Analysis

4.5.1 Ambient Study

Ambient vibration measurements were taken by the Johns Hopkins University under the supervision of Dr. Nicholas Jones in 1993. The mode shapes and the damping ratios of the bridge are derived from the data generated. The ambient study comprised both transient vibration and ambient vibration measurements. The *transient measurements* are the vibrations recorded after a sudden release of energy, such as impacting the structure with a large load. This approach is used to estimate the frequency of the superstructure. *Ambient measurements* are the vibrations produced by traffic and wind. This approach is useful to estimate both the deck and the towers frequencies. For best transient

measurement analysis, the records should be taken when the ambient vibrations are minimal.

The transient measurements captured the first mode of vibration, 0.074 Hz. The second mode was not captured. The third mode, predominantly vertical mode; the fourth mode, center-span lateral mode; the fifth mode, center-span vertical and the sixth mode, center-span lateral mode, are also captured by the transient analysis. The ambient measurements revealed the first 9 vertical, 1 torsional and 12 lateral natural frequencies.

The damping ratio was determined to be in the range of 0.3% to 3.5% and the study concluded that the average damping is 1.3%, which is a reasonable number and close to the true value for the size of the Tacoma Narrows Bridge when operating within the elastic range. The results of the natural frequency are shown with the frequency analysis results are presented below. The average damping ratio of the bridge is relatively small in magnitude. Therefore its influence on the damped natural frequency is insignificant and could be considered equal to the undamped natural frequency.

4.5.2 Eigenvalue Analysis

In the analysis, 100 Ritz vectors are generated, that is, one hundred modes and frequencies are estimated. The mode shapes and frequencies obtained from the analysis are found to compare reasonably well with experimental studies as shown in Table 4.1.

4.5.3 Model Calibration and Analysis

The following procedure was used to calibrate the model:

1. Pre-modelling Phase:
 - a. Evaluation of the bridge detailed drawings.
 - b. Review previous studies on the bridge.
 - c. Develop a 3-D CAD model for the bridge geometry.
2. Structural Modelling Phase:
 - d. Transfer the CAD model to the structural analysis program (MIDAS-Civil).
 - e. Calculate gross cross sectional properties.
 - f. Compute the weights of non-structural elements.
 - g. Estimate boundary condition of foundations and the approaches.
 - h. Approximate the initial tension in the main cable and hangers, using the elastic theory.
 - i. Iterate the cable forces.
 - j. Solve Eigen value problem, using the Ritz theory method.
3. Model Calibration
 - k. Calibrate the estimated sustained loads and re-evaluate the cable initial tension.
 - l. Calibrate boundary condition.
 - m. Calibrate selfweight, by tuning the material density.
 - n. Evaluate the modal response and reiterate, as needed.

4.6 Results

Table 4.1 lists the bridge frequencies. Experimental frequencies are obtained from the ambient vibration taken by the Johns Hopkins University in September, 1993. The analytical results are estimated using MIDAS-civil. Ritz vector is used in the Eigenvalue analysis. The table shows the results of the OPAC (1994) study. The error percentage shown is the analytical results, obtained in this research, to the corresponding experimental frequency.

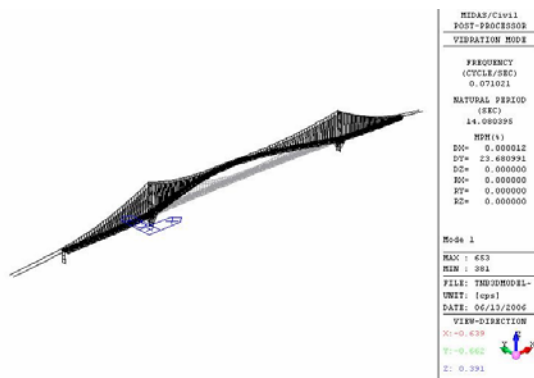
Table 4.2 shows thirteen modes of vibration for the Tacoma Narrows Bridge. The identified modes are only those vertical, transverse and torsional modes of vibration. Appendix A shows complete identification of the bridge mode shapes and their locations. Periods after the 50th mode are found to be relatively very small, less than 1.5 second, for wind analysis.

Table 4.1: Comparison between the experimental and the analytical frequencies

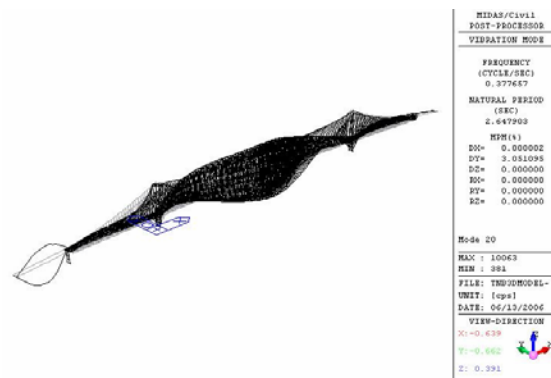
Longitudinal Modes					
Location	Field Freq. Hz	OPAC-1994 Hz	Analytical Results		
			Value - Hz	Error	Mode Number
Center Span	0.187	0.186	0.1565	-20%	3
	.262	0.232	0.2071	-26%	5
Transverse Modes					
Location	Field Freq. Hz	OPAC-1994 Hz	Analytical Results		
			Value - Hz	Error	Mode Number
Center Span	0.074	0.067	0. 07102	-4%	1
	0.33	0.314	0. 3401	+3%	18
	0.358	0.339	0. 3481	-3%	19
	0.386	0.364	0. 3962	+3%	21
	0.496	0.477	0.4824	-3%	29
Vertical Modes					
Location	Field Freq. Hz	OPAC-1994 Hz	Analytical Results		
			Value - Hz	Error	Mode Number
Side Span	0.162	0.143	0. 1565	-5%	3
	0.25	0.232	0.2490	-1%	7
	0.30	0.252	0.3248	+8%	15
	0.362	0.317	0. 4012	+10%	25
Center Span	0.162	0.143	0. 1565	-4%	3
	0.30	0.252	0. 3248	+8%	14

Table 4.2: Modal Frequency Identification of the TNB

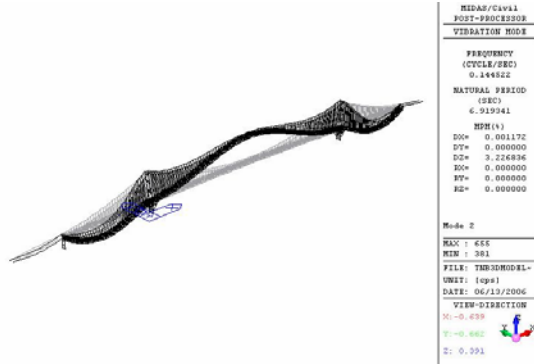
	Mode	Frequency (rad/sec)	Frequency (Hz)	Shape	Location	Symbol Key	
1	1	0.446236	0.0710206	L_HS	MS	L	Lateral Mode
2	2	0.908061	0.1445223	V_HS	MS	V	Vertical Mode
3	3	0.983197	0.1564806	V_FS	MS	T	Torsional Mode
4	4	1.167195	0.1857648	L_FS	MS	HS	Half Sinusoidal
5	7	1.564752	0.2490380	V_(FS+HS)	MS	FS	Full Sinusoidal
6	15	2.04103	0.3248400	V_2HS	MS+SS	MS	Mid Span
7	19	2.186997	0.3480713	L_FS	C+S	SS	Side Span
8	20	2.372891	0.3776573	T_HS	S	SC	Side Span Cable
9	21	2.489505	0.3962170	(L+T)_(FS+HS)	S	MC	Mid Span Cable
10	22	2.520852	0.4012060	V_2FS	MS	TW	Tower
11	36	3.604311	0.5736439	V_(2FS+HS)	MS	C	All Cables
12	37	3.721043	0.5922223	(L+T)_FS	MS	S	All Span
13	41	3.928639	0.6252623	T_FS	MS		



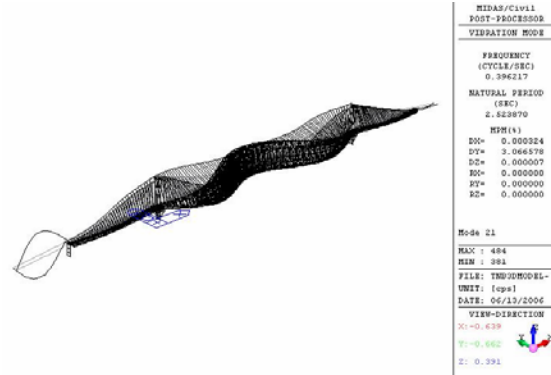
Mode 1: Lateral



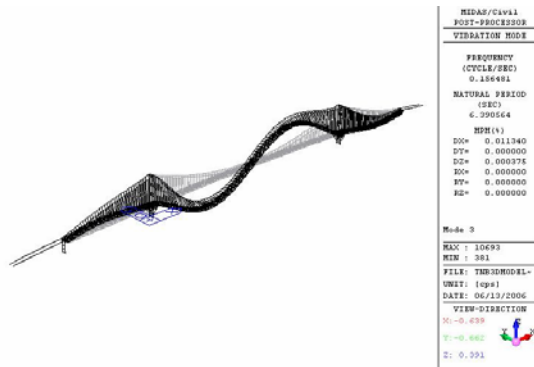
Mode 20: Torsional



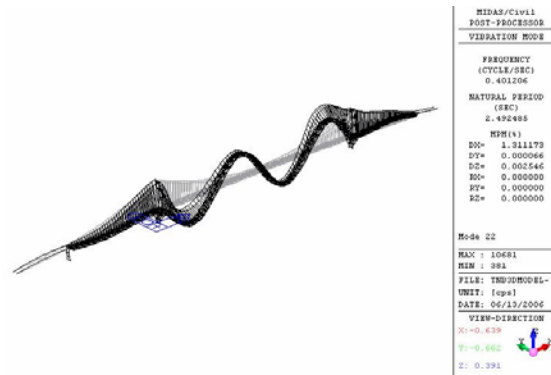
Mode 2: Vertical



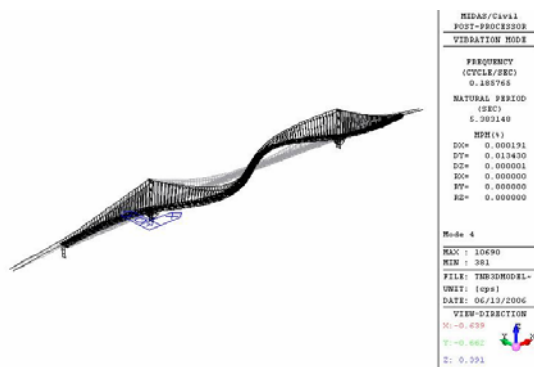
Mode 21: Lateral-Torsional



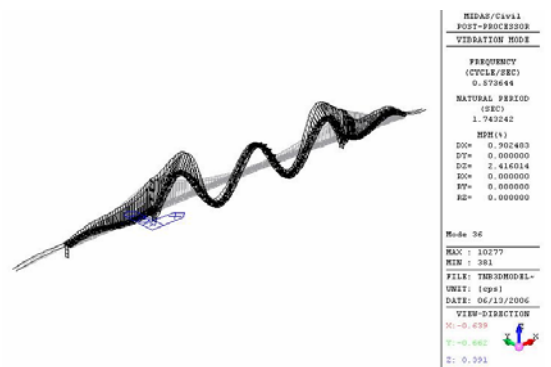
Mode 3: Vertical



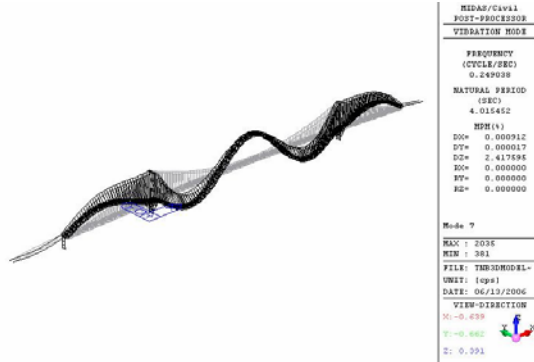
Mode 22: Vertical



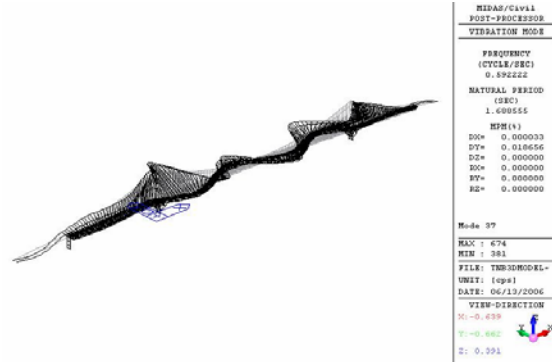
Mode 4: Lateral



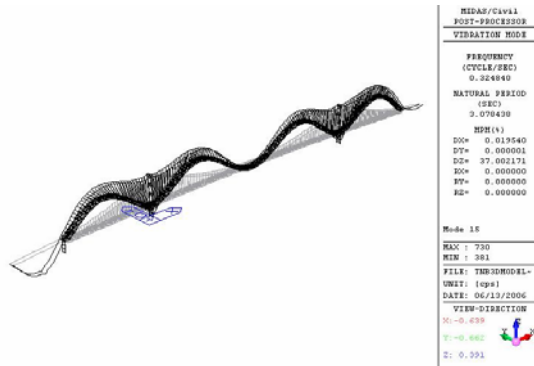
Mode 36: Vertical



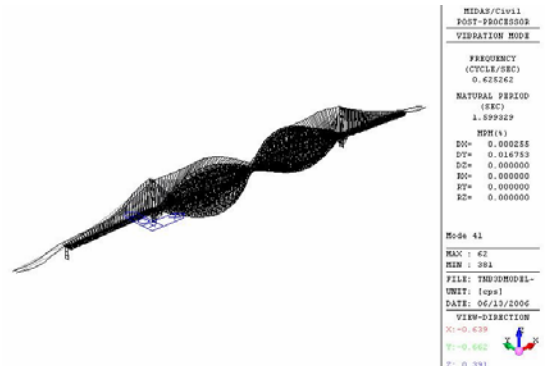
Mode 7: Vertical



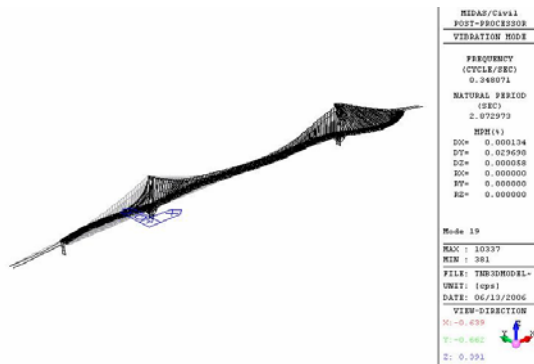
Mode 37: Lateral-Torsional



Mode 15: Vertical



Mode 41: Torsional



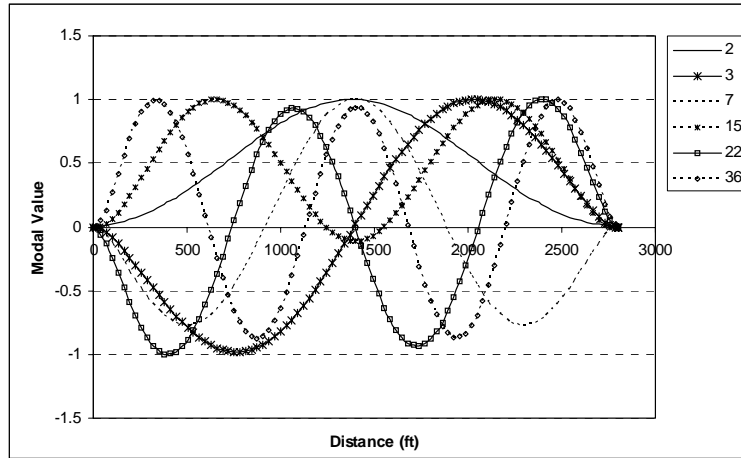
Mode 19: Lateral

Figure 4.14: Mode shapes of Identified Modes

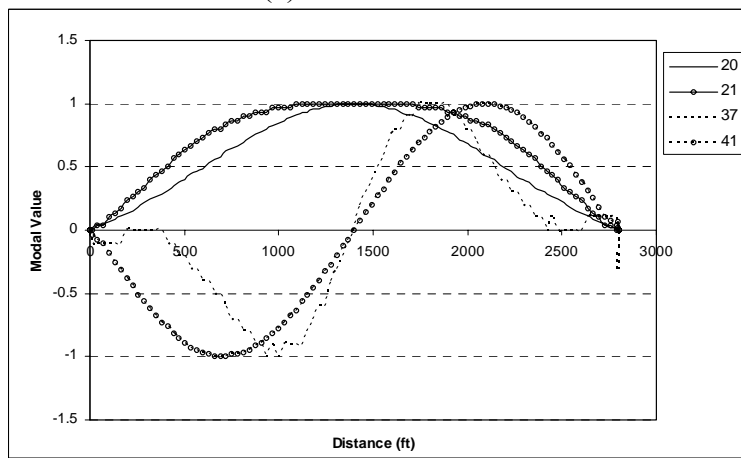
The coupling coefficients are shown in Table 4.3. The underlined modes are those with high coupling potential.

Table 4.3: Coupling Coefficients of the Tacoma Narrows Bridge					
Set No	Mode i	Mode j	C_i	C_j	C_iC_j
1	2	20	1.075	0.9167	<u>0.985453</u>
2	2	21	1.2257	0.7599	<u>0.931409</u>
3	2	37	0.258	0.2876	0.074201
4	2	41	0.0304	0.0266	0.000809
5	3	20	0.3222	0.3489	0.112416
6	3	21	0.438	0.3448	0.151022
7	3	37	0.7335	1.0383	0.761593
8	3	41	0.0595	0.0661	0.003933
9	7	20	0.2551	0.2108	0.053775
10	7	21	0.1126	0.0676	0.007612
11	7	37	0.0522	0.0564	0.002944
12	7	41	0.0836	0.0709	0.005927
13	15	20	0.6886	0.6078	0.418531
14	15	21	0.937	0.6013	0.563418
15	15	37	0.2921	0.337	0.098438
16	15	41	0.0125	0.0113	0.000141
17	22	37	0.4059	0.5636	0.228765
18	22	41	0.4325	0.4716	0.203967
19	36	37	0.0978	0.1274	0.01246
20	36	41	0.9684	0.9911	<u>0.959781</u>

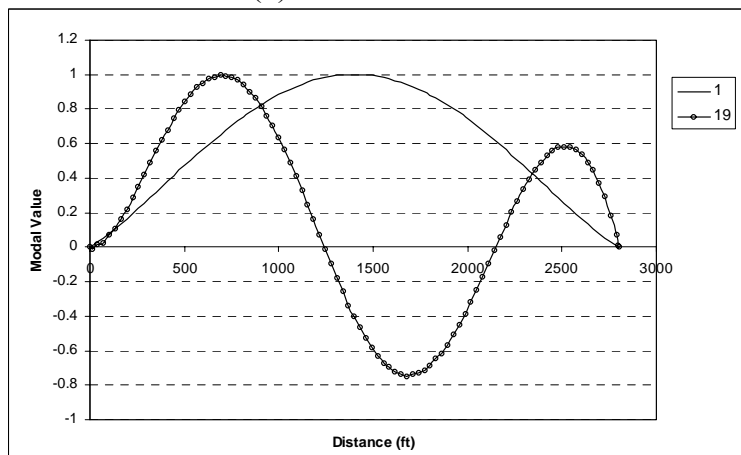
It is expected according to the coupling coefficients, that the critical condition might be due to the coupling between the second and the eighth mode, the second and the ninth modes or the eleventh and the thirteenth modes. This conclusion is supported by the flutter analysis conducted on the bridge, in Chapter 6, using the suggested coupling patterns above.



(a) Vertical modes



(b) Torsional modes



(c) Lateral modes

Figure 4.15: Normalized modes of vibration

All the shown modes of vibration are symmetric about the span centerline, except, the second lateral mode of vibration (mode 19). This mode is coupled with the longitudinal

mode which transports the effect of the asymmetric boundary condition to the lateral mode. It could be noted that the curve amplitude attenuates from left to right and the curve matches with the point of symmetry at the centreline of the mid-span. This is due to the effect of the eastern boundary condition (at the right-hand-side side-span), which is stiffer than the boundary condition at the other end of the western side-span.

4.7 Discussion

Table 4.1 shows the frequencies obtained from the ambient analysis, OPAC (1994) study and this research. Note that the frequencies evaluated using the proposed methodology are relatively accurate when compared with the experimental results. The error in the transverse and the vertical modes is not more than 10%. This error is very acceptable. However, the frequencies of the longitudinal direction are less accurate.

Unlike the superstructure transverse and the vertical modes of vibration, the longitudinal mode of vibration of the deck interacts with the tower and the approaches boundary conditions. In other words, the modeling of these two components reflects on the accuracy of the superstructure frequencies in that direction. A 26% error in the frequency is not faulty results for the following reasons. The tower and the approaches, most likely, will not interact with the deck movement, because the windshoe and the expansion joints provide enough separation. Moreover, the longitudinal mode shapes are not significant in wind. The deck is assumed to be sufficiently rigid along its axis and only excitations in the transverse, vertical and rotational are considered. The frequencies in this direction shall be further calibrated if seismic analysis is required.

The results obtained here are more accurate than those of the OPAC (1994) study. Note that most of the section properties, boundary conditions and mass estimations used in this research are based on the OPAC study. The study, however, used linear cable element instead of catenary cable element. This proves that using catenary cable element with appropriate initial tension estimation is essential for accurate frequency analysis.

There are several factors that affect the frequencies of the structure. The most important factors include mass estimation and distribution, element stiffness and initial tension in the cables. Boundary conditions and soil structure interaction are of less significance. The towers have small influence on the low structural frequencies, and their effects are significant only after the 50th mode. Thus, the superstructure and cable properties have the most impact in the lower frequency range.

CHAPTER 5

BRIDGE AEROELASTICITY

5.1 Background

The failure of the Original Tacoma Narrows Bridge was a pivot point in the history of suspension bridges, as it coincided with the evolution of aeronautical engineering. Thus the failure was justified, unlike prior bridge catastrophes. Vortex-induced and flutter forces become well-recognized as the main phenomena responsible for long-span bridge collapse.

Classical aerodynamic theories of wind forces are based on steady-state expressions such as Bernoulli's equation, and solved using the quasi-static approach. However, this type of formulation is insufficient to describe the rapid time-varying forces that develop at higher speeds. Moreover, steady-state functions will not allow expressing the self-induced forces, resulting from the change in deformations or deflections due to time. Therefore, it was necessary to develop more general theories to account for time variation. Theories that followed the quasi-static approach were based on transient dynamic analysis. Earlier tests started on airfoil in laminar wind flow followed by studies of bluff bodies.

5.2 Earlier Aeroelasticity Theories

The first insightful view into self-induced forces was investigated by Wagner (1925), using thin aerofoil with various angles of attack. He proposed a very illustrative indicial function to express lift force for thin airfoil undergoing a step change in the angle of

attack in incompressible flow. Theodorsen (1934) presented his function which was later considered as a fundamental function in unsteady aerodynamics on oscillating thin airfoil in incompressible flow. The function is described in complex terms with respect to time-frequency domain. The function is considered as a reference in developing flutter formulation for a bluff body, as described by Scanlan and Tomko (1971). Kussner (1936) then presented the theoretical bases of flutter forces and gust penetration for a thin airfoil. Garrick (1938) investigated the foregoing theories and found the relations among them using Fourier transformation. He thus proved the interrelation among all of these theories of non-stationary flows. Sears (1941) proposed an admittance function named after him which is now a well-known function in the frequency domain analysis. In 1941, Von Karman and Sears investigated flutter of a thin airfoil moving into a sinusoidal vertical velocity (gust) field. Sears problem shows the fundamental difference between the results obtained on an oscillating airfoil in angle of attack and an airfoil moving through an oscillating vertical velocity field, where the latter results in a non-uniform angle of attack over the airfoil chord. The Sear's function is formulated in the frequency domain, similar to the Theodorsen function (1934).

The Theodorsen Function is applicable in many cases of both fixed-wing and rotating-wing aerodynamics. However, they are less capable in other problems where time is an important parameter where the velocity of the elastic body is not usually constant. Thus, the reduced frequency term ($K=UB/\omega$) becomes very ambiguous in this case, where U is the oncoming wind velocity, B is the characteristic geometric parameter (usually the width of the elastic body) and ω is the circular frequency of motion. Theories

formulated in time-domain are more general as they account for the varying or arbitrary velocity of the solid body in the flow. However, as mentioned before, Wagner (1925) obtained a solution for the indicial lift on a thin-airfoil undergoing a step change in the angle of attack in incompressible flow. He introduced terms that represent the flow taking into account the effect of time-history change of the angle of attack on the lift.

Sisto published a paper on stall flutter of airfoil while Liepmann (1952) applied the forgoing theories in conjunction with statistical concepts to outline the random buffeting problem of aircraft lifting surfaces, considering the Sears admittance function in that process.

5.3 Early Bridge Aeroelasticity Theories

After the collapse of the Tacoma Narrows bridge in 1940, a board of engineers consisting of O.H. Ammann, T. Von Karman and G.B. Woodruff issued a detailed report concerning the catastrophic failure. The report included a paper by Louis G. Dunn explaining the phenomenon of vortex-shedding with the equation of motion, and giving a detailed account of some of the earliest deck sections that collapsed, in particular those that have negative aerodynamic damping and torsional flutter.

The explanation by Dunn was followed by an analysis of bridge flutter. Bleich (1948) and Bleich (1949) used the Theodersen theory for flat plate for the analysis of bridge flutter. The results, however, were not applicable to unstreamlined bridge decks. The reason is that the Theodersen function was derived for thin flat plates. An alternative

approach, originally recommended by Dunn in the Tacoma Narrows Bridge case, emerged suggesting that if motional force coefficients (flutter derivatives) are obtained experimentally, they might be useful in the analysis. This idea was widely adopted and used in the investigation. It became the fundamental idea in the theory of bridge aeroelasticity. Davenport (1962) adopted steady-flow formulation following Liepmann's approach and the Sears admittance function to analyze bridge buffeting.

The theory of bridge aeroelasticity was established late in the 60's with most of the effort undertaken in the US and Japan. In the US, most of the research was attributed to Scanlan, who outlined the flutter theory based on measured motional aerodynamic derivatives. Scanlan's contribution in aeroelasticity started in 1951 by investigating aircraft vibration and flutter. In 1967, Scanlan and Sabzevari presented a conference paper revisiting the analysis of bridge flutter based on experimental flutter derivatives. Meanwhile, Ukeguchi, Sakata and Nishitani released a study on bridge flutter based on the experimentally measured flutter derivatives theory, proposed by Scanlan and Rosenbaum. Another contribution was made by Tanaka and Ito (1969) on the characteristics of the aerodynamic forces of self-excited oscillations of bluff structures.

The concept proposed by Bleich (1948) to use the flat plate theory in bridge aeroelasticity was revisited in 1971. Flutter derivatives of streamlined bodies were experimentally investigated and compared to the theoretical flutter derivatives of airfoils, so that the former will be applied to bridges. Sakata (1971) found that the thin airfoil flutter theory was reasonable to apply on streamlined bridge deck sections. He

recommended his findings to the design of the Severn Bridge, which was the first ever to be constructed with thin streamlined deck. However, Scanlan and Tomko (1971) tested sets of flutter derivatives for bridges and compared them to the airfoil derivatives. They concluded that bridge flutter derivatives are significantly different from airfoil derivatives. Accordingly flutter derivatives of bridges are not accurately expressed by analytical or mathematical solutions and experimental data is needed to characterize them.

Another research approach was pursued to solve the equation of motion in conjunction with the self-excited forces. The need to link the frequency domain with the time domain was realized by Scanlan and Budlong (1972), where the Fourier transformation was used to link the bridge deck flutter derivative and the distinct aerodynamic force functions that were functions of both time and frequency. Thus the right-hand-side of the equation of motion of self-induced forces became a function of the frequency and the response.

Flutter is one of the oscillation regimes of solid bodies in wind. It accounts for one component of instability, where wind is assumed to be laminar. Buffeting, is another component that might contribute to the stability of a solid body in wind. There are other different aeroelastic phenomena such as vortex-induced motion, that are explained below.

5.4 Wind Forces on Bridges

Modern aeroelasticity classifies wind forces on solid bodies into a number of models each having a different mathematical model. This is based on the type of the interaction that occurs between wind and a solid body. Some of the theories are recognized from early theories conducted on flat plates and airfoils and applied to bluff-bodies. Aeroelastic phenomena are vortex-shedding, cross-wind galloping, wake galloping, torsional divergence, flutter and buffeting.

Modern long-span bridges wind response is basically due to three main components, namely, Flutter, buffeting, and vortex shedding components. y. The flutter component which is the most substantial instability component is described with respect to the average laminar wind speed while the buffeting component stochastically estimates the variable wind speed on the deck motion. The vortex shedding component is the least potentially destructive instability component .

The other aeroelastic instability phenomena, across-wind galloping and wake galloping, are of less importance on the global response of bridges and more related to cables and hangers oscillation. Cross-wind galloping takes place when the main cable has received a coating of ice under conditions of freezing rain. Wake galloping occurs when a bluff body is located in the wake of another bluff



Figure 5.1: Grouping of Hangers

body. This occurs when a bundle of hangers is grouped in four cables as shown in Figure 5.1. As the length of the hanger increases its frequency becomes very small and it

becomes vulnerable to wind. Those hangers in the windward are susceptible to vortex-induced motion and will shed a wake that extends to the leeward hangers, which become susceptible to wake galloping.

This phenomenon might also be of interest in the case of two bridge decks being closely separated and located nearly at the same level. The wake of the upstream deck might induce violent oscillation in the downstream one. A New Tacoma Narrows Bridge is currently under construction next to the existing one. A wind tunnel experiment is done by Rowan Williams Davies & Irwin Inc. (2003) to check the galloping effect. The report concluded the safety of both bridges. The following is a summary of the most important three aeroelasticity phenomena vortex-shedding, self-induced vibration, and buffeting.

5.4.1 Vortex-shedding

The very first observation on flow-structure-interaction was published by Vincenz Strouhal in 1878. Strouhal observed that there is a relation between the natural frequency of an Aeolian wire and its vibration frequency induced by wind flow. He concluded that the sound of the wire would be substantially magnified when the frequency of the vibration approaches the natural frequency of the wire. Strouhal came up with a non-dimensional quantity, known as Strouhal Number (S) that concludes the regularity of vortex-shedding phenomena of a bluff body.

$$S = \frac{N_s D}{U} \quad 5.1$$

Where N_s is the frequency of a full vortex shedding cycle, that is, the shedding frequency, D is the characteristic dimension of the body projected on a plane normal to the laminar oncoming flow velocity, U . Strouhal Number is constant for certain-cross sectional shapes.

Wake behavior in certain Reynolds number range is found to be remarkably regular. Benard, in 1908, and Theodore Von Karman, in 1911, reported the behavior of vortex shedding behavior of flow around a two-dimensional cylinder. They investigated the separation of the flow around the cylinder and noticed alternating vortices shed from the cylinder and form a clear recurring “vortex trail” downstream. The fine details behind this phenomenon were not quite investigated and many theoretical and experimental studies were conducted to find an explanation.

Abstractly, *vortex-shedding* is a phenomenon that takes place subsequent to the separation of the boundary layer as a result of the interaction between oncoming fluid flow and a bluff body. Depending on the bluff body’s shape at certain Reynolds number, the boundary layer might experience unsteady separation that leads to a repeating pattern of eddies, called the Von Karman vortex trail.

For a certain shape, the mechanism of vortices is function of Reynolds number. For example the flow around a cylinder looks symmetric and with no separation in the boundary layer at $Re \approx 1$. Separation is initiated at $Re \approx 20$, where two symmetric eddies start forming next to the solid body and extend downstream. Up to this limit, drag force is

mainly generated due to the viscosity of the fluid and the skin friction of the solid body. Pressure around the solid body is symmetric, and hence the lift force is negligible. The two eddies grow the Reynolds number increases, $Re \approx 30$ to 5000 , and the flow starts shedding a staggered, well-defined, alternating arrangement of vortices that travel downstream at a velocity fairly less than that of the surrounding fluid. Transition to turbulence in the wake and large separation in the shear boundary layer downstream occur as the Reynolds number increases, $Re \approx 5,000$ to $200,000$. In this range three dimensional patterns start forming and transition to turbulent flow occurs in the wake as the Reynolds number decreases along the wake from that closer to the cylinder surface to that downstream, and the clear vortex-shedding disappears. In high Reynolds number flow, $Re > 200,000$, the wake narrows substantially resulting in considerable reduction in the drag. Analogous vortex-shedding behaviors are also observed for other types of bluff bodies, such as, triangles, squares, prisms and I- and H-shape sections.

When vortex shedding takes place the positive/negative pressure distribution around the body alternates with time. This creates oscillatory motion across the flow. The frequency of the shedding, N_s as shown in Equation 5.1, determines the frequency of the solid body oscillation. If the shedding frequency matches the natural frequency of the body resonance takes place. The dynamic system is only a function of the across flow degree of freedom. If other degrees of freedom are included in the system, flutter will take place. Distinction between vortex-shedding motion and flutter will be discussed in the self-induced forces section. For a high Reynolds number, the Strouhal number could

be averaged and considered to be constant for a specific shape. It is found that for cylinders Strouhal number is 0.2 and for an I-beam it is around 0.12.

Experimental tests for different bluff bodies showed that at a certain range of Reynolds number depending on the tested shape the frequency of shedding remains unchanged and equal to the natural frequency of the structure. This is known as the *Lock-in phenomena*, where the stored energy equals the damped energy, and thus excessive response is manifested.

Vortex shedding vibration could be ignored in most of the current long-span instability problems. Vortex-shedding induced vibration is significant when the deck section has blunt shape and has relatively low structural frequency. However, some earlier bridges such as the Original Tacoma Narrows Bridge were very susceptible to vortex-induced forces as they have a very slender low frequency H-shape deck.

Vortex shedding force is important to be checked for the local instability of individual elements, such as beam, truss or cable elements. Generally, vortex-induced forces of individual elements, such as the I-beam, T-beam and L-beam, add significant change to the stored energy in the whole structure which may turn the load estimate by building codes to be less conservative, Grant and Barnes (1981). Hangers and cables are the most susceptible structural elements for vortex-induced forces. Hangers located in the wake of other hangers will be more vulnerable to high vibration amplitudes. This depends on the angle of attack of the wind and the spacing between the hangers, Cigada et. al. (1997). In

the Second Tacoma Narrows bridges clasps were used to brace the hangers against vortex-shedding vibration.

In summary, vortex-induced forces are, most probably, not the critical component in bridge global response, but it onsets motion or vibration that might lead to another type of aeroelastic instability, which is flutter (self induced forces).

5.4.2 Self-induced Forces

For a cross-wind single degree-of-freedom bluff body system, vortex-induced motion is most likely to occur. In a multi-degree of freedom system, however, vortex-shedding might induce the first across wind mode. The structure



Figure 5.2: Torsional Oscillation of the First Tacoma Narrows Bridge.

might switch to a higher mode of vibration depending on the amount of energy stored in the system and the structural frequencies. A good example of that is the First Tacoma Narrows Bridge, as mentioned before. Vortex shedding initially induced vertical motion. At wind speed 42 mph the bridge switched from pure vertical oscillation to pure torsional vibration. Assuming that the Strouhal number for the First Tacoma Narrows Bridge is 0.12, based on I-beam shape experiments, (see *“Wind Forces on Structures,” Trans. ASCE, 126 (1961)*), the wind speed at collapse is 62 ft/sec and the girder depth is 8 ft, then the shedding frequency, based on Equation 5.1 will be around 0.9 Hz. The frequency of the destructive mode, 0.2 Hz, was neither a natural mode of the isolated structure nor the frequency of bluff-body vortex shedding of the bridge at that wind speed. The

justification lays in understanding flutter, where the aerodynamic forces and the excited structural frequency are mutually developing to an extent where instability takes place at a combination of modes of vibration.

Flutter is classified into different categories. *Classical flutter* is originally recognized in aerospace applications and applied to thin airfoils, and later applied to long-span bridges. It indicates an aeroelastic phenomenon in which two degrees of freedom of a structure, mainly torsional and vertical translation, couple in a flow-driven, unstable condition. The coupling of modes is the characteristic sign of the classical flutter. Other types of flutter are *stall flutter* or *single-degree-of-freedom flutter*, where oscillation of the solid part is driven by nonlinear characteristics of lift or torsional forces, such as, sudden loss of lift. In the structural sense, flutter is analogous to buckling, where a small magnitude of perturbation could be sufficient to be the incipient of the critical mode. The analytical models developed to solve the flutter problem assume oncoming wind in a steady-state condition.

5.4.3 Buffeting

Buffeting force is the aeroelastic component that accounts for the unsteady wind component to the instability of slender structures in wind. The fundamental ideas to estimate buffeting of line-like structures by atmospheric turbulence are set up by Liepmann (1952) and Davenport (1961). Most of the theories are developed based on statistical models to synthesize a random periodic function which simulates the

fluctuating wind component. Several assumptions and simplifications are used to simplify the buffeting analysis of line-like structures. These assumptions are:

- a) The oscillations of the structure in each responding mode are very small and, i.e., aerodynamic behavior of the structure is linear; b) The squares and products of the velocity fluctuations are negligible with respect to the square of the mean velocity and
- c) The static force coefficients are independent from the frequency in the range considered. Thus it is assumed that the buffeting force is based on a quasi-steady theory and is not function of frequency as the case with the flutter force. This inconsistency requires superimposing the buffeting forces and the self-excited forces simultaneously assuming harmonic response of the structure to give the total aerodynamic force.

Buffeting response of suspension bridges is not discussed in this research and only flutter analysis is considered. This does not necessarily imply that the critical response is underestimated or that the critical wind speed is overestimated. In fact tests done on an I-beam, a cylinder and a square sections show that increasing the turbulence intensity of the oncoming wind diminishes the amplitude of oscillation of the bluff-bodies at a given average wind velocity, Barriga-Rivera (1973).

Diana et al (1993) concluded, based on quasi-static analysis, that for a box shape deck the effect of turbulence is correlated to the degree of nonlinearity of the wind derivative, where a sudden divergence in the angle of attack due to flutter instability, might cause change in the response due to high degree of wind turbulence intensities. In some cases the turbulence of wind, when considering the sign couple derivatives, reduces the

effective torsional stiffness of the bridge deck, causing excessive rotational displacement at flutter. It does however damp out the torsional acceleration response. Diana et al (1993) also concluded that in the case of low turbulence flutter velocity does not change. In case of strong turbulence with more than 0.2 turbulence intensity, it is difficult to settle the flutter velocity because oscillation amplitudes are already high because of large wind force.

5.5 Analytical Models of Flutter

Motion-induced, or *self-excited*, forces play an important role in the design of suspension bridges. When wind velocity reaches a speed at which the input energy from the self-induced motion is equal to the dissipated energy by mechanical damping, *flutter* occurs and the wind speed is called *critical flutter wind velocity*.

Flutter analysis could be accomplished using experimental and/or analytical techniques. Wind tunnel is the standard experimental method where a prototype resembling the whole structure is modeled and tested. Analytical methods are derived based on time and frequency domains. The frequency domain method is adopted by most researches since it requires less computational effort than the time domain analysis method. Thus it became the attractive traditional method in the absence of efficient computer resources, Scanlan (1988). To provide reduced computational efforts, researchers used to consider *multi-mode* analysis instead of *full-mode* analysis, also known as the *direct method*. In the multi-mode analysis modal superposition is employed to sum up the effect of dynamic properties and represent coupling between frequencies.

Full-mode analysis requires explicit representation of all the degrees-of-freedom required along the structure, and then solving the equation of motion to find the critical flutter condition.

Several modes of vibration are involved in suspension bridges. Coupling of two modes namely the vertical and the torsional modes usually takes place when the structure starts to reach its critical vibration frequency. Multi-mode behavior, with more than two degrees-of-freedom, becomes more significant with the increased center-span length. Multi-mode flutter is likely to occur when the location of the maximum deflections of two modes coincide with each other. Most of the studies suggest coupling of the vertical and the torsion modes of vibration.

Ge and Tanaka (2000) proposed a study that investigates these issues and provides a numerical approach for multi-mode and full-mode aerodynamic flutter analysis. There are two issues associated with the multi-mode frequency domain analysis where the assumption includes dynamic coupling between natural modes and the self-excited aerodynamic forces. The first issue involves the number and kind of natural modes participating in the instability of the structure. The second issue involves the mode combination which is only an approximate expression of flutter and thus the result of the modal superposition will not necessarily be always accurate. Still the results of both types of analysis are sufficiently close considering the accuracy required in engineering

applications. Multi-mode analysis is adopted in the research. The following is a discussion for the solution process.

5.5.1 Equation of Motion

The equation of motion of a bridge with a two-degree-of-freedom section could be written as follows:

$$m\ddot{h} + c_h\dot{h} + k_h h = L_{ae} \quad 5.2-a$$

$$I\ddot{\alpha} + c_\alpha\dot{\alpha} + k_\alpha \alpha = M_{ae} \quad 5.2-b$$

where: m is the mass per unit length, I is the mass moment of inertia per unit length, c_α and c_h are the coefficients of viscous damping, h and α are the vertical and the rotational displacements, as shown in Figure 5.3, and L_{ae} and M_{ae} are the self-excited aerodynamic lift and Moment forces about the rotational axis per unit span, respectively.

The above equation requires that the center of mass be located in the vertical plane of the center of rotation. This is typical in suspension bridges where the deck is symmetric about its vertical axis. It is, however, not necessary that the two centers match along the vertical axis. The above equation can also be rewritten as a function of frequency:

$$m(\ddot{h} + \xi_h \omega_h \dot{h} + \omega_h^2 h) = L_{ae} \quad 5.3-a$$

$$I(\ddot{\alpha} + \xi_\alpha \omega_\alpha \dot{\alpha} + \omega_\alpha^2 \alpha) = M_{ae} \quad 5.3-b$$

Where: ξ_h and ξ_α are damping ratios-to-critical, and ω_h and ω_α are the natural circular frequencies in the h and α degrees-of-freedom, respectively.

For a certain wind speed, the force functions, L_{ae} and M_{ae} , are function of time, frequency and response as discussed in the coming section. The solution of this equation is not easy, as in the Duhamel integration or in other classical time domain analysis. The solution is in both the frequency and the time domain with one domain having to be transformed to the other. The next section discusses the solution of the equation of motion of the self-induced forces.

5.5.2 Self-induced Forces

For steady motion of thin symmetrical airfoil across a uniform airflow at an angle of attack α , the lift force based on the potential flow theory is given by:

$$L = \frac{1}{2} \rho U^2 B \frac{dC_L}{d\alpha} \alpha \quad 5.4$$

where, U is the incoming flow velocity with no turbulence and B is the plate width. C_L is the coefficient of lift per unit span, $dC_L/d\alpha$ is the coefficient of lift gradients.

Although flutter in its details involves nonlinear aerodynamic behavior, it has been possible in a number of instances to treat the problem successfully by linear analytical approaches. The justification for the linearization of flutter analysis is that the structure response is usually treatable as linearly elastic and follows exponentially modified sinusoidal oscillation. Moreover, the stable and the unstable regimes are separated by an incipient condition that may be treated as having small amplitude to onset it, Simiu and Scanlan (1996).

Scanlan and Tomko (1971) established the fundamentals of aerodynamic flutter of bridge decks. Sinusoidal motion is assumed to obtain the components of the aerodynamic flutter forces as indicated by:

$$L_{ae} = \frac{1}{2}\rho U^2 B \left(KH_1^* \frac{\dot{h}}{U} + KH_2^* \frac{B\dot{\alpha}}{U} + K^2 H_3^* \alpha + K^2 H_4^* \frac{h}{B} + KH_5^* \frac{\dot{p}}{U} + K^2 H_6^* \frac{p}{B} \right) \quad 5.5-a$$

$$D_{ae} = \frac{1}{2}\rho U^2 B \left(KP_1^* \frac{\dot{p}}{U} + KP_2^* \frac{B\dot{\alpha}}{U} + K^2 P_3^* \alpha + K^2 P_4^* \frac{p}{B} + KP_5^* \frac{\dot{h}}{U} + K^2 P_6^* \frac{h}{B} \right) \quad 5.5-b$$

$$M_{ae} = \frac{1}{2}\rho U^2 B^2 \left(KA_1^* \frac{\dot{h}}{U} + KA_2^* \frac{B\dot{\alpha}}{U} + K^2 A_3^* \alpha + K^2 A_4^* \frac{h}{B} + KA_5^* \frac{\dot{p}}{U} + K^2 A_6^* \frac{p}{B} \right) \quad 5.5-c$$

where: h , p and α are the vertical, lateral and twist deflections, ρ is the air density, U is the mean cross-wind velocity, B is the deck width, $K=B\omega/U$ is the reduced frequency, and ω is the circular frequency of oscillation. H_i , P_i and A_i are flutter derivatives, which are defined in the next section. The dot superscript indicates the first derivative with respect to time. Figure 5.3 shows the aeroelastic forces and their corresponding displacement for a three-degree-of-freedom bridge section.

Coupling of mode of vibration is significant in flutter analysis of long span bridges. Katsuchi H. and et al (1998), conducted multi-mode frequency domain flutter and buffeting analysis on the Akashi-Kaikyo Bridge, in Japan. The study considered coupling of modes to determine the aeroelastic response. It was concluded that the lateral flutter derivatives are significant in initiating flutter for very long-span bridges.

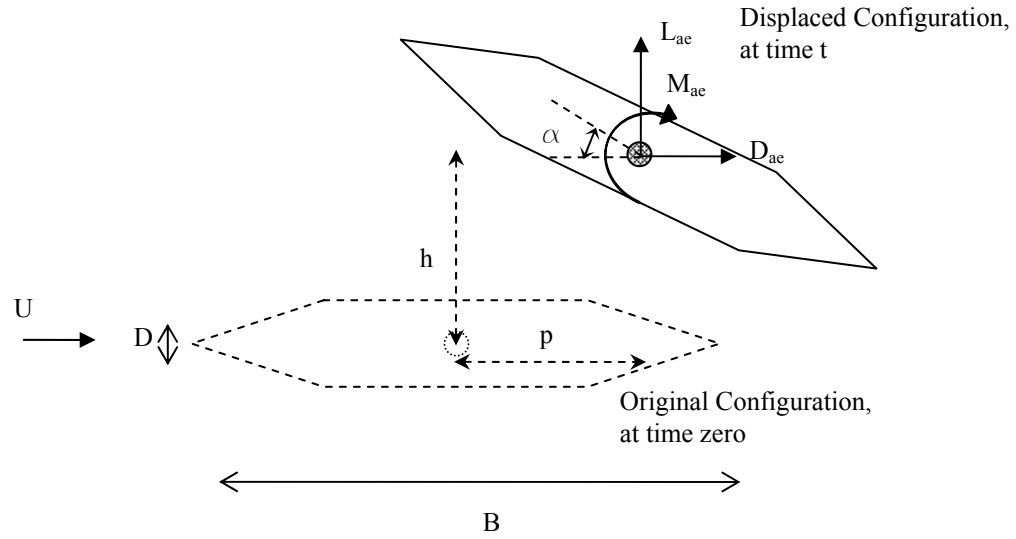


Figure 5.3: Flutter forces on a three degrees-of-freedom bridge section.

5.5.3 Flutter Derivatives

Flutter derivatives, also known as *aerodynamic derivatives*, are coefficients of the mathematical model of the aeroelastic force and are indicated by the H's, A's and P's terms in Equations 5.5. They portray the variation in the wind force due to the alteration in the boundary layer with respect to the induced frequency and the wind speed simultaneously. The geometry of the solid body has the primer effect. These coefficients are function of the *reduced frequency* K , or alternatively the *reduced velocity* U_r :

$$K = \frac{B\omega}{U} = \frac{B(2\pi n)}{U} = \frac{2\pi}{U_r} \quad 5.6$$

where: U is the oncoming laminar wind speed, B is the deck width, ω and n are the angular and the natural frequencies of the deck.

Research has recently been conducted to extract wind derivatives based on theoretical bases. Most of the recent advances done in this regard are adopted from aeronautical engineering. Traditionally, aerofoil or extremely thin-plate were the typical sections to be studied. The understanding of airfoil flutter and its derivatives in incompressible flow was reached through the potential-flow theory, done independently by Kussner and Theodorsen, and then applied to a flat plate.

Wagner (1925) proposed a formulation for the lift force as a function of time for a theoretical flat plate airfoil due to an impulsive change in the angle of attack. Wagner used superposition integral to estimate the indicial lift function. Theodorsen (1935), however, determined the lift and the moment forces based on sinusoidal oscillating airfoil in a uniform airflow. Theodorsen introduced a complex circulation function, which is function of the frequency of oscillatory motion (*refer to Appendix E*)

Bridge engineering researchers investigated the possibility of applying the Theodorsen function on bluff bodies. Although it is found that there is a fairly close parallelism in form between the problems of the aerodynamic instability of suspension bridge decks and flutter of airfoils, the latter should not be carried beyond its logical usefulness and must be used only as a guide in the study of bridge flutter, Scanlan et. Al (1971). Early experiments on extracting flutter derivatives for bridge decks were conducted by Ukeguchi, Sakata, and Nishitani (1966).

For a full mode analysis there are six lateral terms for each of the (P's) (H's) and (A's) for flutter derivatives, as shown in Equations 5.5. These coefficients can be extracted using sectional wind tunnel tests such that only a representative segment along the span length is modeled and tested. The lateral wind coefficients are unlike other flutter coefficients since they are found to be correlated to the static drag coefficient. Thus, they do not need to be extracted using oscillating model in wind tunnel.

The following is a discussion of the flutter derivatives. Extraction methods are briefly discussed. A comprehensive discussion of the behavior and the significance of the flutter derivatives is incorporated. Examples, based on previous studies are included to help in defining the range and the shape of the aerodynamic derivative curves. The results of the coming discussion are employed to synthesize flutter derivative curves for closed-grates stiffened-truss deck. This will be utilized in the flutter analysis of the Second Tacoma Narrows Bridge wind response analysis.

5.5.3.1 Extracting Flutter Derivatives

Aerodynamic derivatives of bluff bodies can be extracted from wind tunnel tests, using a prototype section of the superstructure. There are three procedures for accomplishing such a task:

- 1) Conducting vibration tests by giving prescribed vertical and torsional displacements to the bridge deck and then the aerodynamic derivatives are determined based on the transient behavior that occurs after releasing the bridge deck.

2) Applying the forced oscillation and using pressure measurements at number of pressure taps on the model.

3) Conducting buffeting tests where the behavior of the superstructure is observed under variable wind velocities.

Scanlan et al (1971) introduced an experimental setup with the basic theory and technique needed to extract flutter coefficients experimentally. The research tested a standard airfoil, NACA 0012, and compared the results with the theoretical values based on the Theodorsen function and exponentially modified sinusoidal harmonic response. Flow regime is assumed to be a low-speed low-turbulence incompressible flow. Figure 5.4 shows the results obtained by the experiments and the corresponding theoretical curve. Note that discrepancies from the theory exist. The experimental A_2 coefficient is reduced by a factor equal to 4.54, to match with the theory. Experimental values of H_1 and H_2 show considerably deviation from the Theodorsen function. The disagreement in H_1 is due to some limitation in the proposed experimental procedure as the torsional motion is initially blocked rather than permanently restrained. This causes the torsional motion to increase due to the inherently large coupling between the vertical and the torsional motion. This affects the calculation of H_2 and H_3 as well since both of them are function of H_1 .

Experimental computations of the aerodynamic derivatives involve some uncertainties that influence the quality of the results. Curve fitting seems acceptable, but

need not to be accurate in for bridge decks which have non-uniform curves for their aerodynamic coefficients Sarkar (1986).

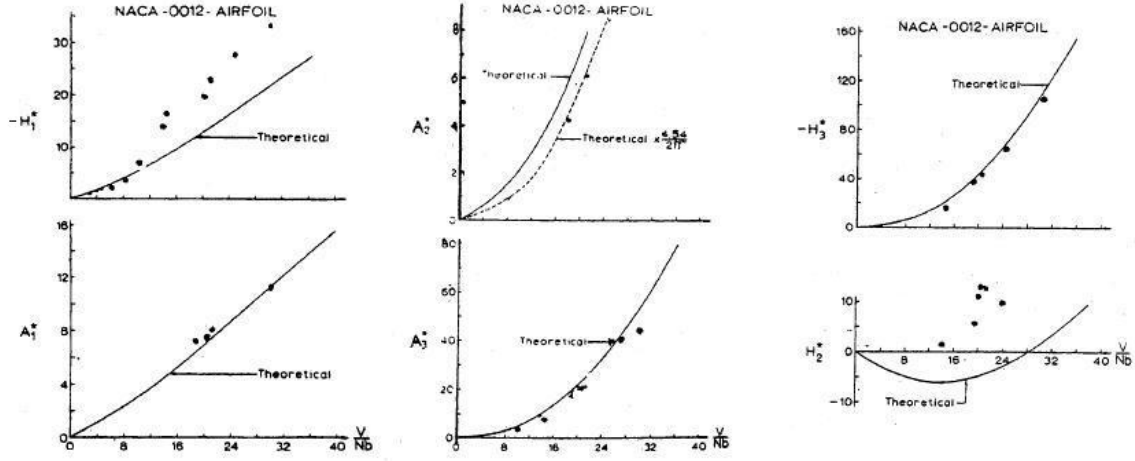


Figure 5.4: NACA-0012-Airfoil test results, for H's and A's, by Scanlan and Tomko (1971)

Brar et al (1996) established a theoretical basis to determine flutter derivatives directly from an indicial function without using Theodorsen-like circulation function. He employed Wanger's function in combination with the expression flutter oscillatory motion proposed by Scanlan and Tomko (1971). However the flutter derivative that relates to the non-circulatory effects was not appropriately estimated. The study recommended further investigations to validate the method for bluff bodies. The bluff body aerodynamic derivatives, in Equations 5.5, written in terms of the Theodorsen coefficients for flat plates flutter analysis, are given in Equation 5.7.

$$\begin{aligned}
 H_1^* &= -\frac{\pi F(k)}{k} & A_1^* &= -\frac{\pi F(k)}{4k} \\
 H_2^* &= -\frac{\pi}{4k} \left[1 + F(k) + \frac{2G(k)}{k} \right] & A_2^* &= -\frac{\pi}{16k} \left[1 - F(k) - \frac{2G(k)}{k} \right] \\
 H_3^* &= -\frac{\pi}{2k^2} \left[F(k) - \frac{kG(k)}{2} \right] & A_3^* &= \frac{\pi}{8k^2} \left[F(k) - \frac{kG(k)}{2} \right]
 \end{aligned} \tag{5.7}$$

$$H_4^* = \frac{\pi}{2} \left[1 + \frac{2G(k)}{k} \right]$$

$$A_4^* = \frac{\pi}{4} \frac{G(k)}{k}$$

Gu M. et. al. (2000) adopted spring-suspended section model and proposed a method to extract flutter derivatives based on Scanlan's formulation. The study consolidates the damping and stiffness matrices of the governing equation of motion into a damping and stiffness matrices of the wind-bridge system. That is, the response variables in the self-excited wind force function are combined with the damping and stiffness terms of the structure. The response of the bridge is approximated by the exponential function. Least square method is used to optimize the error based on the iterative procedure. The wind derivative is then computed based on the damping and stiffness matrices of the wind-bridge system and those of the structure itself. The wind derivatives obtained by the study were positively comparable with those obtained by Scanlan's theory.

Extraction of the lateral flutter derivative is done by wind tunnel experiments. It is then correlated to the static wind coefficients, namely, the drag coefficient Singh et al (1996). The following relations given in equation 5.8 are suggested to find the first three lateral flutter derivatives:

$$P_1^* = -\frac{2}{K} C_D \quad 5.8-a$$

$$P_2^* = -\frac{1}{K} \frac{dC_D}{d\alpha_w} \quad 5.8-b$$

$$P_3^* = -\frac{1}{K^2} \frac{dC_D}{d\alpha_w} \quad 5.8-c$$

where: K is the reduced frequency, C_D is the static drag coefficient, and α_w is the angle of incident of the wind.

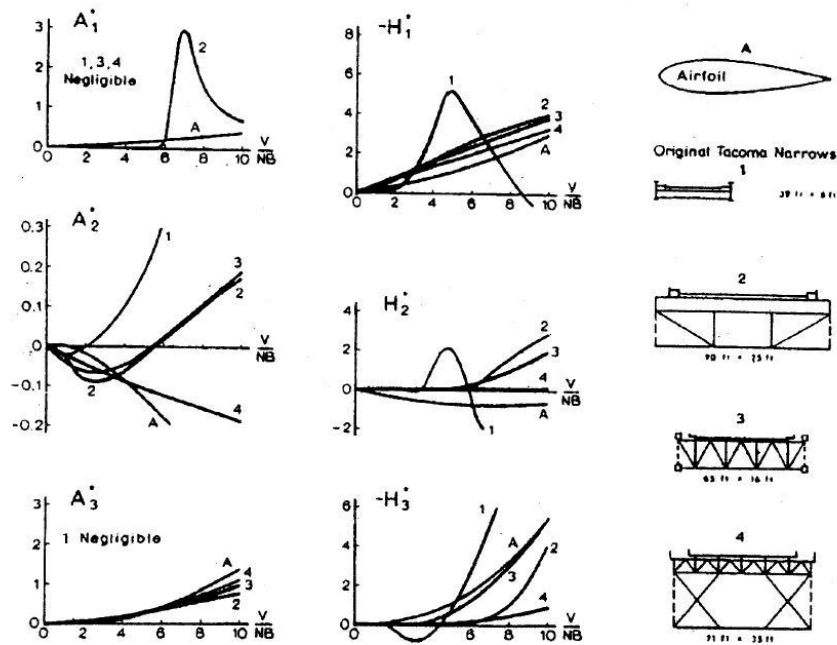
The flutter derivatives theory is conceptually, well established. Experimental research done by Scanlan and other investigators are acceptable to evaluate the parameters of the linearized system of aeroelastic forces. A procedure to determine all of the 18 flutter derivatives in a single test, at each reduced frequency level, using three-degree-of-freedom suspension and the application of a state-of-the-art system identification technique has been developed by Sarkar et al. (1994).

The ongoing research of evaluating the values of flutter derivatives using analytical models, such as computational fluid dynamics are still under investigation. Thus, experimental tools are still essential to validate the new analytical method.

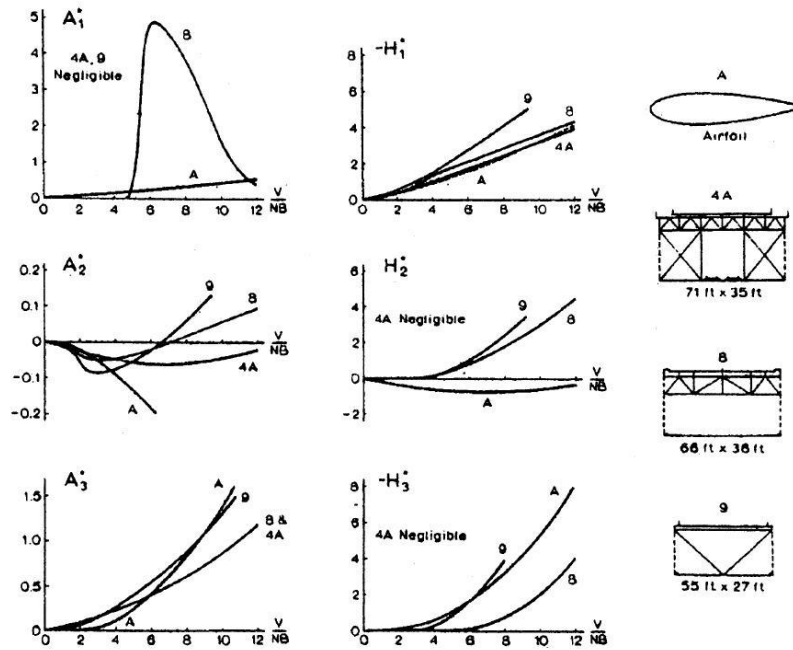
5.5.3.2 Parametric Analysis

Parametric studies have been conducted to examine the trends of flutter derivatives with respect to the bridges physical properties. These include deck shapes and configurations, and the wind properties such as turbulence intensity.

Scanlan and Tomko (1971) extended their experiments to extract the flutter derivatives for different types of representative suspension bridge decks, including closed-box, H-sections and stiffening truss. The plots shown in Figure 5.5 are some selected results from the experiments done on truss-stiffened cross sections.



set A



set B

Figure 5.5 : Results for airfoil, Original Tacoma Narrows Bridge Deck, and six typical truss-stiffened bridge decks, by Scanlan and Tomko, (1971)

The aerodynamic coefficients depend on the ratio of the wind speed and the frequency excited. They are however, independent of damping. The curves shown in Figure 5.5 are function of the reduced velocity, which is the ratio of the oncoming laminar wind speed to the frequency excited, in Hertz, times the width of the superstructure. The shape or the magnitude of the curves is solely affected by the geometrical configuration of the model.

If fluid-structure-interaction is considered, the wind derivatives could be contemplated as the reflection of the interaction of the wind boundary layer and the excited solid body. For example, in Figure 5.5 – set A, curve number one is for the original Tacoma Narrows Bridge deck is remarkably different from the other curves. This is due to the vortex-shedding behavior in the wind boundary layer, associated with the bridge motion, which has a significant effect on H-shape sections. However, this phenomenon is insignificant in the truss-stiffened cross sections shown. The curves are derived assuming that the lift force and the vertical deflection are both positive downward, and the twisting motion and moment are both positive with the windward edge upward. If this sign convention is reversed the terms H_2 , H_3 , A_1 and A_4 should be reversed in sign. This would not affect the flutter analysis results, as discussed later in this chapter. The following is a discussion of the first three aerodynamic coefficients for left A_i and moment H_i and A_i ($i=1, 2$ and 3):

The H_1 Coefficient represents the response of the vertical motion with the torsional degree –of freedom initially blocked, i.e., ($\alpha(0) = 0$). The figure shows that all bridges

with open-truss stiffened decks are close in response to an airfoil. However, the H-shape section, with its considerable side girders, diverts from the airfoil response. In most cases, the airfoil results are the lower bound, with a negative value, for the other opened truss-stiffened bridges.

The H_2 and H_3 coefficients represent the effect of the torsional oscillation on the buildup or decay of the vertical motion. For an example it is observed from experiments that for an H-shape the increase in the torsional oscillation frequency is associated with reduction in the vertical oscillation. This can be depicted by these two coefficients. For an example, curve 1 in Figure 5.5 increases with the increase of the reduced speed. Then it is swiftly reduced in the negative value causing a sudden reduction in the lift force and thus a sudden increase in the torsional oscillatory frequency to converge in values with the structural torsional frequency. This behavior is not exhibited by other deck shapes.

For open truss-stiffened decks the H_2 lies well above the airfoil curve and is always positive. This implies the opposite behavior exhibited by the H-shape deck of the Original Tacoma Narrows Bridge. The H_3 coefficient, however, shows similar behavior to the H-shape deck at a high reduced frequency. If these two aerodynamic coefficients reduce the aerodynamic vertical force at a high reduced wind speed, it is most probable that coupling between the heaving and torsional flutter will occur.

The effect of the vertical motion on the torsional flutter usually is not significant as shown by the A_1 curves of Figure 5.5. This coefficient may contribute to the response

when strong coupling between the two modes takes place at a certain frequency. At that point the term A_1 increases suddenly and then decreases to a low value, as shown in curve 1.

Generally A_1 has a relatively negligible contribution to the flutter condition for most of the bridge decks investigated in the literature. The effect of the A_1 coefficient on the stability behavior appears in airfoil and thin plates such that it induces the torsional branch-coupled flutter despite the adverse effect of A_2 after the torsional motion is initiated.

The A_2 coefficient is an indication of the torsional stability of a bridge section having the vertical motion restrained, i.e. ($h(t) = 0$). It is correlated to the torsional aerodynamic damping and the possibility to have torsional divergence. The A_2 curve provides a very useful rule-of-thumb to judge and compare the aerodynamic stability, even though the contribution of the other aerodynamic derivatives might have considerable positive effects. A steep negative slope is an indication of torsional stability. As indicated in Figure 5.5, the airfoil and the bridge section number 4 are the most stable sections, while the Original Tacoma Narrows Bridge is the least stable section since the A_2 coefficient is well-correlated to the vortex-shedding effect. Flat sections or streamlined bodies have close values to the A_2 of airfoil. Moreover, grating-location, for plate-like decks with open grates, has significant effect on the A_2 value. It is found that installing the open grates at the edge panels of the deck provides more aerodynamic stability, as shown in Figure 5.6.

The A_3 coefficient reflects the difference between flutter and natural torsional frequencies, that is, the aerodynamic stiffening effect upon the critical torsional frequency. It is found that the flutter frequency and the natural torsional frequency are between 1% and 3%. For most of the tested sections A_3 is found to be fairly close to that of the airfoil.

It could be observed that each of the H's and A's coefficients portray a certain behavior of the self-excited forces. Thus the optimal design of suspension bridge decks could be depicted using these coefficients such that the use of an airfoil trend is the most preferable. The challenge is to find a section, mostly a bluff body, with satisfactory stiffness and aerodynamic properties. Different techniques are suggested to improve the aerodynamic characteristics of suspension bridge superstructures. Such techniques are streamlining the deck shape, as originally done in the Second Severn Bridge, installing flaps at both edges, or introducing grates in the superstructure, as in the case of the Second Tacoma Narrows Bridge. The Messina Strait Bridge, which is under planning in Italy, comprises all the above three techniques. This would make its 2.05 miles (3300 m) main span possible, Brancaloni and Diana (1993). Several studies are done on each of the three techniques.

The emphasis here is on studying the effect of altering the grates on the aerodynamic response of the bridge. It is of interest, for the purpose of the case study discussed in Chapter 6, to investigate the effect of deck grates on the aerodynamic behavior. A

comparison between the solid deck, open-grated deck at the sides and the Theodersen function is essential to deduce the general trend of the aerodynamic curves. This will be employed to synthesize wind derivative curves that substitute the deficiency in experimental data.

Matsumoto et al (2001) conducted a parametric study, using a series of wind tunnel tests on plate-like bridge sections with five panels. The tests are conducted with three wind speeds of 5, 10 and 15 m/s (11.2, 22.4 and 33.6 mph). Matsumoto's study discusses the influence of the opening ratio and the location of grating on flutter instability based upon their aerodynamic derivatives and flutter analysis. Different values of the opening ratio (OR) are suggested in the test, with OR varying from 20% to 100% with 20% increments. The different deck configurations and the aerodynamic derivatives for grating-installed with OR=40% are shown in Figure 5.6.

For the Second Tacoma Narrows Bridge, the edge grates next to the sidewalks, are supposed to be open as in Type 2. Note that there are dissimilarities between the bridge deck configurations and the Matsumoto et al (2001) experiment sections. These differences are mainly due to the number of panels and the geometry of the open-truss stiffened decks which is different than that of the plate-like decks, as used in the experiments. The following conclusions are to be used along with the previous discussion to suggest a worst-case scenario for the H's and A's curves, relevant to the bridge problem.

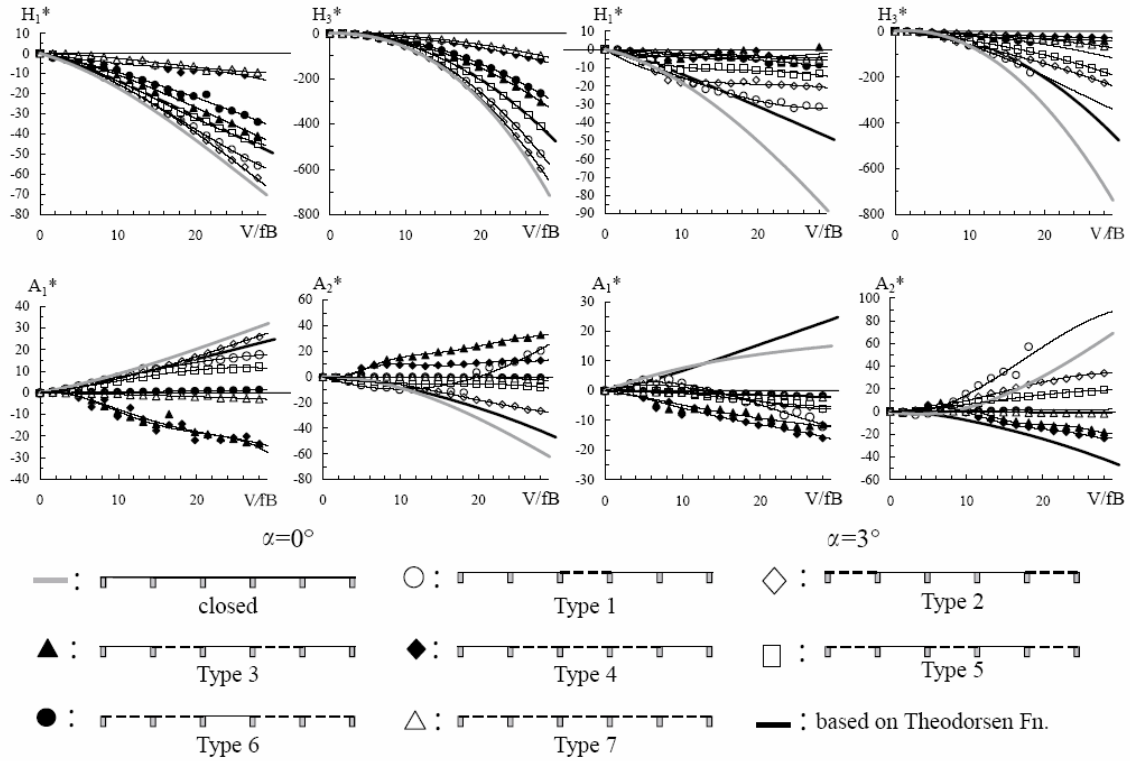


Figure 5.6: The aerodynamic derivatives, H_1 , H_3 , A_1 and A_2 for grating-installed girders, with $OR = 40\%$ and $\alpha = 0^\circ$ and $\alpha = 3^\circ$, Matsumoto et al (2001)

Figure 5.6 shows two sets of curves with each set comprising four aerodynamic curves, H_1 , H_3 , A_1 and A_2 , for the various deck configurations. For A_1 , H_1 and H_3 , the Theodorsen function represents the average aerodynamic coefficients of type 2 and closed deck configurations with $\alpha = 3^\circ$.

For A_2 , the most critical aerodynamic coefficient, reversing the sign of the Theodorsen function gives an average value between the closed deck and Type 2 configurations, for an angle of attack equal to 3° . Another comment on A_2 , as shown in Figure 5.6, is that having the grates placed at the middle panel, the aerodynamic stability is significantly reduced. The most optimal location of the grates is at the edge panels,

which is the scheme recommended to redesign the bridge deck of the second Tacoma Narrows Bridge.

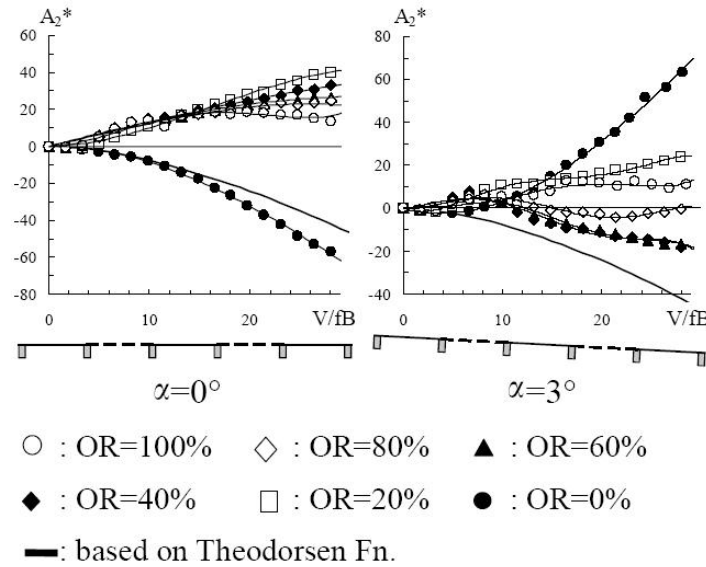


Figure 5.7: The Aerodynamic derivative, A_2 for Type 3, Matsumoto et al (2001)

The effect of the OR could be observed from Figure 5.7 which shows the A_2 flutter derivative curves of different OR's for Type 3 configuration. It could be observed that having the grates opened, with OR greater than or equal to 20%, the dispersion among the A_2 curves is very small particularly for low values of the reduced velocity. It is of interest to note that with all grates closed the A_2 is fairly close to the airfoil behavior. For an angle of attack of 3° , the A_2 curves are rather scattered and the behavior of some curves, such as the closed grates, are reversed. For most bridges, the OR of the grates, is most likely to be between 20% and 40% as the case with the Second Tacoma Narrows Bridge (25.5%), See Appendix D.

The lateral flutter derivatives of bridge decks, P_i , are not well-addressed in most of the flutter analysis studies. It is assumed that the coupling between the lateral and the vertical oscillations is negligible. It is found that for suspension bridges with relatively long center-span, such as the Akashi-Kaikyo Bridge, the coupling of the lateral mode and the other modes is considerable, Katsuchi et. al. (1998).

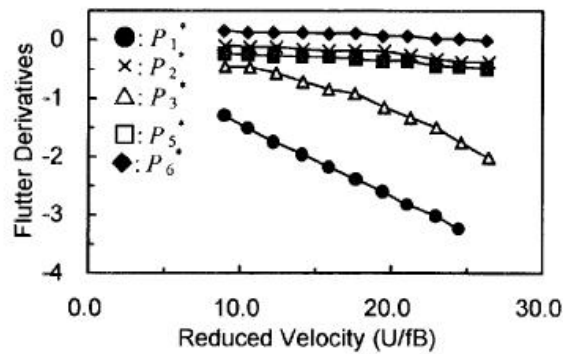


Figure 5.8: Lateral flutter derivatives of Akashi-Kaikyo Bridge, Katsuchi et al. (1998)

The most substantial coefficient among the lateral flutter coefficients is the P_1 . This is due to the negligible coupling between the torsional and the lateral modes of vibration. Coupling with the lateral mode occurs when higher modes of vibration are excited. In relatively short span bridges, coupling between the torsional mode and the lateral mode is not very probable. The second significant lateral aerodynamic derivative is the P_3 , which represents the effect of torsional motion on the lateral aerodynamic force. Figure 5.8 shows five of the lateral aerodynamic coefficients of the Akashi-Kaikyo Bridge. The P_4 is not shown in the figure, that is because there is not any theoretical expression for P_4 and it was never previously determined before Singh et al. (1996), who experimentally determined this coefficient for the Tsurumi and Deer Isle Bridges. Singh et. al. (1996)

concluded that the P_4 has a “stiffening” effect on the sway motion. It is however possible, as described in the pervious section, to at least calculate the terms P_1 , P_2 and P_3 if the static drag coefficient is known.

Effect of turbulence is discussed by Scanlan and Lin (1978), Huston et al (1988), Diana et al (1993) and Sarkar et al (1994). It is found that for most of the eight flutter derivatives (A 's and H 's), the turbulent flow values differ only slightly from their smooth flow counterparts, such that the smooth flow values seems to represent the mean values about which the turbulent flow values fluctuate. It is found that H_3 and A_3 are less influenced by the turbulence of flow as they seem to match perfectly in both cases. It is generally determined that the effect of turbulence is very slight on the flutter derivatives, and thus on evaluating the aeroelastic forces.

The aeroelastic behavior, represented by the flutter derivatives, is mainly driven by the geometry of the structure. There is critical dependence of the aeroelastic behavior on even minor details such as a deck railing Jones et al (1995).

5.5.3.3 Solving for Flutter Condition

5.5.3.3.1 Two-Degree-of-Freedom System

Wind Critical Flutter condition is the state of motion at which the zero damping is attained and oscillation buildup is initiated. This could be noticed in wind tunnel testing, with prototype of the whole structure as the oscillation time history diverts at a certain wind speed and reaches resonance-like motion. Using the time history function the critical frequency could then be identified. The mathematical solution of the flutter

condition is however more complicated. The following discussion is limited to the two degree-of-freedom system such that the lateral motion is ignored.

The vertical and torsional modes that couple in the flutter vibrations are described by Equation 5.9,

$$h(x,t) = \xi_m(x)z(t) \quad 5.9-a$$

$$\alpha(x,t) = \alpha_m(x)q(t) \quad 5.9-b$$

in which, ξ_m and α_m are the vertical and the torsional modes that couple to produce flutter vibration along the deck axis, x . The $z(t)$ and the $q(t)$ are single generalized displacement of the vertical and the torsional displacement, respectively.

Referring to the equations of motion in section 5.4.2 and the self-induced forces in section 5.4.3, and assuming that the vertical deflection, h , and the angular rotation, α , of the bridge deck follow complex exponential harmonic motion given by the following expression:

$$X = X_0 e^{i\omega t}$$

The solution for this equation will be in the form of $\omega = \omega_1 + i\omega_2$. The ω_2 , if greater than zero, represents decay of motion, and represents divergent if negative in value. Let the critical reduced frequency K_c be the value for which $\omega \approx \omega_1$, that is at the critical flutter condition ($\omega_2 \approx 0$).

The following is defined to help in the derivation of the flutter function:

Recalling Equation 5.6,

$$K = \frac{B\omega}{U}$$

K is the reduced frequency, U is the wind speed, B is a characteristic length, usually the deck width, and ω is the frequency. Therefore at flutter the following is assumed

$K=K_c$, $U=U_c$ and $\omega=\omega_1$. For the reduced vertical structural frequency $K=K_h$ and $\omega=\omega_h$.

For the reduced torsional structural frequency $K=K_\alpha$ and $\omega=\omega_\alpha$.

$$s = \frac{Ut}{B} \quad 5.10$$

where s is the reduced time (or distance), and t is time. Using the chain rule, the first derivative of a variable function of t, is as follows,

$$\dot{()}' = \frac{d()}{dt} = \frac{d()}{ds} \frac{ds}{dt} = ()' \frac{U}{B} \quad 5.11$$

$$\ddot{()}'' = \frac{d(\dot{()})}{dt} = ()'' \frac{U^2}{B^2} \quad 5.12$$

Operating Equations 5.11 and 5.12 on h and α , the equation of motion and the aeroelastic forces, Equations 5.3 and 5.5, respectively, the equation of motion are reduced to

$$h'' + 2\zeta_h K_h h' + K_h^2 h = \frac{\rho B^3}{2m} \left[KH_1^* \frac{h'}{B} + KH_2^* \alpha' + K^2 H_3^* \alpha + K^2 H_4^* \frac{h}{B} \right] \quad 5.13-a$$

$$\alpha'' + 2\zeta_\alpha K_\alpha \alpha' + K_\alpha^2 \alpha = \frac{\rho B^4}{2I} \left[KA_1^* \frac{h'}{B} + KA_2^* \alpha' + K^2 A_3^* \alpha + K^2 A_4^* \frac{h}{B} \right] \quad 5.13-b$$

Note that the left hand side and the right hand side are multiplied by B^2/U^2 .

Recalling the proposed solution form of the response,

$$h = h_0 e^{i\omega t} = h_0 e^{iKs} \quad 5.14-a$$

$$\alpha = \alpha_0 e^{i\omega t} = \alpha_0 e^{iKs} \quad 5.14-b$$

where, h_0 and α_0 are initial response amplitudes. The derivatives of Equations 5.14

are:

$$h' = h_0 K e^{iKs}, \text{ and } h'' = -h_0 K^2 e^{iKs} \quad 5.15\text{-a}$$

$$\alpha' = \alpha_0 K e^{iKs}, \text{ and } \alpha'' = -\alpha_0 K^2 e^{iKs} \quad 5.15\text{-b}$$

Equations 5.13 can then be reduced to,

$$\left[-K^2 + 2i\zeta_h K_h K + K_h^2 - \frac{\rho B^2}{2m} K^2 (iH_1^* + H_4^*) \right] \frac{h_0}{B} - \frac{\rho B^2}{2m} K^2 [iH_2^* + H_3^*] \alpha_0 = 0 \quad 5.16\text{-a}$$

$$\left[-\frac{\rho B^4}{2I} K^2 (iA_1^* + A_4^*) \right] \frac{h_0}{B} + \left[-K^2 + 2i\zeta_\alpha K_\alpha K + K_\alpha^2 - \frac{\rho B^4}{2I} K^2 (iA_2^* + A_3^*) \right] \alpha_0 = 0 \quad 5.16\text{-b}$$

Note that Equation 5.16 can be simplified in matrix form, as arranged. The critical condition would be the roots of the determinant of the matrix. Note that in the above equation no coupling term is added. It is however desired to add the coupling terms and use the generalized response, as described in Equation 5.17.

Note that the coupling terms of the aerodynamic force are those associated with H_2 and H_3 for the left and A_1 and A_4 for the moment. A non-dimensional coefficient could be added to represent the coupling effect, based on the mode shape, as shown in equation 5.17-a.

$$C_{\xi_m} = \frac{\int_{Deck} \xi_m(x) \alpha_m(x) dx}{\int_{Deck} \xi_m^2(x) dx} \quad 5.17\text{-a}$$

$$C_{\alpha_m} = \frac{\int_{Deck} \xi_m(x) \alpha_m(x) dx}{\int_{Deck} \alpha_m^2(x) dx} \quad 5.17\text{-b}$$

Mode coupling depends on the product $C_\xi C_\alpha$ of the non-dimensional coefficients, such that the mode shapes likely to couple give $C_\xi C_\alpha$ a value close to one, whereas those that are unlikely to couple will yield a value of $C_\xi C_\alpha$ close to zero. For example, mode coupling is impossible combining a symmetric vertical mode and an asymmetric torsional mode, that gives $C_\xi = C_\alpha = 0$.

Divide Equation 5.13 by $(K\xi)^2$, and assume the following:

$$\Omega = \omega / \omega_\xi = K / K_\xi, \quad \gamma_\omega = \omega_\alpha / \omega_\xi = K_\alpha / K_\xi,$$

$$\gamma_m = m_e / (\rho b^2) \quad \text{and} \quad \gamma_I = I_e / (\rho b^4)$$

The following is obtained:

$$\left[-\Omega^2 + 2i\zeta_h \Omega + 1 - \frac{\Omega^2}{2\gamma_m} (iH_1^* + H_4^*) \right] \frac{h_0}{B} - \left[\frac{C_{\xi_m} \Omega^2}{2\gamma_m} (iH_2^* + H_3^*) \right] \alpha_0 = 0 \quad 5.18-a$$

$$\left[-\frac{C_{\alpha_m} \Omega^2}{2\gamma_I} (iA_1^* + A_4^*) \right] \frac{h_0}{B} + \left[-\Omega^2 + 2i\zeta_\alpha \gamma_\omega \Omega + \gamma_\omega^2 - \frac{\Omega^2}{2\gamma_I} (iA_2^* + A_3^*) \right] \alpha_0 = 0 \quad 5.18-b$$

The solution of flutter condition is obtained by setting the determinant of the coefficient matrix for Equations 5.18 to zero and separating the real and the imaginary parts. This gives a fourth order polynomial function with the following format:

$$R_4 \Omega^4 + R_3 \Omega^3 + R_2 \Omega^2 + R_1 \Omega + R_0 = 0 \quad 5.19-a$$

$$I_4 \Omega^4 + I_3 \Omega^3 + I_2 \Omega^2 + I_1 \Omega + I_0 = 0 \quad 5.19-b$$

The coefficients are identified as follows, *see Appendix C*:

$$R_1 = 0$$

$$R_2 = -\gamma_\omega^2 - 4\zeta_\alpha \zeta_\xi \gamma_\omega - 1 - \frac{A_3^*}{2\gamma_I} - \frac{\gamma_\omega^2 H_4^*}{2\gamma_m}$$

$$\begin{aligned}
R_3 &= \frac{\zeta_\alpha \gamma_\omega H_1^*}{\gamma_m} + \frac{\zeta_\xi A_2^*}{\gamma_I} \\
R_4 &= 1 + \frac{H_4^*}{2\gamma_m} + \frac{A_3^*}{2\gamma_I} + \frac{(C_\xi C_\alpha A_1^* H_2^* - A_2^* H_1^* + H_4^* A_3^* - C_\xi C_\alpha H_3^* A_4^*)}{4\gamma_m \gamma_I} \\
I_1 &= \frac{-\gamma_\omega^2 H_1^*}{2\gamma_m} - \frac{A_2^*}{2\gamma_I} \\
I_2 &= -2\zeta_\alpha \gamma_\omega - 2\zeta_\xi - \frac{\zeta_\alpha \gamma_\omega H_4^*}{\gamma_m} - \frac{\zeta_\xi A_3^*}{\gamma_I} \\
I_3 &= \frac{H_1^*}{2\gamma_m} + \frac{A_2^*}{2\gamma_I} + \frac{(A_2^* H_4^* + A_3^* H_1^* - C_\xi C_\alpha H_3^* A_1^* - C_\xi C_\alpha H_2^* A_4^*)}{4\gamma_m \gamma_I}
\end{aligned}$$

Since the original forth order format of the imaginary polynomial has a zero constant, it is reduced to a third order equation. Note that the sign convention of the vertical motion, which preserves the sign of A_1 , A_4 , H_2 and H_3 , does not change the solution of the flutter analysis.

The normalized frequency Ω , or alternatively the frequency ω , that simultaneously sets Equations 5.19-a and 5.19-b to zero, represents the flutter condition. Equations 5.19 are also function of the reduced frequency K , which is also a function of ω and U . It is not certain that there is a closed form solution for this condition.

It is suggested to try several values of the reduced frequency (K) and plot the real positive roots of Ω , for both equations. The intersection point of the plotted imaginary roots and the real roots represents the critical flutter condition, that is, $(K_c = f(\omega_c, U_c))$ and $\Omega_c = f(\omega_c)$. It is also possible to plot the reduced velocity, U_r , instead of reduced frequency K (see Equation 5.6). The critical frequency equals to $\omega_c = \Omega_c \omega_\xi$, and the

critical wind speed equals to $U_c = b\omega_c/K_c$. If more than one intersection point is found in the selected range of K , the one with the lowest U_c will be the required solution.

Therefore, a wide range of reduced frequencies should be tested to guarantee the lowest possible critical wind velocity.

A MATLAB code is developed to carry out the procedure discussed above, (*see Appendix B*). The eight flutter derivatives, A' 's and H' 's, are expressed in a matrix format, such that for each K value, arranged in an ascending way, the eight flutter derivatives are assigned sequentially. The calculation will be repeated over a range of prescribed reduced frequencies. The imaginary and the real roots are then plotted. The flutter derivatives are input as data points at certain values of K and not as a mathematical function. The flutter derivatives are obtained using linear interpolation. For smooth curves more data points are needed to obtain accurate analysis. Only flutter derivatives of a flat plate are programmed as a continuous function, based on the Theodorsen function. The program is tested using a case study of the Golden Gate Bridge.

5.5.3.3.2 Verification Problem

The flutter problem of the Golden Gate Bridge has been solved in several studies. Simiu and Scanlan (1996) introduced the problem in a simplified format and estimated the critical wind to be 50.9 mph (81.9 km/hr). Jain et al (1998) solved the multi-mode flutter problem taking into account the modal damping effect, different angles of attack and the first lateral flutter derivative P_1 . The flutter wind speed for a zero angle of attack is found to be 53.1 mph (86.1 km/hr), at 1.18 angular frequency. The lowest flutter speed

is found to be 49.21 mph (79.9 km/hr), at 1.19 rad/sec, for an angle of attack equal to $+5^\circ$.

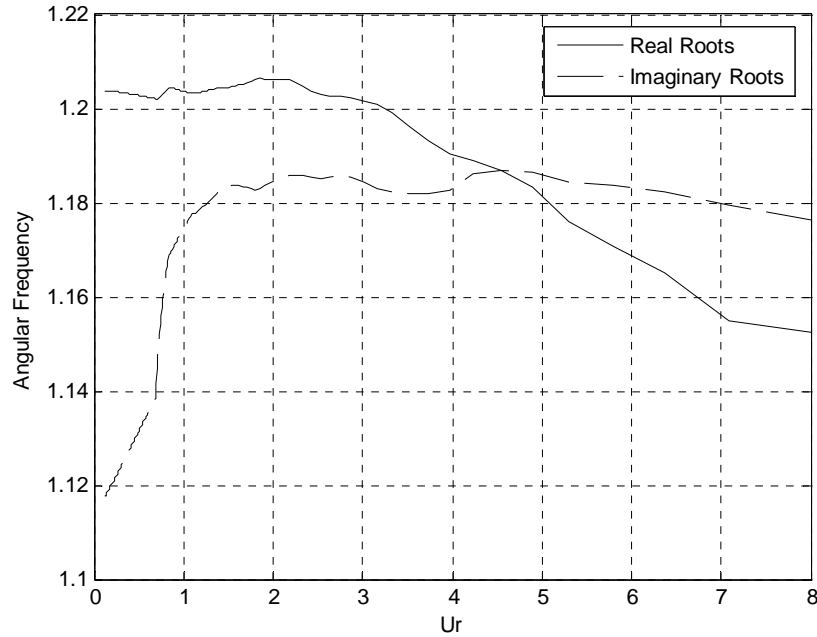


Figure 5.9: Flutter analysis for the Golden Gate Bridge

The analysis is conducted using the approach discussed in the previous section and the critical wind speed is estimated to be 49.6 mph (79.81 km/hr), at a frequency equal to 1.186 (0.188 Hz), for a zero angle of attack. This overestimates the flutter velocity by 4% if compared with Scanlan's simplified calculations, and 7% if compared with Jain multi-mode analysis. The critical condition is reached when the sixth mode of vibration, which is a vertical symmetric mode, coupled with the seventh mode, which is a torsional symmetric mode. Figure 5.9 shows the solution of Equations 5.18. The intersection of the imaginary and the real curves is the critical condition. The graph shows the relation

between ω and the reduced velocity U_r . Table 5.1 shows the parameters used in the analysis and the flutter derivatives are shown in Figure 5.10.

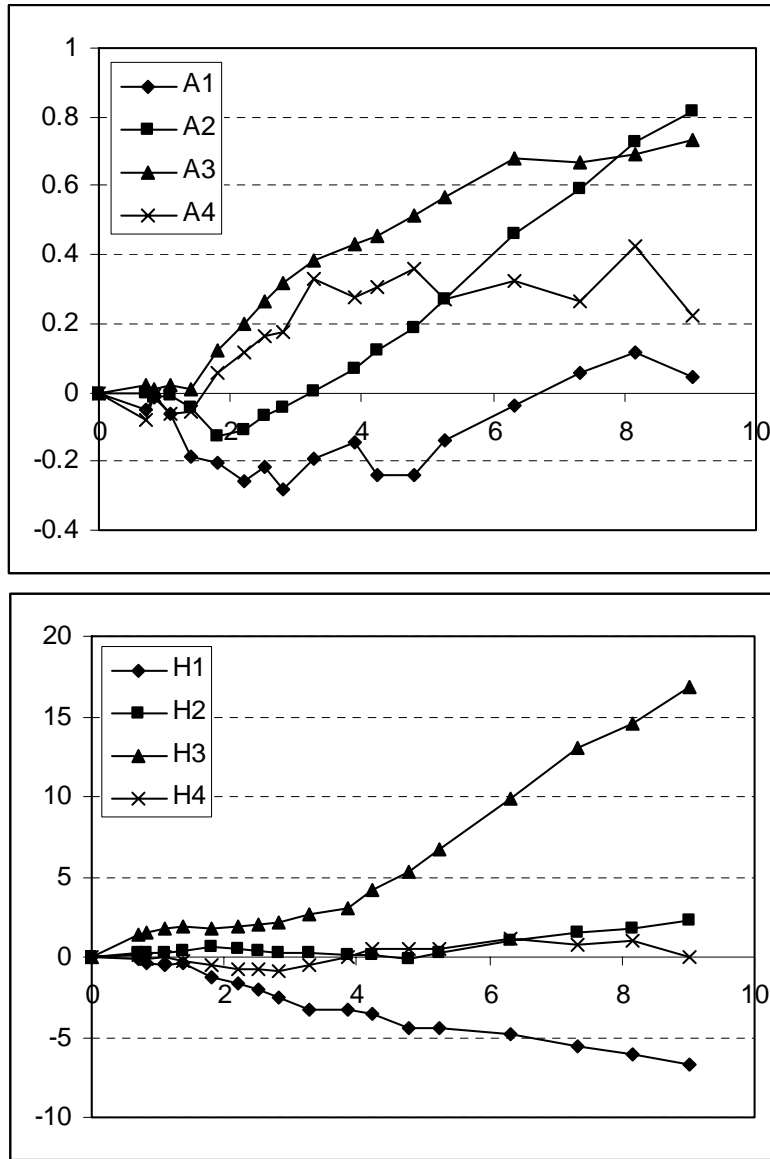


Figure 5.10: Flutter Derivatives of the Golden Gate Bridge Jain et al (1998)

Table 5.1: Golden Gate Bridge flutter analysis parameters

Parameter	Value
B	27.5 m
ρ	1.2 kg/m ³
ω_{ξ} (6 th mode)	0.1638 Hz
ω_{α} (7 th mode)	0.1916 Hz
C_{ξ}	0.34

Parameter	Value
ζ_{ξ}	0.5%
ζ_{α}	0.5%
I_{ξ}	5,208 kg
I_{α}	3,680,000 kg.m ²
C_{α}	0.32

5.6 Flutter Criteria

Suspended structures are usually designed to handle a certain design wind speed. Most of the design codes, such as ASCE-7-98, suggest basic wind speed of 3-second 50 and 100-year return period wind speed with 95% confidence level, as a reference to calculate wind load. If flutter takes place in a slender suspended structure, the probability of failure will be extremely high. It is recommended, for such structures, to consider three-second gust 10,000-year return wind with 99% confidence level to establish the flutter criteria. An Nth-year return wind can be calculated as shown in the coming sections. This value should be averaged to hourly wind speed at the bridge deck elevation.

Displacement and acceleration responses of suspended structures are not a major concern at flutter conditions, since this type of structure is not designed to operate in those conditions and facility closure is the common procedure to ensure public safety. The response of a bridge should be checked to guarantee its serviceability under average wind speed and service loads. The performance history of the Second Tacoma Narrows Bridge proves the bridge serviceability under average loading conditions.

5.7 Estimation of Design Wind Speed

The homogeneity of wind speed, generated in the atmospheric layer, is affected by two main factors, namely, the distance from the ground and the roughness of the surrounding terrain, which is known as the exposure. The wind speed used in the analysis

should reference these two factors in addition to the averaging time, which could be the average in one-minute, one-hour, highest gust. To account for wind variability and to obtain reasonable statistical wind analysis, the average wind speed should be calculated over a sufficient long period of time, which is statistically defined as the period along which the mean value of the fluctuating wind speed component equals zero, Dyrbye and Hansen (1997).

The Tacoma Narrows is relatively an open water surface terrain surrounded by scattered grasslands and urban buildings, which corresponds to exposure C categories, as defined in the ASCE 7-98. Using Figure 6-1 in the standard, the nominal design 3-second gust wind at 33 ft (10m) above the ground for exposure C category is 85 MPH (38 m/s). This figure is calculated on an elevation that exactly matches the elevation of the bridge's superstructure, and thus, no further corrections are needed to calibrate for the height.

Generally, wind speed for the N-year period, U_N , could be calculated using the following approximated equation:

$$U_N = U_m + 0.78(\ln N - 0.577)\sigma \quad 5.20$$

where U_m and σ are, respectively, the sample mean and the sample standard deviation of the largest yearly wind speeds for the period of the record. The standard deviation of the sampling errors in the estimation of U_N can be expressed as:

$$SD(U_N) = 0.78 \left[1.64 + 1.46(\ln N - 0.577) + 1.1(\ln N - 0.577)^2 \right]^{1/2} \frac{\sigma}{\sqrt{n}} \quad 5.21$$

where n is the sample size. The 95% and 99% confidence intervals of the calculated sample mean of the largest yearly wind speed can be established as follows,

Confidence Level	Wind Speed Interval
95%	$U_N \pm 2SD(U_N)$
99%	$U_N \pm 3SD(U_N)$

The derivation of these relationships are based on Type I extreme value distribution and discussed in detail in Simiu and Scanlan (1996).

Wind speed calculated at certain elevation, z_r , on a specific terrain, can be extrapolated to other elevations, z , using the following relationship

$$U = U_r \left(\frac{z}{z_r} \right)^\alpha \quad 5.22$$

where U_r is the wind speed at the reference elevation, U is the required wind speed and is a constant and α equals to 0.147. The above equation is called the *wind profile power law*. Terrain roughness could also be incorporated in this law, (see Simiu and Scanlan (1996)).

The study conducted by RWDI Inc. (2003) on the existing and the new Tacoma Narrows Bridges, comprises the results of a statistical wind study of the narrows region. The study found that the 3-second gust 100-year return period wind equals to 91 MPH. The data used in the study is collected from three stations, namely, Tacoma Narrows Airport located 3 km west of the bridge site, McChord Air Force Base located 19 km southeast of the site, and Seattle Tacoma International Airport located 27 km northeast of

the bridge site. The data collected were 26, 24 and 35 years for the three stations respectively. The wind speed is also correlated to the bridge site elevation. A factor of 1.36 is suggested to find the equivalent 3-second gust 10,000-year return period wind from the 100-year wind, that is, 123.8 MPH. The equivalent mean hourly wind speed is 105.9 MPH. This value will be used as the flutter criteria of the bridge.

CHAPTER 6

FLUTTER ANALYSIS OF THE SECOND TACOMA NARROWS BRIDGE

6.1 Problem Statement

The following is an application on the theory and the methodology discussed in Chapter 5. The purpose of this case study is to estimate the critical wind speed of the Second Tacoma Narrows Bridge based on the classical flutter analysis.

The most systematic method to conduct this study is to use wind tunnel testing to find the aerodynamic derivatives of the bridge. However, this approach is not possible at this point because of unavailability of experimental data. The challenge is to synthesize the aerodynamic characteristics based-on the available experimental studies conducted on different configurations of the open truss-stiffened and plate-like decks. It is desired to suggest a set of wind derivatives that would produce the most severe aerodynamic loading using methodical judgment procedure.

6.2 Assumptions and Parameters

The following are the assumptions considered here for the flutter analysis.

1. The oncoming wind is assumed to be uniform with negligible variable component in magnitude, direction, and with the angle of attack being equal to zero.
2. Each vertical mode is assumed to be coupled with the higher torsional modes.

This is acceptable if the vertical modes of vibration are usually invoked before the torsional mode is considered.

3. The structural and frequency properties of the bridge calculated in Chapter 3 are used here in the analysis.
4. The wind parameters calculated in Chapter 4 are used in this chapter.
5. It is assumed that the superstructure follows the general trend of open-truss stiffened and the plate-like decks, Scanlan (1971) and Matsumoto (2001). The aerodynamic derivatives synthesized are generated at certain reduced velocities and interpolated linearly through the analysis.
6. The maximum reduced velocity is assumed to be 18. Since the lowest frequency of the structure is 0.44623 rad/sec and the maximum frequency included in the analysis is 3.9286 rad/sec, the assumed maximum reduced frequency covers wind speed range up to 208 mph. This range is very satisfactory compared with the maximum expected wind speed of 105.9 mph, as discussed in Chapter 4.

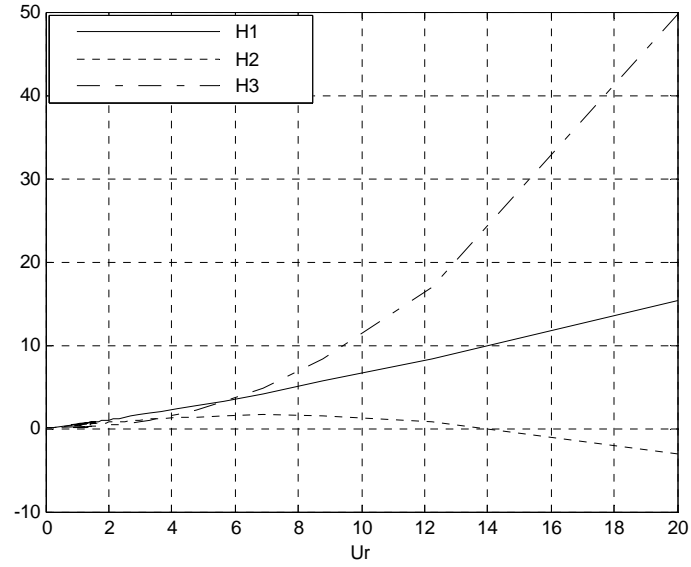
6.2.1 Synthesizing Wind Derivative

The created aerodynamic derivatives are used to estimate the wind response of the Tacoma Narrows Bridge. The modified superstructure is assumed to have grates at the edges and between the right lane and the sidewalks on each bound as suggested in the remodeling process. This also gives more reasonable assumption than considering the less stable cases that include the H-shape or the closed-grate deck sections. Conducting wind tunnel tests to verify this approach is needed for the bridge under consideration.

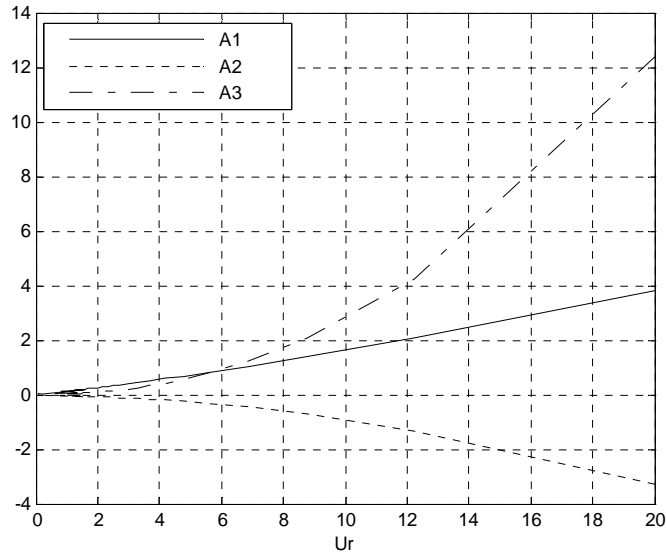
Table 6.1 summarizes the rules concluded from the discussion in Chapter 5 regarding the aerodynamic derivatives of stiffened open-truss and plate-like decks. The realization of these rules is shown in Figure 6.1.

Table 6.1: Assumptions used to Synthesize flutter coefficients

Coefficient	Rule
H1	Same as in the Theodorsen function
H2	Same as in the Theodorsen function
H3	Same as in the Theodorsen function
H4-H6	Assume negligible effect
A1	Same as in the Theodorsen function
A2	Same as in the Theodorsen function with reversed sign
A3	Same as in the Theodorsen function
A4-A6	Assume negligible effect
P1	$2C_D/K = 0.57/K$, consider the maximum C_D at $\alpha = -10^\circ$
P2-P6	Assume negligible effect



(a) lift aerodynamic coefficients



(b) moment aerodynamic coefficients

Figure 6.1: Synthesized flutter derivatives

6.2.2 Verification of the Synthesized Wind Derivative

The Golden Gate Bridge case study, presented by Scanlan, is recalled here to verify the synthesized curves. The suggested flutter derivatives are applied on the Golden Gate Bridge to calculate the critical wind speed and critical frequency, as shown in Figure 6.2.

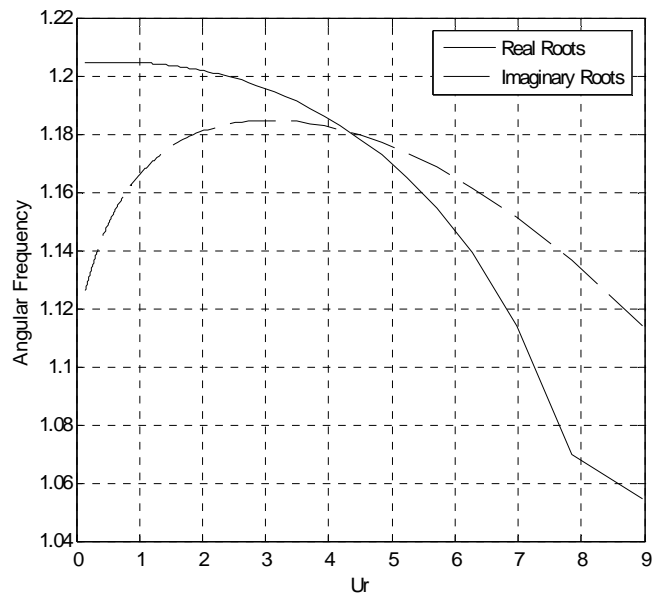


Figure 6.2: Flutter Analysis of the Golden Gate Bridge using the Flat Plate Theory

The critical condition shown in the figure is at critical frequency of 1.181 rad/sec and critical reduced wind speed of 4.3375, that is, 22.42 m/s or 50.15 mph, which is close to the value of 49.6 mph as calculated in chapter 5.

This verifies that the assumed aerodynamic coefficients represent the average trend of the stiffened-truss superstructures.

6.3 Results

The following are the results of the flutter analysis. This includes the critical frequency and the critical wind speed.

6.3.1 Critical Flutter Condition

The solution of the flutter condition is shown in Figure 6.3. Table 6.2 shows the critical wind speed of the bridge, using the synthesized aerodynamic coefficients and the Golden Gate Bridge coefficients.

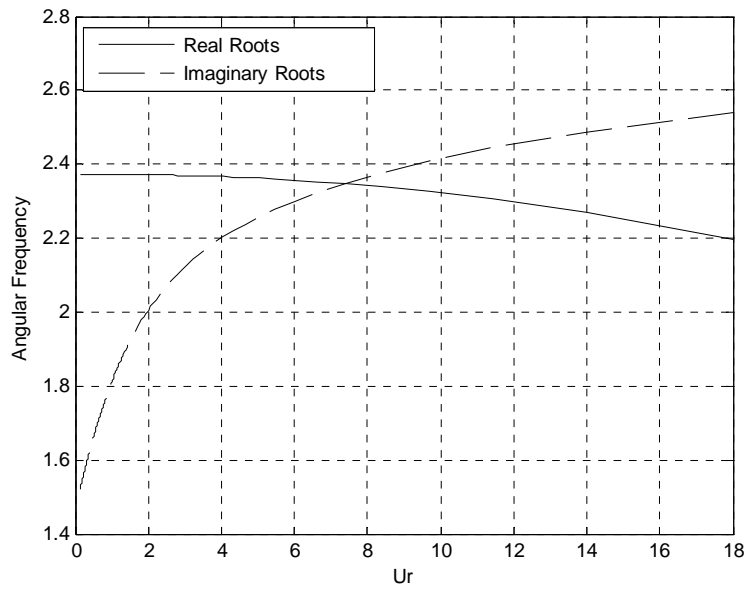


Figure 6.3: Synthesized flutter derivatives

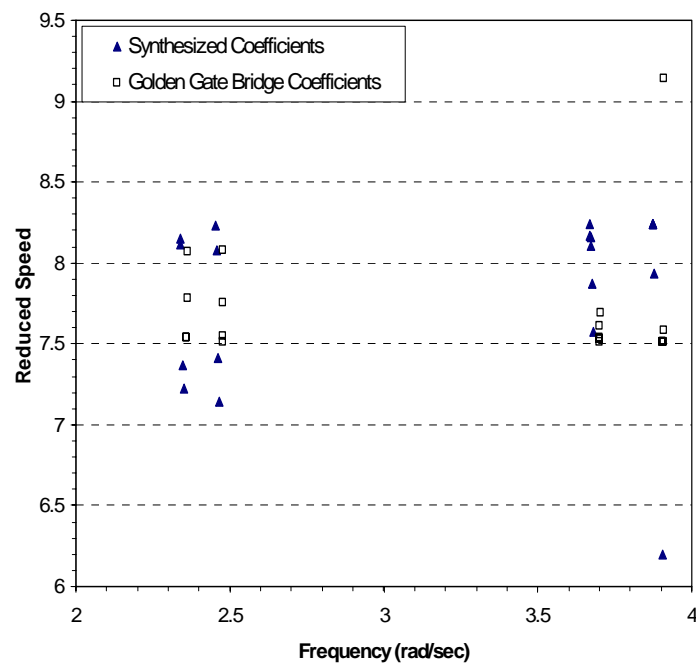


Figure 6.4: Critical Frequencies versus critical reduced wind speed

Table 6.2: Flutter analysis of the Second Tacoma Narrows Bridge

Set No.	Mode i	Mode j	Synthesized Flutter Derivatives			Golden Gate Flutter Derivatives		
			Critical Frequency	Ur	Critical speed m/s	Critical Frequency	Ur	Critical speed m/s
1	2	8	2.348	7.3696	50.365	2.3615	7.7778	53.46
2	2	9	2.4627	7.4155	53.154	2.4774	7.754	55.913
3	2	12	3.6703	8.1684	87.262	3.701	7.5292	81.106
4	2	13	3.874	8.2438	92.955	3.9072	7.5151	85.465
5	3	8	2.3411	8.1147	55.294	2.3601	7.5404	51.798
6	3	9	2.4565	8.0753	57.738	2.4761	7.5485	54.402
7	3	12	3.6787	7.5763	81.122	3.7025	7.689	82.861
8	3	13	3.8741	8.2404	92.919	3.9072	7.5157	85.472
9	5	8	2.3407	8.1523	55.541	2.3601	7.535	51.761
10	5	9	2.455	8.231	58.815	2.476	7.515	54.158
11	5	12	3.6694	8.2406	88.012	3.7008	7.5147	80.946
12	5	13	3.8741	8.2372	92.883	3.9072	7.5154	85.468
13	6	8	2.3496	7.2216	49.387	2.3614	8.0721	55.481
14	6	9	2.4656	7.1463	51.285	2.477	8.0818	58.267
15	6	12	3.6712	8.1097	86.656	3.701	7.5416	81.24
16	6	13	3.874	8.2436	92.953	3.9073	7.513	85.443
17	10	12	3.6746	7.8709	84.182	3.7015	7.6086	81.973
18	10	13	3.8787	7.9314	89.541	3.9079	7.584	86.264
19	11	12	3.6708	8.1593	87.177	3.701	7.527	81.083
20	11	13	3.9068	6.2016	70.52	3.911	9.1409	104.06

6.4 Discussion

Table 6.2 shows that using the synthesized derivatives the critical wind speed is found to be 49.387 m/s (110.48 mph), and using the golden gate aerodynamic derivatives it is found to be 51.761 (115.789 mph), which is around 5% higher. The closeness in the results between the two sets of flutter coefficients verifies the assumptions of the synthesized coefficients holding the average trend of aerodynamic coefficients of open-truss stiffened decks. Note that the coupling of modes corresponding to the estimated critical wind speed does not match the expected coupling of modes based on $C_{\alpha}C_{\xi}$, as

described in Chapter 3, where Set No. one is considered to be the most critical mode. The critical wind speed estimated when modes 2 and 9 are coupled is 50.365 m/s. This value is only 2% higher than the minimum speed obtained.

Figure 6.4 shows that the solution of the flutter condition lineup in four columns with approximate frequencies of 2.35, 2.46, 3.7 and 3.9 Hz. These frequencies are close to but less than the corresponding torsional frequencies used in the analysis which are for modes 20, 21, 37 and 41. This implies that the vertical mode has less significance on the response than the torsional mode. The critical case is that point located closest to the left-bottom corner of the plot.

Note that although the critical wind speeds of both analyses are found to be close, the coupled vertical and torsional modes are different in each case. For the synthesized coefficients coupling of modes 6 and 8, which is set 13, produced the critical condition, while with the Golden Gate Bridge coefficients coupling of modes 5 and 8, which is set 9, invoked the flutter condition. This result further verifies the appropriateness of assumed coefficients as the two vertical modes are consecutive and have close frequencies.

Hence using synthesized aerodynamic coefficients yields reasonable estimation of critical speed. However, the coupling of modes at flutter remains uncertain. Moreover, using different sets of aerodynamic derivative of plate-like deck gave close estimation to the critical wind speed. This implies that the effect of the aerodynamic derivatives is very small compared to contribution of the mechanical properties of the structure.

The maximum wind speed estimated in the Tacoma Narrows area is 105.9 mph, as discussed in Chapter 4 as compared to 110.48 estimated here. Therefore according to this analysis the bridge is safe, since the estimated flutter speed is around 4% higher than the maximum expected wind speed.

CHAPTER 7

CONCLUSIONS AND RECOMMENDATIONS

The Second Tacoma Narrows Bridge frequencies have been successfully and accurately estimated. The analytical results show sound agreement with the experimental data. The transverse and the vertical frequencies are almost equal to the values obtained by the ambient testing. However longitudinal frequencies do not show an accurate agreement with the experimental results. The results are close to the experimental frequencies.

The suggested modelling technique helped in concluding such results. Modelling of suspension bridges requires using centenary element formulation. A non-linear truss element is not quite acceptable to model cables. Detailed modelling of the superstructure is also recommended. Moreover, the Ritz method was very successful in estimating the structural frequencies and eliminating the local mode shapes.

The frequencies associated with the longitudinal mode shapes, however, do not show high accuracy compared with the ambient study. However, this does not have a significant effect on the aerodynamic analysis; that is because of the fact that the longitudinal frequencies will not be excited by wind forces. Moreover, the torsional and the vertical modes are not coupled with the longitudinal mode.

Flutter coefficients of open-truss stiffened superstructures are successfully synthesized based on the Theodorsen function. It is found that reversing the sign of the

torsional aerodynamic damping coefficient of the flat plate simulates the average value of this type of superstructures. This conclusion is not applicable for streamlined decks or superstructures susceptible to vortex induced motion, such as, H-shape decks.

Recommendations

According to the proposed procedure of synthesizing the flutter derivatives and the methods used to find the critical wind speed of stiffened truss decks closing the open-grates of the Second Tacoma Narrows Bridge will not cause the bridge to reach the critical flutter condition. However, keeping the side grates opened ensures the safety of the bridge in severe wind conditions, Matsumoto et al (2001).

The research on using computational-fluid-dynamics and fluid-structure-interaction procedures in the flutter analysis of long-span bridges is still a novel field of study. Some computational-fluid-dynamics software packages and numerical procedures are still under development and investigation. The reliability of obtaining a valid solution depends mainly on the capabilities of the used software. The solution of the FSI problem may exhibit rational response, but may also involve inaccurate numerical values. For a more reliable analysis, it is recommend utilizing powerful computational resources with multi-processing capabilities and three-dimensional models, rather than a simplified two dimensional characterization. Future research may also consider applying turbulence models to account for the variable component of flow velocity

APPENDIX A

ANALYSIS RESULTS

A.1 Second Tacoma Narrows Bridge Frequency Analysis

Mode No	Frequency (rad/sec)	Frequency (cycle/sec)	Period (sec)
1	0.4462	0.0710	14.0804
2	0.9081	0.1445	6.9193
3	0.9832	0.1565	6.3906
4	1.1672	0.1858	5.3831
5	1.3012	0.2071	4.8289
6	1.5073	0.2399	4.1686
7	1.5648	0.2490	4.0155
8	1.5988	0.2545	3.9300
9	1.8497	0.2944	3.3969
10	1.9034	0.3029	3.3010
11	1.9048	0.3032	3.2985
12	1.9052	0.3032	3.2979
13	1.9068	0.3035	3.2952
14	2.0315	0.3233	3.0929
15	2.0410	0.3248	3.0784
16	2.0913	0.3328	3.0045
17	2.1368	0.3401	2.9404
18	2.1479	0.3418	2.9253
19	2.1870	0.3481	2.8730
20	2.3729	0.3777	2.6479
21	2.4895	0.3962	2.5239
22	2.5209	0.4012	2.4925
23	2.6453	0.4210	2.3752
24	2.6681	0.4246	2.3549
25	2.6763	0.4259	2.3477
26	2.6847	0.4273	2.3404
27	2.9379	0.4676	2.1387
28	3.0175	0.4803	2.0823
29	3.0308	0.4824	2.0731
30	3.0338	0.4828	2.0711
31	3.1165	0.4960	2.0161
32	3.1500	0.5013	1.9946
33	3.3631	0.5353	1.8683
34	3.3785	0.5377	1.8598
35	3.4433	0.5480	1.8247
36	3.6043	0.5736	1.7432
37	3.7210	0.5922	1.6886
38	3.7792	0.6015	1.6626
39	3.8121	0.6067	1.6482
40	3.8671	0.6155	1.6248

Mode No	Frequency (rad/sec)	Frequency (cycle/sec)	Period (sec)
51	4.5488	0.7240	1.3813
52	4.6111	0.7339	1.3626
53	4.6783	0.7446	1.3430
54	4.7142	0.7503	1.3328
55	4.7865	0.7618	1.3127
56	4.8180	0.7668	1.3041
57	4.9101	0.7815	1.2796
58	5.0463	0.8031	1.2451
59	5.1340	0.8171	1.2239
60	5.2249	0.8316	1.2026
61	5.3256	0.8476	1.1798
62	5.3535	0.8520	1.1737
63	5.3751	0.8555	1.1690
64	5.7356	0.9128	1.0955
65	5.7517	0.9154	1.0924
66	5.8874	0.9370	1.0672
67	6.0325	0.9601	1.0416
68	6.2647	0.9971	1.0030
69	6.3285	1.0072	0.9928
70	6.5879	1.0485	0.9538
71	7.0892	1.1283	0.8863
72	7.1514	1.1382	0.8786
73	7.1681	1.1408	0.8766
74	7.5785	1.2062	0.8291
75	7.9893	1.2715	0.7865
76	8.1640	1.2993	0.7696
77	8.5155	1.3553	0.7379
78	8.9955	1.4317	0.6985
79	9.2453	1.4714	0.6796
80	9.3795	1.4928	0.6699
81	10.4664	1.6658	0.6003
82	10.7922	1.7176	0.5822
83	11.4814	1.8273	0.5472
84	11.8388	1.8842	0.5307
85	12.8915	2.0517	0.4874
86	13.9077	2.2135	0.4518
87	14.5303	2.3126	0.4324
88	15.8278	2.5191	0.3970
89	16.3625	2.6042	0.3840
90	18.7194	2.9793	0.3357

41	3.9286	0.6253	1.5993
42	3.9916	0.6353	1.5741
43	4.0022	0.6370	1.5699
44	4.0450	0.6438	1.5533
45	4.0913	0.6511	1.5358
46	4.1292	0.6572	1.5216
47	4.3491	0.6922	1.4447
48	4.4390	0.7065	1.4155
49	4.5064	0.7172	1.3943
50	4.5150	0.7186	1.3916

91	20.1433	3.2059	0.3119
92	22.8403	3.6352	0.2751
93	25.1582	4.0040	0.2497
94	28.7127	4.5698	0.2188
95	33.6017	5.3479	0.1870
96	39.9175	6.3531	0.1574
97	52.0059	8.2770	0.1208
98	70.6210	11.2397	0.0890
99	105.1965	16.7425	0.0597
100	379.7931	60.4459	0.0165

Modal Participation Masses (%)

Mode	TRAN-X	TRAN-Y	TRAN-Z
	MASS	MASS	MASS
1	0	23.68	0
2	0	0	3.23
3	0.01	0	0
4	0	0.01	0
5	3.04	0	0
6	0	15.12	0
7	0	0	2.42
8	0	9.64	0
9	0	0	0
10	0	0	0
11	0	0	0
12	0	1.99	0
13	0	0	0
14	0	0	0
15	0.02	0	37
16	0	0	0
17	0	0	0
18	0	0.37	0
19	0	0.03	0
20	0	3.05	0
21	0	3.07	0
22	1.31	0	0
23	0	0.04	0
24	0	0	0
25	0.12	0	4.29
26	0	0.03	0
27	0	0.08	0
28	0	0	0
29	0	1.86	0
30	0	0	0
31	0	0.01	0
32	0	0	0
33	46.1	0	0.06
34	0.03	0.89	0

Mode	TRAN-X	TRAN-Y	TRAN-Z
	MASS	MASS	MASS
51	0	0.2	0
52	0	0.08	0
53	0	0.06	0
54	0.12	0	0.03
55	0	0.03	0
56	0.89	0	0
57	0	3.34	0
58	0.05	0.67	0
59	1.96	0	0
60	0	0	0.01
61	0	0	0.02
62	0	0	0.01
63	0	0	0.01
64	0.16	0.01	0
65	1.44	0	0
66	0.67	0	0.04
67	0	0.13	0
68	0	0	0
69	0.05	0	1.38
70	0	0.03	0
71	0.83	0	0.68
72	0.06	0.01	1.67
73	2.41	0.04	0.19
74	0.37	0	0
75	0	0	0.08
76	0.06	0	0.15
77	0.65	0.19	0
78	0.1	0	0.52
79	3.21	0.02	0.01
80	0.05	0.02	0
81	0.56	0	0.05
82	0	0.01	0.01
83	0.33	0.04	0.02
84	0.01	0	0.45

35	0	0	0
36	0.9	0	2.42
37	0	0.02	0
38	0.26	0	0.28
39	5.9	0	0
40	0	0.94	0
41	0	0.02	0
42	0	0	0
43	0	0	0
44	0	1.67	0
45	0	0	0
46	0	0.07	0
47	0	0	0
48	0	0.68	0
49	0	0	0
50	0	0	1.02

85	0.01	0.01	0.06
86	0	0	1.08
87	0	0	0.75
88	0	0.01	1
89	0	0	6.64
90	0.02	0.01	0.5
91	0.11	0.02	0.22
92	0	0	5.46
93	0.07	0.01	0.51
94	0.09	0.01	0.84
95	0.05	0.01	1.16
96	0.24	0.09	0.61
97	0	0	9
98	0	0.01	1.12
99	0	0	13.95
100	0	0	0.69

Mode Shape Identification

Mode	Freq. (rad/sec)	Shape	Location
1	0.446236	L_HS	MS
2	0.908061	V_HS	MS
3	0.983197	V_FS	MS
4	1.167195	L_FS	MS
5	1.301158	V_FS	SS
6	1.50725	L_HS	SS
7	1.564752	V_(FS+HS)	MS
8	1.598782	L_HS	SS
9	1.849657	L_HS	SC
10	1.9034	L_HS	SC
11	1.904833	L_HS	MC
12	1.905209	L_FS	MC+TW
13	1.906756	L_FS	MC+MS
14	2.031485	L_FS	SC+MC
15	2.04103	V_2HS	MS+SS
16	2.091287	L_HS	SC
17	2.136832	L_2HS	C+S
18	2.147853	L_HS	SC
19	2.186997	L_FS	C+S
20	2.372891	T_HS	S
21	2.489505	L+T_HS	S
22	2.520852	V_2FS	MS
23	2.645296	L_FS	SC
24	2.668146	L_2HS	SC
25	2.676282	V_HS	SC
26	2.684675	V_HS	SC

Mode #	Freq. (rad/sec)	Shape	Location
27	2.937856	L_2FS	C
28	3.017497	L_4HS	MC
29	3.030805	L_2FS	C
30	3.033756	L	C
31	3.116474	L	C
32	3.15004	L	SC
33	3.36308	V_3FS	S
34	3.378495	L	SC
35	3.443337	L	SC
36	3.604311	V_(2FS+HS)	MS
37	3.721043	L+T_FS	MS
38	3.779155	V_(2FS+HS)	SS+MS
39	3.812122	V_FS	SS
40	3.867088	L	C
41	3.928639	T_FS	MS
42	3.991616	L	SC
43	4.002207	L	MC
44	4.045034	L	C
45	4.091282	L	C
46	4.129206	L_2FS	C+MS
47	4.349058	T_HS	SS
48	4.438963	T_HS	SS
49	4.506398	V	SS
50	4.515044	V	SS
52	4.61109	T_HS	SS

Symbol Key	
L	Lateral Mode
V	Vertical Mode
T	Torsional Mode
HS	Half Sinusoidal
FS	Full Sinusoidal
MS	Mid Span
SS	Side Span
SC	Side Span Cable
MC	Mid Span Cable
TW	Tower
C	All Cables
S	All Span

APPENDIX B

MATLAB PROGRAMS

B.1 Coupling Coefficient

```
%FindGenProp
% Find the Generalized Properties and Coupling Terms

mMat=[2 8;3 8;5 8;6 8;
       2 9;3 9;5 9;6 9;
       10 12;11 12;10 13;11 13]

for m=1:12
    mod1=mMat(m,1);
    mod2=mMat(m,2);
    [nr,nc]=size(Modeshp);

    Cx12=0;Cx11=0;Cx22=0;
    for i=1:nr-1;
        Cx1=(Modeshp(i,modXi+1)+Modeshp(i+1,modXi+1))/2;
        Cx2=(Modeshp(i,modA+1)+Modeshp(i+1,modA+1))/2;
        Cx12=Cx12+Cx1*Cx2*Modeshp(i,1);
        Cx11=Cx11+Cx1*Cx1*Modeshp(i,1);
        Cx22=Cx22+Cx2*Cx2*Modeshp(i,1);
    end
    CXi=abs(Cx12/Cx11);
    CA=abs(Cx12/Cx22);
    CouplingResult(m,:)=[mod1,mod2,CXi,CA]
end
```

B.2 Flutter Analysis MATLAB Program

```
% Uncoupled Flutter Solver
clear
clc
stp=0;
%ModesDataBase_FlatPlate
% Xi index is for heaving, A index is for Rotation

BrdgWidth=27.5; %meter
AirDensity=1.2;

OmegaXi=0.1285*2*pi;
OmegaXi=0.1638*2*pi;
OmegaA=0.1916*2*pi;

ZetaA=0.005; % Damping ratio
ZetaXi=0.005;

CXi=.34;
CA=.32;

EffMassXi=5.2081e+003;
```

```

EffMassA=3680000;

GamaW=OmegaA/OmegaXi;
GamaM=EffMassXi/(AirDensity*BrdgWidth^2);
GamaI=EffMassA/(AirDensity*BrdgWidth^4);
CA=1.29;
CXi=0.38;

% Note: the generalized mass is calculated based on certain
mode(dominated
% mode) see GetGs.m
for K=pi/4:.1:50
    stp=stp+1
    k=K/2; % half cord
    Ur=pi/k %Reduced Velocity
    % GetFlutterDeriv_FlatPlate;
    GGGetHsAs;
    % GGGetGs;

    R1=0;
    R2=-GamaW^2-4*ZetaA*ZetaXi*GamaW-1-A3/(2*GamaI)-
GamaW^2*H4/(2*GamaM);
    R3=ZetaA*GamaW*H1/GamaM+ZetaXi*A2/GamaI;
    R4=1+H4/(2*GamaM)+A3/(2*GamaI)+(CXi*CA*A1*H2-A2*H1+H4*A3-
CXi*CA*A4*H3)/(4*GamaM*GamaI);
    Rconst=GamaW^2;

    I1=-GamaW^2*H1/(2*GamaM)-A2/(2*GamaI);
    I2=-2*ZetaA*GamaW-2*ZetaXi-ZetaA*GamaW*H4/GamaM-ZetaXi*A3/GamaI;
    I3=H1/(2*GamaM)+A2/(2*GamaI)+(H4*A2+H1*A3-CXi*CA*H3*A1-
CXi*CA*H2*A4)/(4*GamaM*GamaI);
    Iconst=2*ZetaXi*GamaW^2+2*ZetaA*GamaW;
    %Get A and B matrix then E matrix
    RealRoot=roots([R4 R3 R2 R1 Rconst]);
    ImgRoot=roots([I3 I2 I1 Iconst]);

    RealRoot=sortrows(RealRoot);
    ImgRoot=sortrows(ImgRoot);

    PlotSolReal(stp,:)=RealRoot(:,1)*OmegaXi;
    PlotSolImag(stp,:)=ImgRoot(:,1)*OmegaXi;
    PlotUr(stp,1)=Ur;
end

plot(PlotUr(:,1),PlotSolReal(:,4))
Hold on
plot(PlotUr(:,1),PlotSolImag(:,3),'--')
Grid on
legend('Real Roots','Imaginary Roots','sin(x-.5)')
xlabel('Ur');ylabel('Angular Frequency');
Hold off

Status = 'End of the Analysis'

%GGGetHsAs
As=[0 0 0 0 0

```

7.05E-01	-4.77E-02	-2.88E-03	2.26E-02	-8.21E-02
8.38E-01	-1.29E-02	-1.69E-02	7.49E-03	-8.19E-03
1.10E+00	-6.33E-02	-7.88E-03	1.84E-02	-6.08E-02
1.39E+00	-1.89E-01	-4.17E-02	1.20E-02	-5.60E-02
1.82E+00	-2.04E-01	-1.26E-01	1.20E-01	5.55E-02
2.21E+00	-2.59E-01	-1.08E-01	1.97E-01	1.15E-01
2.51E+00	-2.15E-01	-6.57E-02	2.67E-01	1.66E-01
2.81E+00	-2.84E-01	-4.60E-02	3.17E-01	1.75E-01
3.27E+00	-1.95E-01	3.29E-03	3.85E-01	3.27E-01
3.88E+00	-1.43E-01	6.97E-02	4.29E-01	2.74E-01
4.24E+00	-2.40E-01	1.20E-01	4.55E-01	3.06E-01
4.79E+00	-2.40E-01	1.90E-01	5.13E-01	3.59E-01
5.25E+00	-1.41E-01	2.70E-01	5.67E-01	2.70E-01
6.31E+00	-3.98E-02	4.59E-01	6.77E-01	3.21E-01
7.33E+00	5.64E-02	5.89E-01	6.70E-01	2.62E-01
8.16E+00	1.16E-01	7.30E-01	6.93E-01	4.25E-01
9.04E+00	4.73E-02	8.16E-01	7.33E-01	2.23E-01];

```

Hs=[0 0 0 0 0
6.94E-01 -7.26E-02 2.49E-01 1.42E+00 1.41E-01
8.39E-01 -3.73E-01 2.25E-01 1.54E+00 -9.63E-02
1.09E+00 -4.52E-01 2.26E-01 1.76E+00 1.10E-02
1.39E+00 -4.15E-01 3.81E-01 1.85E+00 -2.68E-01
1.82E+00 -1.30E+00 5.92E-01 1.76E+00 -4.97E-01
2.21E+00 -1.69E+00 5.13E-01 1.96E+00 -7.52E-01
2.51E+00 -2.06E+00 3.29E-01 2.07E+00 -7.60E-01
2.82E+00 -2.53E+00 2.93E-01 2.17E+00 -9.37E-01
3.28E+00 -3.28E+00 2.78E-01 2.60E+00 -5.30E-01
3.88E+00 -3.32E+00 1.43E-01 3.06E+00 -4.91E-02
4.24E+00 -3.53E+00 1.66E-01 4.16E+00 4.54E-01
4.79E+00 -4.40E+00 -6.80E-02 5.33E+00 4.85E-01
5.25E+00 -4.38E+00 3.11E-01 6.72E+00 4.52E-01
6.32E+00 -4.80E+00 9.51E-01 9.90E+00 1.09E+00
7.34E+00 -5.55E+00 1.51E+00 1.30E+01 7.86E-01
8.16E+00 -6.13E+00 1.78E+00 1.46E+01 1.01E+00
9.03E+00 -6.73E+00 2.24E+00 1.68E+01 2.24E+00];
endloopHs=0;
endloopAs=0;

```

```

for i=1:18
    if (Ur>=As(i,1))& ((Ur<=As(i+1,1)))&(endloopAs == 0)
        c=2;
        A1=(Ur-As(i,1))/(As(i+1,1)-As(i,1))*(As(i+1,c)-
As(i,c))+As(i,c);
        c=3;
        A2=(Ur-As(i,1))/(As(i+1,1)-As(i,1))*(As(i+1,c)-
As(i,c))+As(i,c);
        c=4;
        A3=(Ur-As(i,1))/(As(i+1,1)-As(i,1))*(As(i+1,c)-
As(i,c))+As(i,c);
        c=5;
        A4=(Ur-As(i,1))/(As(i+1,1)-As(i,1))*(As(i+1,c)-
As(i,c))+As(i,c);
        endloopAs=1;
    end
    if (Ur>=Hs(i,1))& ((Ur<=Hs(i+1,1)))&(endloopHs == 0)
        c=2;

```

```

        H1=(Ur-Hs(i,1))/(Hs(i+1,1)-Hs(i,1))*(Hs(i+1,c)-
Hs(i,c))+Hs(i,c);
        c=3;
        H2=(Ur-Hs(i,1))/(Hs(i+1,1)-Hs(i,1))*(Hs(i+1,c)-
Hs(i,c))+Hs(i,c);
        c=4;
        H3=(Ur-Hs(i,1))/(Hs(i+1,1)-Hs(i,1))*(Hs(i+1,c)-
Hs(i,c))+Hs(i,c);
        c=5;
        H4=(Ur-Hs(i,1))/(Hs(i+1,1)-Hs(i,1))*(Hs(i+1,c)-
Hs(i,c))+Hs(i,c);
        endloopHs=1;
    end
end

```

APPENDIX C

C.1 Calculation of Side-Span Profile

The figure shows a schematic sketch for the side-span cable profile. There points are known on the profile, and none of them are necessarily at the vertex. The following is the procedure taken to find the polynomial function (aX^2+bX+c) of the profile, assuming that the coordinate system is at one of the given points. The axes are then transformed to vertex and the final profile equation is found

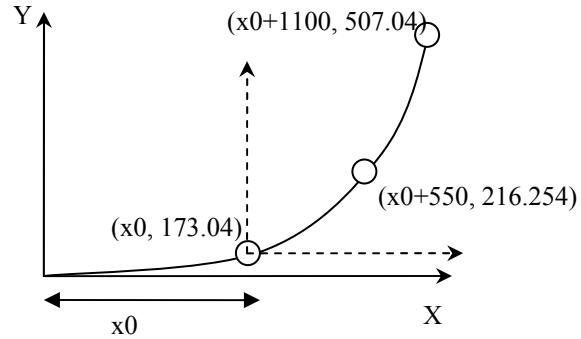
1.4 Find the profile with respect to point 1 ($x_0, 173.04$)

$$V_{mat} := \begin{pmatrix} 0 & 0 & 1 \\ 550^2 & 550 & 1 \\ 1100^2 & 1100 & 1 \end{pmatrix}, \quad Y_{vect} := \begin{pmatrix} 173.04 \\ 296.826 \\ 507.04 \end{pmatrix}$$

Solve for the polynomial coefficients

$$Coeff := V_{mat}^{-1} \cdot Y_{vect}$$

$$Coeff \rightarrow \begin{pmatrix} .14285619834710743801e-3 \\ .146494545454545457 \\ 173.04 \end{pmatrix}$$



Then the vertex of the polynomial is at x

Shift x-axis

$$x_0 := \frac{-Coeff_1}{2 \cdot Coeff_0} \quad x_0 \rightarrow -512.73429906974591578$$

$$y := Coeff_0 \cdot (x + x_0)^2 + Coeff_1 \cdot (x + x_0) + Coeff_2$$

$$y \text{ simplify} \rightarrow .14285619834710743801e-3x^2 + .13767288638859384044e-20x + 135.4836109594113018$$

Shift y-axis

$$y := y - 135.4836109594113018$$

Therefore the side-span cable profile is expressed as follows,

$$y := .14285619834710743801e-3x^2$$

Which equal to that of the main-span

C.2 Derivation of Equations 5.19 coefficients

Mathcad is used to find the complex polynomial of the coefficient matrix of the flutter condition equation. The real and imaginary coefficients are then separated.

$$X := \begin{bmatrix} \left[-\Omega^2 + 2 \cdot i \cdot \zeta_h \cdot \Omega + 1 - \frac{\Omega^2}{2 \cdot \gamma_m} \cdot (H4 + i \cdot H1) \right] & \frac{-Ch \cdot \Omega^2}{2 \cdot \gamma_m} \cdot (H3 + i \cdot H2) \\ \frac{-Ca \cdot \Omega^2}{2 \cdot \gamma_l} \cdot (A4 + i \cdot A1) & \left[-\Omega^2 + 2 \cdot i \cdot \zeta_a \cdot \gamma_w \cdot \Omega + \gamma_w^2 - \frac{\Omega^2}{2 \cdot \gamma_l} \cdot (A3 + i \cdot A2) \right] \end{bmatrix}$$

$$DX := |X|$$

$$DX \text{ coeffs, } \Omega \rightarrow \begin{bmatrix} \gamma_w^2 \\ 2 \cdot i \cdot \zeta_a \cdot \gamma_w + 2 \cdot i \cdot \zeta_h \cdot \gamma_w^2 \\ \frac{-1}{2 \cdot \gamma_l} \cdot A3 - 1 - \gamma_w^2 - \frac{1}{2 \cdot \gamma_m} \cdot H4 \cdot \gamma_w^2 - \frac{1}{2} \cdot \frac{i}{\gamma_l} \cdot A2 - \frac{1}{2} \cdot \frac{i}{\gamma_m} \cdot H1 \cdot \gamma_w^2 - 4 \cdot \zeta_h \cdot \zeta_a \cdot \gamma_w \\ (-2) \cdot i \cdot \zeta_h - \frac{i}{\gamma_l} \cdot \zeta_h \cdot A3 - 2 \cdot i \cdot \zeta_a \cdot \gamma_w - \frac{i}{\gamma_m} \cdot H4 \cdot \zeta_a \cdot \gamma_w + \frac{1}{\gamma_m} \cdot H1 \cdot \zeta_a \cdot \gamma_w + \frac{1}{\gamma_l} \cdot \zeta_h \cdot A2 \\ \frac{1}{2 \cdot \gamma_m} \cdot H4 + \frac{1}{2 \cdot \gamma_l} \cdot A3 + \frac{1}{2} \cdot \frac{i}{\gamma_l} \cdot A2 - \frac{1}{4} \cdot \frac{i}{\gamma_m \cdot \gamma_l} \cdot Ch \cdot Ca \cdot H2 \cdot A4 - \frac{1}{4 \cdot \gamma_m \cdot \gamma_l} \cdot Ch \cdot Ca \cdot H3 \cdot A4 + \frac{1}{4 \cdot \gamma_m \cdot \gamma_l} \cdot Ch \cdot Ca \cdot H2 \cdot A1 + \frac{1}{2} \cdot \frac{i}{\gamma_m} \cdot H1 + \frac{1}{4 \cdot \gamma_m \cdot \gamma_l} \cdot H4 \cdot A3 - \frac{1}{4 \cdot \gamma_m \cdot \gamma_l} \cdot H1 \cdot A2 + \frac{1}{4} \cdot \frac{i}{\gamma_m \cdot \gamma_l} \cdot H1 \cdot A3 - \frac{1}{4} \cdot \frac{i}{\gamma_m \cdot \gamma_l} \cdot Ch \cdot Ca \cdot H3 \cdot A1 + \frac{1}{4} \cdot \frac{i}{\gamma_m \cdot \gamma_l} \cdot H4 \cdot A2 + 1 \end{bmatrix}$$

APPENDIX D

MISCELLANIES CALCULATIONS

D.1 Calculations of the Grate Opening Ratio of Tacoma Narrows Bridge:

The following calculation estimates the opening ratio (OR) of the grates of the Second Tacoma Narrows Bridge.

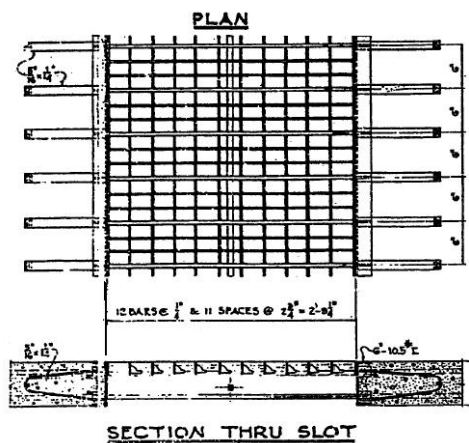


Figure D.1: The Second Tacoma Narrows Bridge Grates

$$\text{OR} = \frac{\text{SolidArea}}{\text{TotalArea}}$$

$$\text{OR} = \frac{12\text{bar} \times 0.25" \text{ diameter} \times 0.5' \text{ Length} + 4\text{bars} \times 0.25" \times 2.7708' \text{ Length}}{(2.77083' \times 6'')} \times 100\%$$

$$\text{OR} = 25.6\%$$

APPENDIX E

PARAMETERS FOR AEROELASTICITY

E.1 Wind Characteristics

In aerodynamic analysis the wind parameters are calculated based on spatial considerations. The environment surrounding the structure has considerable effects on the *atmospheric boundary layer*. Wind flow becomes turbulent and nonlinear with space and time. This is due to several factors, such as friction with the terrain, temperature variations between the air at terrain level and that of higher altitudes, and the difference in pressure from one zone to another.

Wind boundary layer is described by exponential profile of the mean wind speed and a variable component of the turbulent speed. There is no clear formulation to simulate the turbulent component of wind speed and stochastic method based on *random functions* which are used to generate this component analytically.

For certain regions the average temperature, pressure and surface roughness are used to generate the shape of the boundary layer. This is important for slender vertical structures such as high-raised buildings and towers. In suspension bridges, however, averaged values at the elevation of the superstructure are sufficiently acceptable to calculate wind characteristics, unless wind effects on the main towers is required.

Averaged wind parameters are calculated in the following section. Most of these parameters, such as viscosity and density of air, are required for the fluid-structure-interaction finite element analysis. For the classical flutter analysis, density of air is the

only wind variable required, and the interaction between the structure and the laminar wind flow is depicted by other coefficients determined experimentally, as described in Chapter 6.

Another important wind parameter is the maximum averaged expected wind speed for a given number year return period at the structure site. This value is extracted using statistical methods, where the collected wind data is fitted to a cumulative density function. The wind speed corresponding to a certain probability of occurrence is then can be obtained.

The following is a brief discussion for the wind parameters and the methods used to numerically evaluate them for a given the bridge.

E.1.1 Estimating Wind Parameters

The number of air molecules in a micrometer is 2.5×10^{10} molecules, at sea level and standard temperature. In other words, the mean free path between molecules is 6.6×10^{-8} meter. Therefore, wind within the atmospheric layer is considered continuum (Bertin, 2002). This allows the gross behavior of air motion to be described using macroscopic properties, such as density, viscosity and temperature.

Generally speaking, fluid is described by the following variables, namely, density, viscosity, specific heat at constant pressure, specific heat at constant volume, thermal

conductivity, rate of heat generated per unit volume, thermal expansion coefficient and bulk modulus of elasticity. However, in incompressible flows, with inconsiderable heat transfer, all the above mentioned parameters are ignored, except density and viscosity. Bulk modulus of elasticity is assumed very large, and specific heat at constant volume is assumed to be equal to the specific heat at constant pressure.

The mentioned variables could be constants, time-dependent, temperature-dependent, deformation-dependent or a combination of these conditions. Although the constant material model is the simplest, it is the most applicable in civil engineering problems. Wind properties within few hundred feet above the ground could be considered constant. According to the U.S. Standard Atmosphere, 1976, the change in air density, between the ground surface and that at 2000 ft elevation above the ground level is less than 5% when the change in viscosity is less than 3% and the change in pressure is less than 8%, *see Bertin J, 2002*.

Air properties could be measured in several units based on the different unit systems. However, in computational fluid dynamics standard units are used, due to its standard definition. Temperature, in fluid mechanics, is usually measured in Kelvin (K), rather than Celsius or Fahrenheit. Kelvin is more appropriate temperature unit than the others since it is derived based on molecular motion. Air pressure is traditionally measured using standard atmospheric pressure units, which is based on mercury column length. However, in computational fluid dynamics it is more appropriate to use the force per unit area unit. The standard atmospheric pressure at sea level is $1.01325 \times 10^5 \text{ N/m}^2$.

Density of air does not have a unique value. Air continuum changes with respect to temperature and pressure. Therefore the mass per unit volume is a function of pressure and temperature. The *equation of state* of thermally perfect gases could be used to express the density of air as given by:

$$\rho = \frac{p}{RT} \quad \text{E.1}$$

Where p is the pressure (N/m^2), R is the gas constant, which is equal to 287.05 N.m/kg.K in SI units, and T is the temperature in (K). Note that in fluid-structure-interaction analysis, pressure around the solid body changes due the motion of the solid body. However, the change in pressure between two points in the fluid flow is negligible compared to the absolute pressure value. Bertin J., 2002, suggests that the assumption of constant density is a valid approximation for velocities below 100 m/s (223 mph), which is higher than the maximum possible wind speed on structures.

Viscosity is measured by coefficient of, μ , which is the ratio of the shear stress developed by the flow to the transverse gradient of velocity. Viscosity represents the transport of momentum in the direction of the velocity gradient. All fluids have viscosity, but not all flows are viscous.

For temperatures less than 3000 K, the coefficient of viscosity of air is independent of pressures (see Svehla 1962), and could be related to temperature only, using Sutherland's equation:

$$\mu = 1.458 \times 10^{-6} \frac{T^{1.5}}{T + 110.4} \quad \text{E.2}$$

where T is the temperature in Kelvin and μ is the coefficient of viscosity (kg/s.m).

The ratio of the viscosity to the density is defined as the *kinematic viscosity*, ν , which is measured in square meter per second is given by:

$$\nu = \frac{\mu}{\rho} \quad \text{E.3}$$

The thermal conductivity of air is frequently used in turbulent flow models. It could be expressed in terms of temperature as follows:

$$k = 4.76 \times 10^{-4} \frac{T^{1.5}}{T + 112} \quad \text{E.4}$$

where k is in cal/m.s.K, and T is the temperature in Kelvin. The conductivity is also computed in J/m.s.K, where 1 cal is 4.187 J (Bertin, 2002).

Another property of air is the speed of sound, which reflects the disturbance of infinitesimal proportions propagating through fluid at rest. Generally, the speed of sound, a , is given:

$$a = \sqrt{\gamma RT}$$

E.5

where γ is the ratio of specific heats ($C_p/C_v = 1.4$ for perfect gas), R is the gas constant and T is the temperature. Therefore for air the speed of sound (m/s) is $a = 20.047\sqrt{T}$, where T is in Kelvin. For a standard temperature the speed of sound is around (346.1 m/s). It is suggested that air flow could be considered incompressible if its speed is less than 0.3 Mach (103 m/s or 230 mph), *see Wanderley and Levi, 2002*.

Wind properties, as shown in the above equations, are mainly a function of temperature and pressure. These two variables are not deterministic and are considered stochastic variables. However, ignoring the variability in wind properties is accepted in this research, since the extreme values of wind speed are required and the critical flutter condition is to be evaluated, rather than a reliability assessment. Moreover, the variation in wind properties between 37 °F and 100 °F is around 20%. If the mean value of this temperature interval is considered then the variation would be around $\pm 10\%$. Therefore, temperature and pressure will be assumed constants and air density and viscosity will be estimated accordingly as deterministic value. The pressure and temperature are assumed based on the average metrological measurements in the Tacoma area in months of maximum wind speed.

The following table summarizes average values of air properties that will be used for analysis in this research.

Table E.1: Air parameters				
T	20	°C	68	°F
ρ	1.2	kg/m ³	4.335e-5	lb/in ³
μ	1.814e-5	kg/s.m = Pa.s	2.631e-4	lbf.s/in ²
a	346.123	m/s	1.363e-4	in/s

E.2 Flat Plate Aerodynamics

The Theodorsen function is derived from the basic principles of potential flow theory, where the expressions of the aerodynamic lift and the moment forces are linear in the vertical and the torsional degrees-of-freedom and their first and second derivatives. The aerodynamic coefficients of this expression are defined in terms of two theoretical functions $F(k)$ and $G(k)$, where k is half of the reduced frequency, K , which equals to $B\omega/U$, where B is the width of the airfoil cord, ω is the frequency of the motion and U is the average laminar wind speed. The Theodorsen aerodynamic coefficient $C(k)$ is described as follows,

$$C(k) = F(k) + iG(k), \text{ where}$$

$$F(k) = \frac{J_1(J_1 + Y_0) + Y_1(Y_1 + J_0)}{(J_1 + Y_0)^2 + Y_1(Y_1 - J_0)^2}, \text{ and} \quad \text{E.6}$$

$$G(k) = \frac{J_1 J_0 + Y_0 Y_1}{(J_1 + Y_0)^2 + Y_1(Y_1 - J_0)^2}$$

J_0, J_1, Y_0 and Y_1 are the Bessel functions, which are canonical solutions $y(x)$ of Bessel's differential equation.

The theoretical expressions for sinusoidally oscillating lift and moment on a flat plate airfoil are, respectively:

$$L_h = -\rho b^2 \left(U\pi\dot{\alpha} + \pi\ddot{h} - \pi b a \ddot{\alpha} \right) - 2\pi\rho C(k) \left(U\alpha + \dot{h} + b\left(\frac{1}{2} - a\right)\dot{\alpha} \right) \quad \text{E.7}$$

$$M_\alpha = -\rho b^2 \left(\pi\left(\frac{1}{2} - a\right)U b \dot{\alpha} \right) + \pi b^2 \left(\frac{1}{8} + a^2 \right) \ddot{\alpha} - a\pi b \ddot{h} \\ + 2\rho U b^2 \pi \left(\frac{1}{2} + a \right) C(k) \left(U\alpha + \dot{h} + b\left(\frac{1}{2} - a\right)\dot{\alpha} \right) \quad \text{E.8}$$

where, k and U are as defined above, ρ is the wind density, b is half of the length of the airfoil cord (B), a is the distance from the mid-chord to the rotation point and h and α are vertical and angular displacement, respectively. The dot and the double dots, appear over α and h , are the first and second derivative with time, that is, velocity and acceleration, respectively.

For bluff bodies, and suspension bridge decks, a different expression is suggested. The expression is discussed in Chapter 6. In the expression of the aerodynamic forces of bluff bodies, displacement and velocity terms of each degree-of-freedom are correlated to separate aerodynamic coefficients. The above equations are equated to the aerodynamic forces of suspension bridges, and an equivalent expression to the flat plate aerodynamic forces, is obtained by evaluating the aerodynamic coefficients of the bluff body correspondingly. These coefficients are expressed in Chapter 5.

REFERENCES

ADINA-F Manual (2006), ADINA R&D, Inc., Boston, USA

AGA and OPAC – Geospectra (1994), *Tacoma Narrows Bridge Seismic Vulnerability Study*,

Ammann, O.H.; Karman, T. and Woodruff, G.B. (1941), *The failure of the Tacoma Narrows bridge*, Report to the Federal Works Agency.

Barar, P. S.; Raul, R. and Scanlan, R. H. (1996), *Numerical Calculation of Flutter Derivatives Via Indicial Functions*, Journal of Fluid and Structures, vol 10, pp. 337-351

Barriga-Rivera, Alfredo Nicolas (1973), *Aeroelastic Vibrations of Structural Shapes in Highly Turbulent Flows*, Master of Science thesis, Washington State University.

Bathe, K.J. and Zhang, H. (1999), *Finite element analysis of fluid flows fully coupled with structural interactions*, Computers & Structures, Vol. 72, Issues 1-3, Pages 1-16

Bertin J. (2002), *Aerodynamics for Engineering, Fourth Edition*, Prentice Hall, New Jersey,

Boussinesq, J. (1877), *Théorie de l'écoulement Tourbillant*, Mémoires Présentées par Divers Savants de l'Académie des Science, Institut de France, Vol. 23, pp. 46-50

Brancaleoni, F. and Diana, G. (1993), *The aerodynamic design of the Messina Straits*

Bridge, Journal of Wind Engineering and Industrial Aerodynamics, Vol. 48 (2-3), p.
p 329-342

Brar, P. S.; Raul, R. and Scanlan, R. H. (1996), *Numerical Calculation of Flutter Derivative Via Indicial Function*, Journal of Fluid and Structures, issue 10, p. 337 – 351

Cebeci, T. and Simth, A.M.O. (1974), *Analysis of Turbulent Boundary Layers*, Ser. in Appl. Math and Mech., Vol. XV, Academic Press, Orlando, Florida

Cebeci, T. and Simth, A.M.O. (1974), *Analysis of Turbulent Boundary Layers*, Ser. in Appl. Math and Mech., Vol. XV, Academic Press, Orlando, Florida

Chen W.F., Duan L. (1999), *Bridge Engineering Handbook*, CRC Press, Florida, USA

Chopra, Anil (2001), *Dynamics of Structures: Theory and Applications to Earthquake Engineering*, Third Edition, Pearson Education, Inc., New Jersey, USA.

Cigada, A.; Diana, G.; Falco, M.; Fossati, F. and Manenti, A. (1997), *Vortex shedding and wake-induced vibrations in single and bundle cables*, Journal of Wind Engineering and Industrial Aerodynamics, Vol. 72 , issue Nov.-Dec, Pages 253-263

Davenport, A. G. (1961), *The Response of Slender, Line-like Structures to a Gusty Wind*, Proceedings of the Institute of Civil Engineering, 19, pp. 449-472

Diana, G.; Bruni, S.; Cigada, A. and Collina (1993), A., *Turbulence Effect on Flutter Velocity in Long Span Suspended Bridges*, Journal of Wind Engineering and

Industrial Aerodynamics, Vol. 48 (2-3), p.p. 329-342

Dunn, L.G. (1941), *The failure of the Tacoma Narrows bridge. Report to the Federal Works Agency*, Appendix VIII, Volume 28, issue March.

Dyrbye, C. and Hansen, S. (1997), *Wind Loads on Structures*, John Wiley and Sons, England,

Farquharson, F. B. (1954), *Aerodynamic Stability of Suspension Bridges: with special reference to the Tacoma Narrows Bridge*, The Structural Research Laboratory – University of Washington, Seattle

Fiana, G.; Bruni, S.; Cigada, A. and Collina, A., *Turbulence Effect on Flutter Velocity in Long Span Suspended Bridges*, Journal of Wind Engineering and Industrial Aerodynamics, Vol. 48 (2-3) October 1993, p.p. 329-342

Frandsen J.B. (2004), *Numerical bridge deck studies using finite elements. Part1:1 flutter*, Journal of Fluid and Structures, 19, p. 171-191

Garrick, I.E. (1938), *On some reciprocal relations in the theory of nonstationary flows*, NACA Tech. Report 629, Nat. Advisory Committee for Aeronautics, Langley, VA.

Ge M.m Zhang R., Xiang H. (2000), *Identification of flutter derivatives of bridge decks*, Journal of Engineering and Industrial Aerodynamics, volume 84, pp. 151-162

Ge Y.J. and Tanaka H. (2000), *Aerodynamic flutter analysis of cable-supported bridge by multi-mode and full-mode approaches*, Journal of Wind Engineering and

Industrial Aerodynamics, vol. 86, p.: 123-153

Grant, I. and Barnes, F. H. (1981), *The vortex shedding and drag associated with structural elements*, Journal of Wind Engineering and Industrial Aerodynamics, Volume 8, Issues 1-2, Pages 115-122

Huston, D.; Bosch, H. and Scanlan, R. (1988), *The Effects of Fairings and of Turbulence on the Flutter Derivatives of a Notably Unstable Bridge Deck*, Journal of Wind Engineering and Industrial Aerodynamics, Vol. 29, p.p. 339-349.

Jones, N.P.; Scanlan, R.H.; Sarkar, P.P; Singh, L. (1995), *The effect of Section Model Details on Aeroelastic Parameters*, Journal of Engineering and Industrial Aerodynamics, Vol. 54/55, p.p. 45-53

Katsuchi H.; Jones N.P.; Scanlan R.H. (1998), *Akiyama H., Multi-mode flutter and buffeting analysis of the Akashi-Kaikyo bridge*, Journal of Wind and Engineering and Industrial Aerodynamics, vol. 77&78, p.: 431-441

Katsuchi, H.; Jones, N.P.; Scanlan, R.H.; Akiyama, H. (1998), *Multi-mode flutter and buffeting analysis of the Akashi-Kaikyo bridge*, Journal of Wind Engineering and Industrial Aerodynamics, Vol. 77&78, p.p. 431-441

Kussner, H.G. (1936), *Zusammenfassender Bericht u ber den instation a ren Auftrieb von Flugeln*, Luftfahrt-Forschhung , 13, :410 - 424

Liepmann, H. W. (1952), *On the Application of Statistical Concepts to the Buffeting Problem*, Journal of Aeronautical Science, 19, 12, pp. 793-822

- Matsumoto, M.; Nakajima, N.; Taniwaki, Y.; Shijo, R. (2001), *Grating effect on flutter instability*, Journal of Wind Engineering and Industrial Aerodynamics, Vol. 89, p.p. 1487-1497
- O'Connor C (1971)., *Design of Bridge Superstructures*, Wiley-Interscience, New York
- OPAC Consulting Engineers (1993), *Tacoma Narrows Bridge Seismic Vulnerability Study: Calculations*
- Peterson, S. (2002), *Experimental Response and Analysis of the Evergreen Point Floating Bridge*, A PhD dissertation, Washington State University
- Prandtl, L. (1925), *Über die ausgebildete Turbulenz*, ZAMM, Vol. 5, pp. 136-139
- Prandtl, L. (1925), *Über die ausgebildete Turbulenz*, ZAMM, Vol. 5, pp. 136-139
- Prandtl, L. (1945), *Über ein neues Formelsystem für die ausgebildete Turbulenz*, Nacr. Akad. Wiss. Gottingen, Math-Phys. Kl., pp. 6-19
- Prandtl, L. (1945), *Über ein neues Formelsystem für die ausgebildete Turbulenz*, Nacr. Akad. Wiss. Gottingen, Math-Phys. Kl. 1945, pp. 6-19
- Pugsley, A., (1949), Some experimental work on model suspension bridges, structural engineering, Volume 8, issue 27
- Pugsley, Sr. Alfred (1968), *The Theory of Suspension Bridges*, Second Edition, Edward Arnold Publishers LTD, London, UK

Rotta, J. C. (1951), *Statistische Theorie nichthomogener Turbulenz*, Zeitschrift für Physik, Vol. 129, pp. 547-572

Rotta, J. C. (1951), *Statistische Theorie nichthomogener Turbulenz*, Zeitschrift für Physik, Vol. 129, pp. 547-572

Rowan Williams Davies & Irwin Inc (2003), *Final Report – Volume 1 of 2, Wind Engineering Studies: Tacoma Narrows Bridge*, Ontario, Canada

Sarkar, P. (1992), *New-identification methods applied to the response of flexible bridges to wind*, PhD thesis, The John Hopkins University, Baltimore, Md.

Sarkar, P.P.; Jones, N.P. and Scanlan, R.H. (1994), *Identification of aeroelastic parameters of flexible bridges*, Journal of Engineering mechanics. ASCE 120, p.p.1718-1742

Sarkar, Partha (1986), *Effect of Wind Turbulence on The Stability of Long Span Bridges*, Master of Science Thesis, Washington State University, USA

Scanlan, R. (1988), *On Flutter and Buffeting Mechanisms in Long-Span Bridges*, Journal of Probabilistic Engineering Mechanics, Vol. 3, No. 1, p.p. 22-27

Scanlan, R. H. (1983), *On Linearized airfoil and bluff-body stability theory and the Scruton number*, Journal of wind engineering and industrial aerodynamics, vol. 12, pp. 373-378

Scanlan, R. H. and Tomko, J. J. (1971), *Airfoil and bridge deck flutter derivatives*, Journal of the Engineering Mechanics Division, Proceedings of the ASCE, Vol. 97,

No. EM 6, p.p. 1717-1737

Scanlan, R.H. and Budlong, K.S. (1972), *Flutter and aerodynamic response considerations for bluff objects in a smooth flow, Flow-induced structural vibrations*, Proc. Symp. IVTAM-IAHR, Karlsruhe, Springer, Berlin, Germany p.p.339—354

Scanlan, R.H., and Sabzevari, A. (1967), *Suspension bridge flutter revisited*, Proceedings of Structural Conference, ASCE, Paper No.468, New York

Scanlan, R.H.; and Rosenbaum, R. (1951), *Aircraft Vibration and Flutter*, Macmillan, New York

Scanlan, R.H.; Jones, N.P.; Singh, L. (1997), *Inter-relations among flutter derivatives*, Journal of Wind Engineering and Industrial Aerodynamics, Vol 69 – 71, p.p. 829 – 837

Scanlan, R. and Lin, WH (1978), *Effects of Turbulence on Bridge Flutter Derivatives*, Journal of the Engineering Mechanics Division, Proceedings of the American Society of Civil Engineers, Vol. 104. No. 4

Sears, W.R. (1941), *Some aspects of non-stationary airfoil theory and its practical application*, Journal of Aeronautical Science, Vol. 8, issue 3, p.p.104—108

Singh, L.; Jones, N.P.; Scanlan, R.H. and Lorendeaux, O. (1996), *Identification of lateral flutter derivatives of bridge decks*, Journal of wind Engineering and Industrial Aerodynamics, Vol. 60, p.p. 81-89

Svehla, R. A. (1962), *Estimated Viscosities and Thermal conductivities of Gases at*

High Temperatures, Technical Repot R-132 NASA

Svehla, R. A. (1962), *Estimated Viscosities and Thermal conductivities of Gases at High Temperatures*, Technical Repot R-132 NASA

The ASCE 7-02 Committee (2003), *Minimum Design Loads for Buildings and other Structures: Revision of ASCE 7-98*, ASCE Publication, Virginia, USA

Theodorsen T. (1935), *General theory of aerodynamic instability and mechanism of flutter*, NACA Report 496, U.S. Nat. Advisory Committee for Aeronautics, Langley, VA

Theodorsen, T. (1934), *General theory of aerodynamic instability and the mechanism of flutter*, NACA a 496, National Aeronautics and space Administration

Ukeguchi, M.; Sakata, H. and Nishitani, H. (1966), *An investigation of aeroelastic instability of suspension bridges*, Proceedings Symposium on Suspension Bridges, Lisbon, Portugal

Wagner, H. (1925), *U ber die Entstehung des dynamischen Auftriebs von Tragflugein*, Zeit. Angew. Math. U. Mech. 5(1) p.p.17—35

Wanderley, J.B. and Levi, C.A. (2002), *Validation of a finite difference method for the simulation of vortex-induced vibrations on a circular cylinder*, Ocean Engineering, 29, p.p. 445-460

Wanderley, J.B. and Levi, C.A. (2002), *Validation of a finite difference method for the simulation of vortex-induced vibrations on a circular cylinder*, Ocean

Engineering, 29, p.p. 445-460

Wilcox D.C. (1993), *Turbulence Modeling for CFD*, DCW Industries, Inc., California

Wilcox, D.C. (1993), *Turbulence Modeling for CFD*, DCW Industries, Inc., California

Wilson E. (2002), *Three Dimensional Static and Dynamic Analysis of Structures*, Computers and Structures Inc., Third Edition, Berkeley, CA, USA

Zhang H.; Zhang, Xiaoli; Ji, Shanhong; Guo, Yanhu; Ledezma, Gustavo; Elabbasi, Nagi and deCougny, Hugues (2003), *Recent development of fluid–structure interaction capabilities in the ADINA system*, Journal of Computers & Structures, Volume 81, Issues 8-11, p.p. 1071-1085

Zhang, H. and Bathe, K.J. (2001), *Direct and Iterative Computing of Fluid Flows fully Coupled with Structures*, Proceedings of the First MIT Conference on Computational Fluid and Solid Mechanics, Boston, USA